Université de Neuchâtel
Institut de microtechnique

Microoptical Systems for Fluorescence Detection in Chemical Microsystems

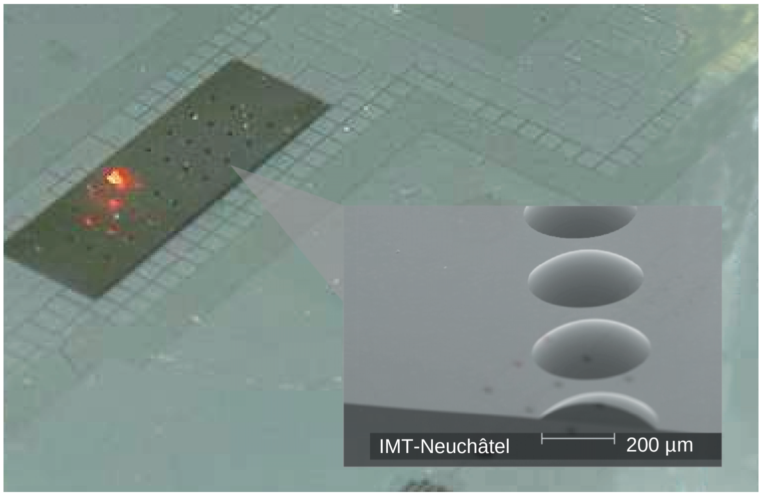

Thèse

Présentée à la Faculté des sciences
pour obtenir le grade de docteur ès sciences
par

Jean-Christophe Roulet

Neuchâtel, mars 2001

IMPRIMATUR POUR LA THESE

Micro-optical Systems for Fluorescence Detection in Chemical Microsystems

de M. Jean-Christophe Roulet

UNIVERSITE DE NEUCHATEL

FACULTE DES SCIENCES

La Faculté des sciences de l'Université de Neuchâtel sur le rapport des membres du jury,

MM. R. Dändliker (directeur de thèse),
H.P. Herzig, S. Verpoorte et
R.E. Kunz, CSEM Zürich

autorise l'impression de la présente thèse.

Neuchâtel, le 13 juin 2001

Le doyen:

J.-P. Derendinger

An experiment is a question which we ask of Nature, who is always ready to give a correct answer, provided we ask properly, that is, provided we arrange a proper experiment.

– CHARLES VERNON BOYS, 1896

Summary

Since the beginning of microelectronic industry and microfabrication technology in the 1960s, various types of integrated chemical sensors have been developed. Unfortunately, most of these sensors lack in sensitivity, reproducibility and/or longevity. At the beginning of the 1980s a way to circumvent these limitations was proposed with the ”total analysis system” concept (TAS). In 1990 a miniaturized form of TAS (μ-TAS or μTAS) began to be investigated. A μTAS incorporates on the same chip the functions of sampling, sample transport, separation (or any necessary chemical reaction) and detection.

The present work gives an overview of the author's contributions to the development of integrated microoptical systems for μTAS applications. Unlike other similar microchemical systems, using standard and hence bulky optical systems (such as a confocal microscope), the optical elements (refractive microlens and chromium/aluminium aperture arrays) composing the detection system are directly, and precisely, structured onto the microchemical chip. **Chapter 1** presents an introduction to fluorochromes and laser induced fluorescence detection (LIF) and detection system integration issues. **Chapter 2** presents detection system geometries and their comparison with the help of raytracing simulations. **Chapter 3** deals with the microchemical chip and microoptical elements fabrication. **Chapter 4** presents experimental results and the comparison of the integrated detection system with a confocal, epiluminescent detection system. The summary and conclusions of the thesis are presented in **Chapter 5**. The publication list related to this work is presented in the annex.

Contents

Chapter 1

Introduction

1.1 Total and miniaturized total analysis systems

Nowadays, the need for fast automated chemical systems instruments keeps on growing. Potential applications of such systems in chemical or biotechnological industry, nutritional and environmental control, medical and life sciences are manifold. As examples one can cite real-time monitoring of specific or critical substances during chemical and biochemical processes (improvement of manufacturing processes and industrial safety), continuous control of industrial waste effluents and toxic species in air (i.e. pollution control) and fast, inexpensive clinical tests at point-to-care. Analytical chemistry offers a great number of methods for the analysis of almost every compound in any environment. Yet, most of these methods are time consuming (i.e. not suitable for real-time monitoring) and require expensive fully-equipped laboratories and qualified technicians. This is why the realization of integrated sensors enabling the transformation of chemical information into electronic information is of great interest.

In 1983, H. Michael Widmer introduced the concept of the total analysis system (TAS) [1, 2]. A TAS incorporates elements for sampling, sample transport, sample pretreatment, separation or chemical reaction, detection, and data treatment into a single flow system. Furthermore, the elements necessary for calibration and cleaning can also be implemented. Thus, a TAS is able to work autonomously and automatically.

In principle, stand-alone chemical sensors are an ideal approach for continuous monitoring applications, since they need only to be immersed in the sample to obtain the desired information. Unfortunately, the chemically sensitive interfaces of these sensors often lack sensitivity and tend to suffer from interferences due to other species present in the sample. Hence, few chemical sensors achieve a good sensitivity independent of sample composition. Moreover, the chemically sensitive interfaces also lack in longevity and stability over time. In TAS, as shown in Fig. 1.1, these problems are avoided by the fact that samples are taken from the solution to be analyzed (the TAS is thus not in continuous direct contact with the solution). Sample pretreatment stages can also be used to eliminate interfering or aggressive species which would otherwise attack or cause to deteriorate subsequent TAS components, such as the detector for example.

Many well-known and powerful techniques of analytical chemistry and detection methods can be implemented in TAS. In the early 1990s, Andreas Manz showed that miniaturizing total analysis systems (then called μ-TAS or μTAS) not only enables a size reduction of the analytical system (thus allowing portable systems) and/or a significant reduction of reagent and sample consumption, but also improves TAS performance [3]. The reduction of microfluidic channel diameters increases the efficiency of sample pretreatment techniques (such as chromatographic and electrophoretic separation) and enables the use of electroosmotic pumping to handle and transport liquid phase samples through a μTAS [4, 5, 6]. Furthermore, a reduction of the distance over which a sample has to travel between μTAS elements results in a reduced transport time, which in turn contributes to decreased times of analysis, a crucial point for real-time monitoring. Thus, a μTAS resembles a standard chemical sensor in many regards, yet with improved sensitivity and durability, and benefits from the fact that each analysis step can be optimized and kept under the control of the user [7].

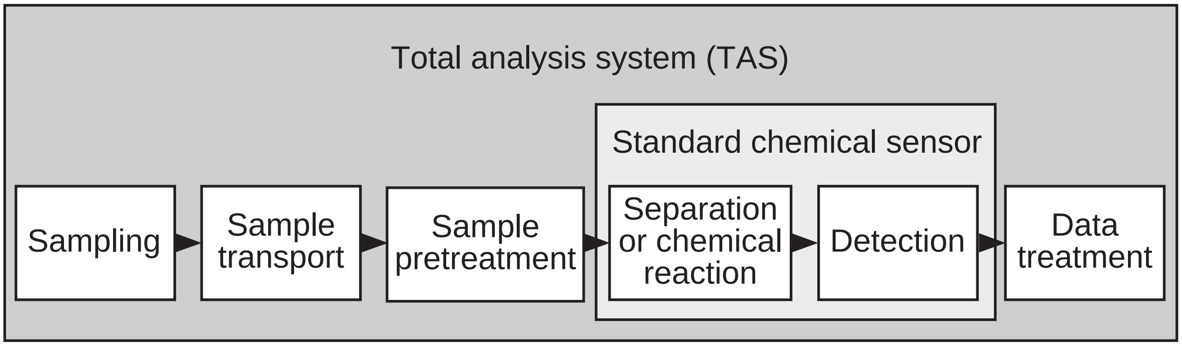

Figure 1.1: Total analysis system block-diagram.

The technology necessary to realize structures with μm feature size, and hence μTAS has been developed since the 1960s by the semiconductor industry [8, 9]. Beside the integration of electronic components (transistor, resistance, etc.), this IC fabrication techniques (or microfabrication) can be used to realize not only micromechanical devices (micropumps, microvalves, etc.) and microfluidic networks [10, 11], but also, microoptical elements such as refractive and diffractive lenses [12, 13, 14].

The present work gives an overview of the author's contributions to the development of integrated microoptical systems for μTAS applications. Unlike other similar microchemical systems, using standard and hence bulky optical systems (such as a confocal microscope), the optical elements (refractive microlens and chromium/aluminium aperture arrays) composing the detection system are directly, and precisely, structured onto the microchemical chip. This chapter presents an introduction to fluorochromes and laser induced fluorescence detection (LIF) and detection system integration issues. Chapter 2 presents detection system geometries and their comparison with the help of raytracing simulations. Chapter 3 deals with the microchemical chip and microoptical elements fabrication. Chapter 4 presents experimental results and the conclusions concerning the detection performance of the system. A summary of the thesis and the final conclusions are presented in Chapter 5. Part of this work is reported in the following publications:

I. J.-C. Roulet, E. Verpoorte, R. Völkel, H. P. Herzig, N. F. de Rooij, and R. Dändliker, Fabrication of Multilayer Systems Combining Microfluidic and Micro-Optical Elements for Fluorescence Detection, *IEEE Journal of Microelectromechanical Systems*, accepted for publication, March 2001 (will appear in Vol. 10 either September or December 2001).

II. J.-C. Roulet, E. Verpoorte, R. Völkel, H. P. Herzig, N. F. de Rooij, and R. Dändliker, Microlens Systems for Fluorescence Detection in Chemical Microsystems, *Optical Engineering*, **40**(5), pp. 814–821, (May 2001).

III. J.-C. Roulet, E. Verpoorte, R. Völkel, H. P. Herzig, N. F. de Rooij, and R. Dändliker, Integration of micro-optical systems for fluorescence detection in μTAS applications, *Proc. of the μTAS'2000 Symposium*, 14-18 May, Enschede, The Netherlands, pp. 163–166, (2000).

IV. J.-C. Roulet, K. Fluri, E. Verpoorte, R. Völkel, H. P. Herzig, N. F. de Rooij, and R. Dändliker, Micro-optic integration for fluorescence detection in μTAS systems, *Proc. Transducers'99*, 7-10 June, Sendai, Japan, pp. 120–123, (1999).

V. J.-C. Roulet, K. Fluri, E. Verpoorte, R. Völkel, H. P. Herzig, N. F. de Rooij, and R. Dändliker, Micro-optical systems for fluorescence detection in μTAS applications, *Proc. of the μTAS'98 workshop*, 13–16 October, Banff, Canada, pp. 287–290, (1998).

An exhaustive list of papers and conference/workshop papers related to this work are presented in appendix B.

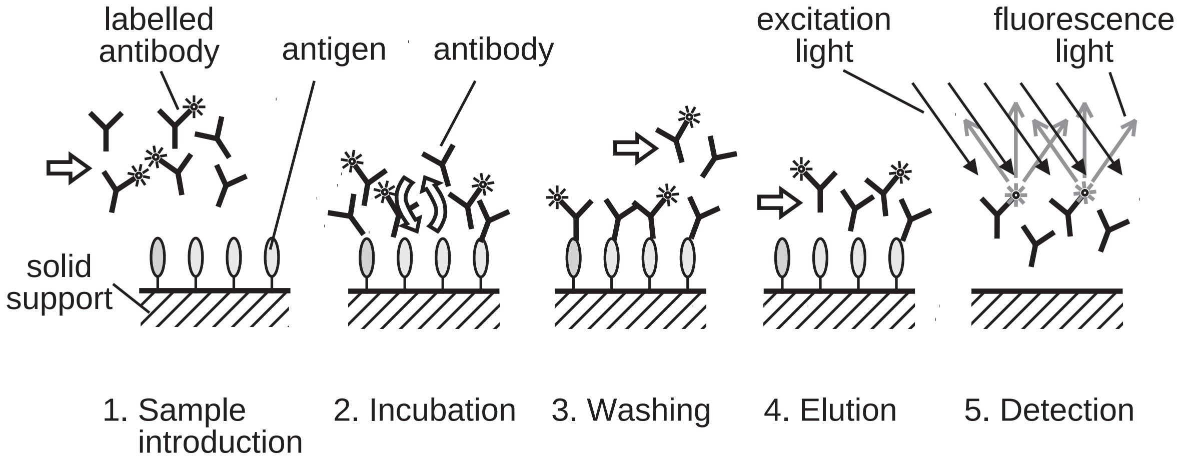

Figure 1.2: Schematic diagram of the principle of a competitive heterogeneous immunoassay with fluorescence detection.

1.2 Laser induced fluorescence detection

To date, many different detection methods, ranging from electrochemical to optical have been integrated onto microchemical chips. These methods can be either direct (analyte detected directly) or indirect (detection of a reagent which interacts somehow with the analyte). For example, one can cite UV-absorbance [15, 16, 17], refractive index measurement [18, 19, 20, 21, 22], electrochemical detection [23, 24, 25] or laser induced fluorescence measurements (LIF) [26, 27, 28]. Due to its selectivity and high sensitivity [3, 29, 30], LIF is one of the preferred detection techniques on microchemical chips and the detection technique chosen here to be implemented onto a microchemical chip.

1.3 Heterogeneous immunoassay techniques

The analytical application for which microchemical chips were designed in this project was basic biochemical analysis using heterogeneous immunoassay techniques. This work was done by K. Fluri and A. Dodge in our partner group, SAMLAB [31]. These techniques exploit the highly specific antigen/antibody interaction. Figure 1.2 shows the Protein A-rIgG model studied and Fig. 1.3 shows how this model was implemented onto a microchemical chip. Generally, antibodies are immobilized in these types of assays. In this case however, Protein A (antigen) are immobilized on the surface of a microchannel section (called the reaction chamber) and the antibody/immunoglobulin G (IgG) is being analyzed. In the competitive assay format, the sample previously mixed with a known amount of labeled analyte (antibody) is transported to the reaction chamber (sample introduction) where the labeled and unlabeled analytes compete for a limited number of

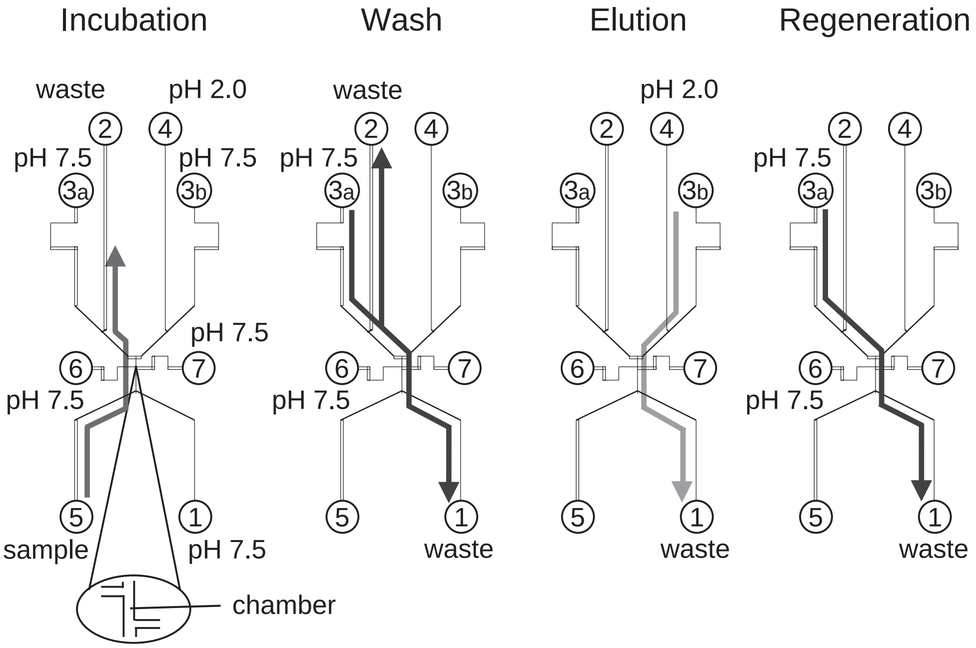

Figure 1.3: Operated electrokinetically microfluidic chip for heterogeneous bioassays using a locally immobilized biospecific layer. The reaction chamber has picoliter dimensions and is integrated into a network of microchannels etched in glass (picture courtesy of A. Dodge).

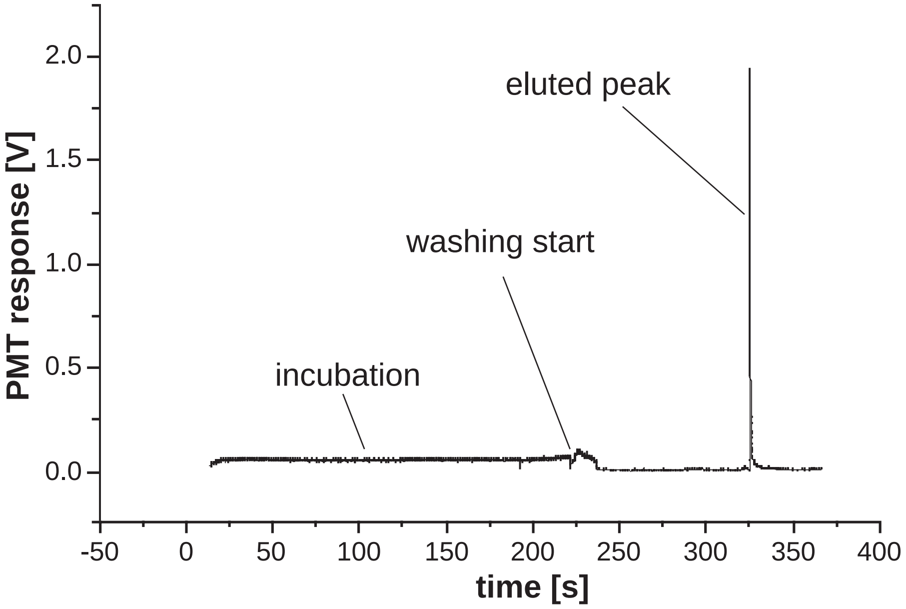

Figure 1.4: Photomultiplier (PMT) response for a full analysis cycle (picture courtesy of A. Dodge).

antigen binding sites. After a certain amount of time (incubation), excess sample (and hence the unbound antibodies) is washed away (washing). Finally, with the help of a chaotropic reagent, the bound analytes are released and transported to an in-channel detection volume (elution). The system can then be rinsed and prepared for the next measurement (regeneration). The resulting signal intensity is proportional to the labeled analyte concentration and hence inversely proportional to the analyte concentration [32]. Figure 1.4 shows a trace of the fluorescence emitted from the detection volume of the microchemical chip for the analysis sequence described in Fig. 1.3. The signal is recorded by means of a standard detection system (photomultiplier mounted on a microscope system). The concentration of the Cy5-rIgG solution is 1.5 μM and the incubation time is 200 s. The full cycle takes 350 s. Note that the intensity of the eluted peak is many times that of the fluorescence of the original sample. This is because Cy5-rIgG was concentrated on the surface of the reaction chamber during incubation, to the point that the eluted concentration was much greater than the original 1.5 μM sample. The ability to concentrate samples on a specially prepared surface is one of the main advantages of heterogeneous immunoassay.

The channels used in these chips were etched isotropically in glass wafers and have a more or less semi-circular profile (Chap. 3).

1.4 Fluorochromes

Although some molecules are naturally fluorescent (e.g. riboflavin, vitamin B2), the fluorescence emission is often weak. Most molecules do not fluoresce at all. This is why fluorescent labels (or fluorochromes) are often chemically attached to the substance to be detected. Fluorochromes absorb photons at specific wavelengths and after a short delay re-emit photons at a slightly longer wavelength (Sec. 1.4.1). This wavelength shift (termed Stokes' shift) enables a spectral differentiation between the light used for exciting the fluorochromes and the light emitted by the fluorochromes. The utilization of fluorescent labels is a well known technique, and a wide choice of these molecules, covering a large spectra of chemical, biochemical and clinical applications, is available. The analyte can be selectively excited, and this in a complex mixture of molecular species. Moreover, this technique can be used to detect different species (with different fluorochromes) at the same time. From the optical detection point of view, fluorochrome molecules are mainly characterized by the absorption and emission spectra, the emission intensity, the absorption time and the fluorescence life time [33, 34].

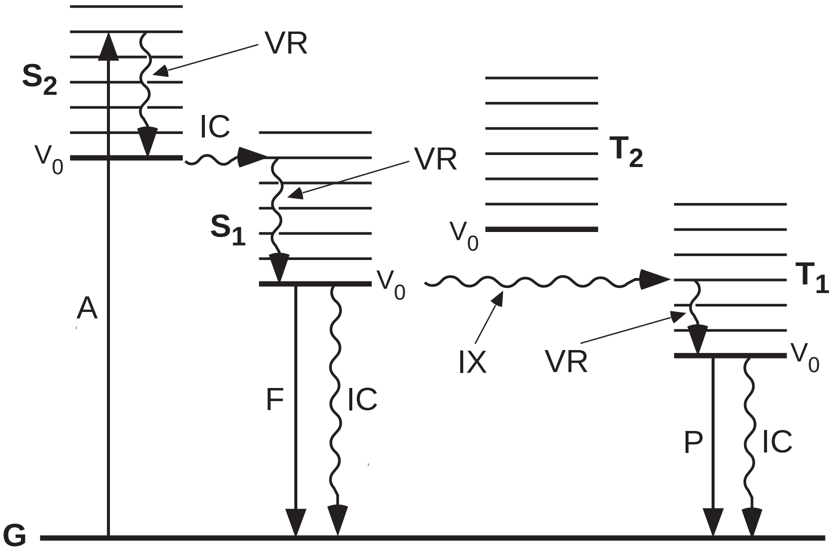

Figure 1.5: Electronic energy-level diagram for a molecule with ground state (**G**) and excited singlet (**S**) and triplet (**T**) states. Radiationless transitions between states are represented by wavy arrows; A is absorption, F is fluorescence, P is phosphorescence, VR is vibrational relaxation, IX is intersystem crossing, and IC is internal conversion (diagram taken from *Chemical Separations and Measurements* [35]).

1.4.1 Absorption and emission spectra

As shown in Fig. 1.5, when fluorochrome molecules are excited with photons of sufficiently high energy (i.e. sufficiently short wavelength, Eq. (1.1)), the probability exists that a valence electron of the molecule situated at the ground level (G) absorbs a photon and is boosted up to a higher and less stable energy level (S_1, S_2). After a short period of time, depending of the fluorochrome type (Sec. 1.4.3), the excited electron returns to the ground level via either a radiative or a non radiative transition (i.e. with or without the emission of a photon, as discussed in Sec. 1.4.2). Most of the time, before the relaxation from the lowest singlet excited state, the excited electron lost part of its energy via non radiative transitions [35]. Thus, photons emitted during relaxation have on average a lower energy (hence a longer wavelength) than the excitation photons. The emission spectrum is thus shifted towards longer wavelengths. The relation between the wavelength and the energy of a photon is given by

$$\lambda = \frac{h\,c}{E}, \tag{1.1}$$

where λ is the wavelength of light, h is the Planck's constant ($6.6262 \cdot 10^{-11}\ J\,s$), c the velocity of light in vacuum ($2.997924 \cdot 10^{8}\ m\,s^{-1}$) and E is the energy of the photon.

Absorption and emission spectra are specific to each fluorescent molecule. The difference between the excitation and the fluorescence peak ranges from 7 nm to 238 nm [34]. The absorption and emission spectra of molecules broaden as the number of energy levels

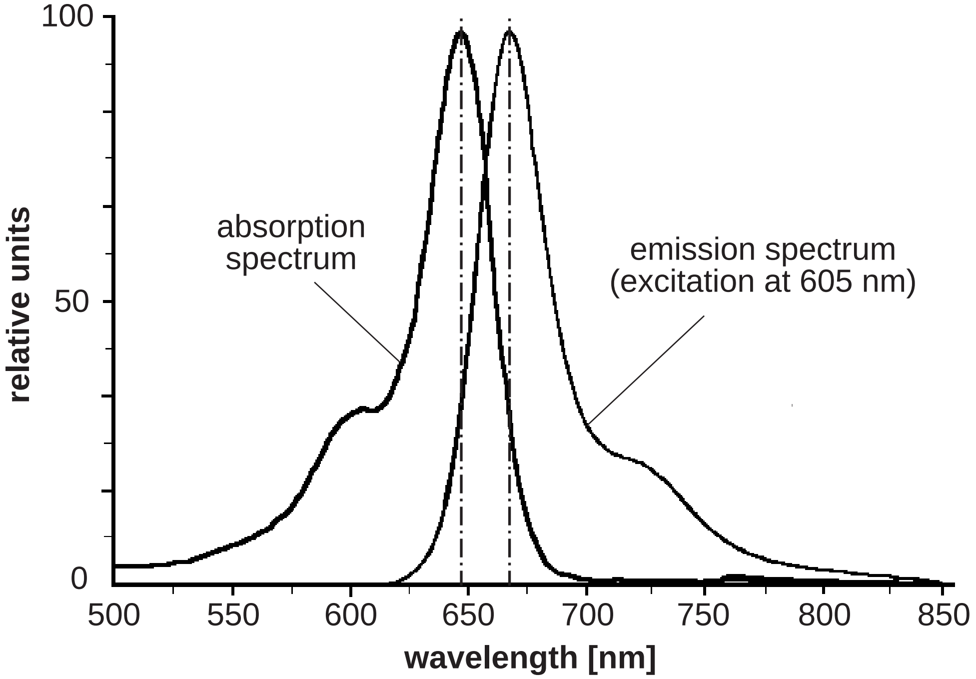

Figure 1.6: Absorption and emission spectra for Cy5^{TM} fluorochrome in water. The absorption peak is at 649 nm and the emission peak at 670 nm (spectra courtesy of Dr. A. Paulus). The extinction coefficient ε is $250'000\,M^{-1}\,cm^{-1}$ and the quantum efficiency ϕ is > 0.28.

(hence the number of transition pathways) increases.

Figure 1.6 shows the absorption and excitation spectrum of Cy5^{TM} cyanine fluorochrome (Amersham Life Science Ltd., Bucks, England). In this case, the Stokes shift is about 21 nm. This fluorescent marker was chosen for its brightness (see next section), ease of attachment to proteins, and longer excitation wavelength, which allowed a less costly and smaller red laser diode or $HeNe$ laser to be used.

1.4.2 Fluorochrome brightness

The brightness of a fluorochrome represents the capacity of the molecule to absorb excitation photons and to re-emit fluorescence photons. The brightness is proportional to the product of the extinction coefficient ε and the quantum efficiency ϕ:

$$Brightness \propto \varepsilon\,\phi \tag{1.2}$$

The extinction coefficient represents the probability of absorption of excitation photons by the fluorescent molecules. Useful fluorochromes have an extinction coefficient ranging from 40 000 to 250 000 $M^{-1}\,cm^{-1}$. The quantum yield is defined as the ratio of the quanta emitted divided by the number of quanta absorbed. For practical purposes, the quantum yields should be greater than 0.1. The brightness of a fluorochrome is linearly proportional to its concentration, and this over a wide range (e.g. from 10^{-9} M to 10^{-3} M for fluoresceins and at least from 10^{-9} M to $10 \cdot 10^{-6}$ M for Cy5). The signal becomes nonlinear at higher concentrations.

1.4.3 Absorption time and fluorescence life time

The time required for a photon to be absorbed by a fluorochrome is extremely small ($\sim 10^{-15}$ s) compared to the average time that a molecule remains in the excited state. When photons are emitted by the molecule within a time delay of $\sim 10^{-8}$ s or less, the emitted light is termed fluorescence. Typical time delays for fluorescence (or fluorescence lifetime) range from 100 ns down to 1 ns [33]. For a time delay of $\sim 10^{-6}$ s or less, one speaks of delayed fluorescence, and for a time delay greater than $\sim 10^{-6}$ s, of phosphorescence.

1.5 Excitation and fluorescence light intensity

1.5.1 Absorption of the excitation beam

Absorbance of a solution containing fluorescent molecules is defined by the Lambert-Beer law [36, 37],

$$A = \log \frac{I_0}{I_T} = \varepsilon \, l \, c, \tag{1.3}$$

where I_0 is the incident excitation intensity, I_T the transmitted excitation intensity, c the concentration of the fluorescent molecules per unit volume (usually given in moles per liter) and l the path length of the excitation light through the sample. The Lambert-Beer law correctly describes the absorbance for fluorochrome concentrations of 0.01 M or lower. Above this concentration, interaction between absorbing molecules reduces the absorbance [37].

1.5.2 Fluorescence light intensity

The amount of excitation light absorbed by fluorescent molecules can be calculated with Eq. (1.3). Since the fluorescence light intensity I_F is proportional to the amount of absorbed excitation light ($I_0 - I_T$) and to the quantum yield (Sec. 1.4.2) [26], it can be expressed by

$$I_F = \phi \, I_0 \left(1 - 10^{-A}\right). \tag{1.4}$$

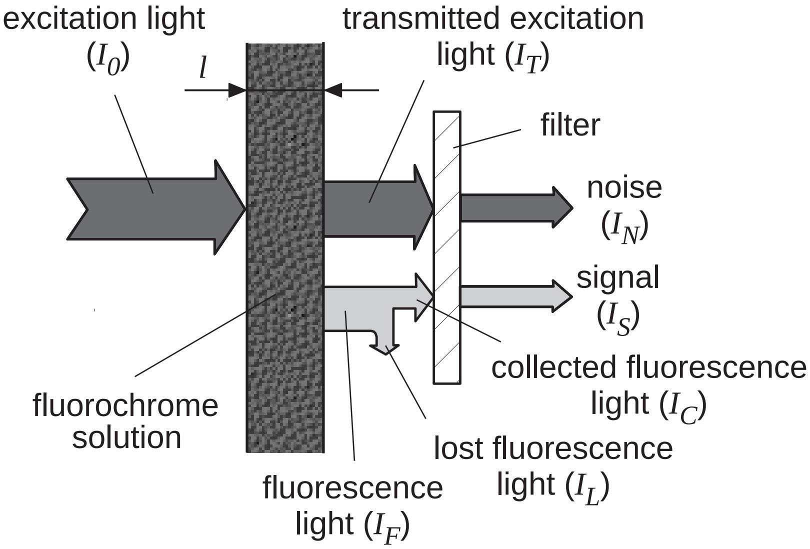

Figure 1.7: Schematic of light propagation for fluorescence measurements. Part of the excitation light I_0 is absorbed by the fluorochrome in solution and used to generate fluorescence light I_F. I_C represents the part of the fluorescence light which is collected and I_L the part which is lost. After the interference filter, the fluorescence light intensity I_S must be greater than the remaining excitation light I_N.

1.5.3 Fluorescence light intensity vs. background intensity

By combining Eqs. (1.3) and (1.4), the ratio of the fluorescence to the transmitted light intensity becomes

$$\frac{I_F}{I_T} = \phi \left(10^A - 1\right). \tag{1.5}$$

In the case of a 10 nM solution of Cy5™ ($\phi > 0.28$, $\varepsilon = 250\ 000\ M^{-1}cm^{-1}$) in a detection cell which is 25 μm deep, the ratio I_F/I_T is about $4 \cdot 10^{-6}$. The fluorescence intensity is thus about 250 000 times weaker than the excitation intensity.

This is why fluorescence detection cannot be performed without separating the fluorescence light from the transmitted excitation light. Interference filters are commonly used for this purpose (see Fig. 1.7). In the ideal case where all the fluorescence light would be collected (a situation which is hardly conceivable because of the uniform angular emission of the fluorescence light), the lost fluorescence light $I_L = 0$. Thus, the ratio between the fluorescence light I_S and the transmitted excitation light I_N remaining after the interference filter is given by

$$\frac{I_S}{I_N} = \phi \left(10^A - 1\right) 10^{OD(e)-OD(f)}, \tag{1.6}$$

where $OD(f)$ is the optical density of the filters at the fluorescence wavelength (mean value) and $OD(e)$ the optical density at the excitation wavelength. For a commercial filter specifically designed for Cy5™ detection one has $OD(f) = 27 \cdot 10^{-3}$ (maximal transmission of 94 %) and $OD(e) \simeq 5$ (transmission less than 10^{-3} %). Although this is an ideal case, the fluorescence light intensity is still about 2.6 times weaker than the transmitted excitation intensity. In most cases, the fluorescence light is collected by means of an objective with a limited numerical aperture ($I_L \neq 0$). The ratio between the total amount of fluorescence light emitted from the detection volume I_F and the collected fluorescence light I_C is then given by

$$\frac{I_C}{I_F} = \frac{1-\cos\theta}{2}, \tag{1.7}$$

where θ is the acceptance angle of the detection system. The numerical aperture NA is defined by

$$NA = n\,\sin\theta, \tag{1.8}$$

where n is the refractive index of the medium before the collection lens or objective. The acceptance angle is related to the focal length f_L and the entrance pupil diameter Ø_P of the collection objective. Eq. (1.8) becomes then

$$NA = n\,\sin\left[\arctan\left(\frac{\text{Ø}_P}{2\,f_L}\right)\right]. \tag{1.9}$$

By replacing θ with the numerical aperture NA defined in Eq. (1.8), Eq. (1.7) becomes

$$\frac{I_C}{I_F} = \frac{1-\sqrt{1-\frac{NA^2}{n^2}}}{2}, \tag{1.10}$$

and the ratio between I_C and I_0 as a function of NA gets

$$\frac{I_C}{I_0} = \phi\left(1-10^{-A}\right)\frac{1-\sqrt{1-\frac{NA^2}{n^2}}}{2}. \tag{1.11}$$

By inserting Eq. (1.10) into Eq. (1.6), the ratio between I_S and I_N now becomes

$$\frac{I_S}{I_N} = \phi\left(10^{A}-1\right)10^{OD(e)-OD(f)}\,\frac{1-\sqrt{1-\frac{NA^2}{n^2}}}{2}. \tag{1.12}$$

Even for an objective with an unusually high numerical aperture of 0.9 (typical NA for confocal systems are 0.3 to 0.8), the ratio of I_S to I_N is reduced to about 0.1. This means that the fluorescence intensity collected with the objective is about 10 times smaller than the transmitted excitation intensity. This is reduced even further to a value of $4 \cdot 10^{-3}$ for a NA of 0.3, which is a typical value for a refractive microlens (lenses with diameter under $\sim 1\ mm$ are called microlenses). Of course, part of the transmitted excitation which is scattered at system interfaces (e.g. at the microchannel walls) is not collected by the objective either. This will slightly increase the ratio between I_S and I_N.

However, spectral separation alone remains insufficient, so that the separation between the fluorescence and the non-absorbed excitation light must be improved. Angular separation or fluorochrome emission lifetime may be exploited for this purpose. It is precisely for this reason that conventional spectrometers collect fluorescence light at 90° (or another large angle) to the incident excitation beam. On the same way, epifluorescence detection (which can be combined with a confocal detection systems) use the same objective to focus the excitation light onto the sample and to collect the fluorescence light. Hence, the fluorescence is collected with an angle of 180° which enables a better detection sensitivity. In the confocal microscope, the collected light is focused onto a pinhole in front of the detector to increase the detection sensitivity by subtracting light which is not issued from the focal plan (false light).

The short fluorescence lifetime of most fluorochromes makes it difficult to apply time resolved detection, and would require sophisticated acquisition systems with very fast photodetectors [38, 39]. This is why we chose the combination of spectral and angular separation as detection strategy.

1.6 Detection system integration

1.6.1 Detection system for parallel microchannels

Today, the most common strategy to use LIF with multichannel chips is to scan the microchemical chip with respect to a stationary detection system (such as a confocal microscope), or to sweep the channels with a light beam [40]. These solutions require precise, and thus often expensive, bulky mechanical and optical systems, such as translation stages, movable mirrors or confocal microscopes [41]. Though microfabricated forms of some of these elements, such as scanning micromirrors, exist [42, 43, 44, 45], they must be realized on a separate silicon wafer. Since silicon is not transparent at most fluorochrome excitation wavelengths, the microchemical chip (or part of it) must be realized in glass or fused silica. Such a system, combining glass and silicon structures, a light source, a detection system and possibly optical elements to focus the scanning beam and to collect the fluorescence light, is expensive and complex to assemble.

Another possibility is to use an optical fiber to bring the excitation light to the detection cell. The fluorescent light can also be collected by means of a second optical fiber [46, 16, 47]. The fibers are generally fixed in grooves etched in the microfluidic chip. Detection is carried out either perpendicular to the flow in the microchannel or in the direction of flow, in a U-shaped flow cell with light directed through the bottom of the U.

In the former case [47], the groove can be directly connected to the microchannel (i.e. the optical fiber tip is in direct contact with the sample) or set back a bit from the microchannel and separated by a wall. In the first case, the watertightness of the microchannel or the direct contact between the optical fiber and/or the substance used to seal the groove and the sample is an issue. In the second case, the profile and/or the surface roughness of the wall causes scattering and excitation beam focusing problems [16]. For measurements in U cells, light has either been directed through a thin wall into the channel, or reflected into the detection volume using a mirror formed in silicon [46]. To avoid significant internal losses, the bending radius of the optical fibers must not be smaller than 10-20 mm. The use of fibers will also dictate a minimum spacing between adjacent microchannels, and hence limit the total number of channels possible on a chip. For parallel microfluidic systems, the alignment and fixing of optical fiber arrays would be difficult. Moreover, the packaging of several tens of optical fibers as well as their connection to a light source or to a detector becomes a delicate operation.

An integrated wave guide can also be used to bring the excitation light to the detection cell in two ways. In the first case, the reaction chamber (or the detection cell) must be placed directly in contact with the waveguide to enable the excitation of the fluorochromes with the evanescent part of the excitation wave [21, 48, 49]. This favorable placement allows for the fluorescence light to be detected perpendicularly to the excitation, and a good geometrical separation is achieved. The issue is here to get a good coupling efficiency of the excitation beam into the waveguide. Moreover, only one side of the evanescent wave can be used for excitation, and the depth of penetration of the evanescent wave is limited to a few wavelengths, which limits the detection volume and hence the fluorescence light intensity. In the second case, the detection configuration is much like that described in [47], with the integrated waveguide fulfilling the role of the optical fiber and transporting light to and from the detection volume [50].

Figure 1.8 shows a conceptual diagram of the approach chosen in this thesis. We take advantage of microfabrication technology to directly implement microoptical elements comprising part of the detection system onto a glass microchemical chip. Glass was chosen for its transparency (at excitation of most common fluorescent dyes) and because it is an electrical insulator. Therefore, electroosmotic flow can be used to pump chemical solutions. This solution enables the fabrication of small closely spaced optical elements, limited only by the microoptical element diameters, and their precise alignment with respect to the microfluidic channels, which is relatively easy due the fabrication method. As presented in Chap. 3, the microfluidics are chemically etched into one of the two wafers forming the microchemical chip (the second one is used to seal the chip) which

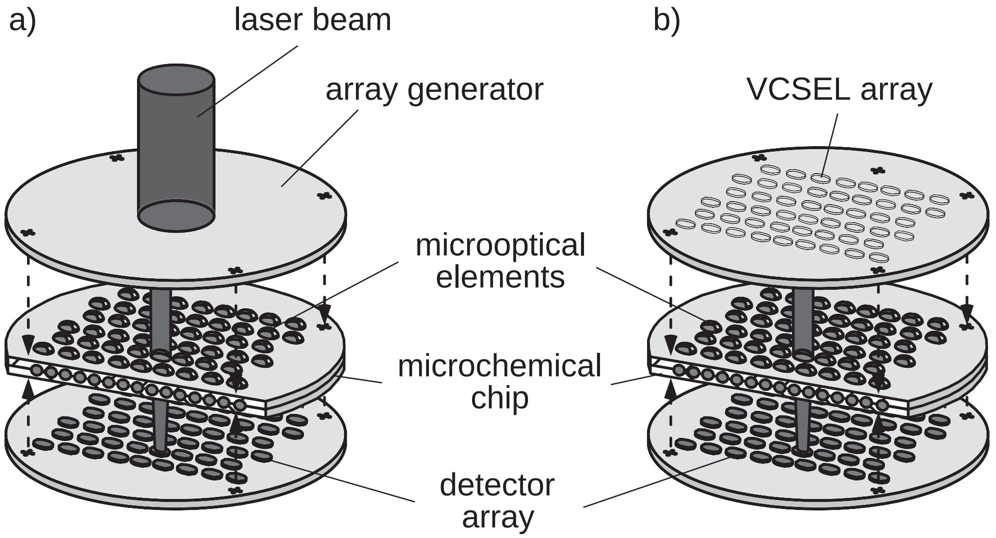

Figure 1.8: System approach. The microoptical elements composing the detection system are directly deposited on both sides of the microchemical chip. The excitation light source and the detector array can then be added. For the sake of clarity, only one beam is show emerging from the array generator (a) and the VCSELs (b).

gives a microfluidic section consisting of a half circle with a flat bottom. The system is completed with a light source, which can either be a laser beam split with the help of an array generator (fan-out) [51, 52], as shown on Fig. 1.8a, or an array of VCSELs (vertical-cavity surface-emitting laser) [53], as shown on Fig. 1.8b. The array generator or the VCSEL array, as well as the detector (which can be an array of photodetectors), can be stacked on both sides of the chemical chip and precisely aligned with respect to the microchip with the help of alignement marks realized during the microfabrication of the microoptical elements. The excitation beam is inserted directly into the chip, and the detection volume is defined by the diameter of the microchannel and by the excitation beam diameter at the level of the microchannel. The system based on VCSELs is more compact than the system with the array generator, but the wavelengths available at the moment (and hence the choice of fluorochromes) are more limited.

The microoptical elements used in this thesis for the realization of the detection systems are aperture, stop and refractive microlens arrays. The apertures and stops are formed by photolithographic techniques into an opaque layer, such as chromium (Chap. 3), and serve to block part of the excitation or fluorescence light. The refractive microlenses formed by melting techniques (Chap. 3) [54, 12, 55] are used for two tasks. The first one is to focus the excitation light into the detection cell/microchannel section and the second one is to collect and transport the fluorescence light to the detector. Figure 1.9 shows the basic elements composing the microchemical and the detection systems as well as the geometrical definitions used in the forthcoming chapters.

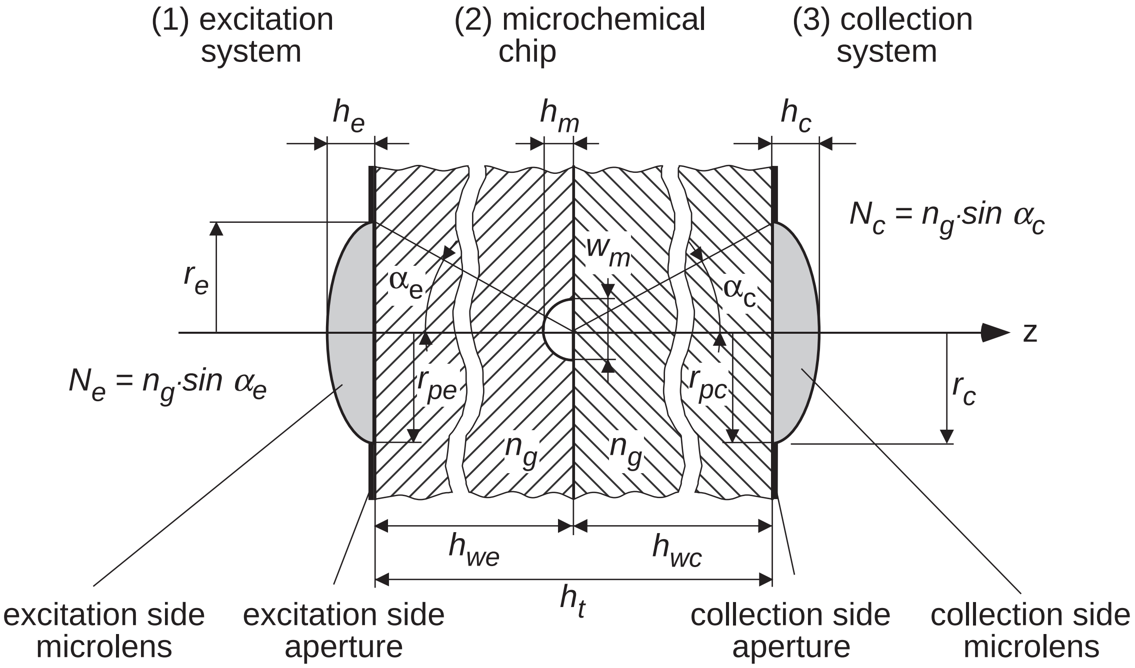

Figure 1.9: Basic elements composing the microchemical and the detection system.

1.6.2 Stack approach

The angular separation of fluorescence light and transmitted excitation light is a relatively easy task with standard optical components, such as microscope objectives, beamsplitters or dichroic mirrors and interference filters. They can be easily combined to realize illumination and collection systems which are perpendicular to one another, or on the same side of the chip, as in confocal microscopy [56]. In these cases, I_T (Fig. 1.7) is only composed of back or side scattered excitation light, which can be easily eliminated by one or more interference filters. Unfortunately, beamsplitters and dichroic mirrors are difficult to integrate onto microchemical chips. Thus, if the excitation and collection systems are placed on the same side of the microchemical chip, the surface occupied by the excitation system is lost for the collection system (or vice versa) which reduces either the amount of fluorescence light collected, and hence the system sensitivity, or the number of channels per chip. The other solution involves the realization of a system with the excitation system from one side of the chemical chip and the detection on the other side. In this case, the excitation and detection systems are completely separated. Unfortunately, the false light reaching the collection system is mainly transmitted excitation light whose intensity is more significant than back or side scattered excitation light. The system therefore requires a better geometric separation between excitation and collection subsystems.

This is why we combine stacks of microlenses and stops to realize excitation configurations which create an angular separation between the non-absorbed excitation light and the fluorescence light. In the case of perfect geometrical separation, the main source of background light I_N is then generated by the scattering of excitation and transmitted light at interfaces, such as microlens and microchannel surface. Since the angular distribution of the scattered light is difficult to control, it must be eliminated by means of an interference filter. Scattering problems can be an important issue for small dimension systems (short distance between scattering sources and detector) and for microfabricated stacked systems (number of interfaces). The number of interfaces should thus be limited and their surface roughness maintained as low as possible. Besides good angular separation and good scattering control, the sensitivity of the system depends also on the insertion efficiency of the excitation beam into the microchannel (I_0 as large as possible for a given light source power), and on the fluorescence light I_F collection efficiency (hence on the NA of the collection part of the detection system).

In summary, the following criteria must be carefully taken into consideration for the implementation of the detection system: efficient separation of false light and fluorescence light, reduction of scattering sources, high excitation beam coupling efficiency, high fluorescence light collection and transport efficiency.

Chapter 2

Micro-optics based detection

2.1 Introduction

As discussed in Sec. 1.5, the detection system integrated onto the chemical chip must enable the separation of the false light intensity from the fluorescence light intensity. Figures 2.1 to 2.3 show how stacks of combined layers of refractive microlenses and stops allow not only the excitation beam to be focused into the detection volume, but also the remaining excitation intensity to be reduced at the detector position by blocking or directing sideways the transmitted excitation beam. These raytracing simulations[1] were performed with the assumption that the refractive index difference between the melted photoresist and the glass substrate (1.62 and 1.47 respectively, at 633 nm) and between the glass substrates and the liquid (water) contained in the microchannel (1.33, at 633 nm) are negligible.

Figure 2.1 illustrates a beam-splitting configuration. As this cross-sectional view shows, the illumination system is composed of two layers of cylindrical microlenses. Two lenses on the top layer split the incoming beam of light, while a third microlens on the second layer focuses the two resulting beams into the probe volume or microchannel. The beams diverge as they leave the chip, producing a dark area a few millimeters behind the chip, where a collection microlens or a photodetector could be placed. The raytracing diagram of Fig. 2.2 presents another excitation scheme. A circular stop blocks the central part of the excitation beam. As in the beam-splitting case, the light is focused into the microchannel and diverges as it leaves the microchip. A collection microlens and/or a detector could be placed in the dark area. An off-axis illumination scheme is a third possibility. In this case, the incoming beam forms an angle of 45° with respect to the surface of the microchip. As can be seen from the raytracing diagram in Fig. 2.3, a first

---

[1] Simulations performed with Raytrace 6.2, developed by N. Lindlein, University of Erlangen, Germany.

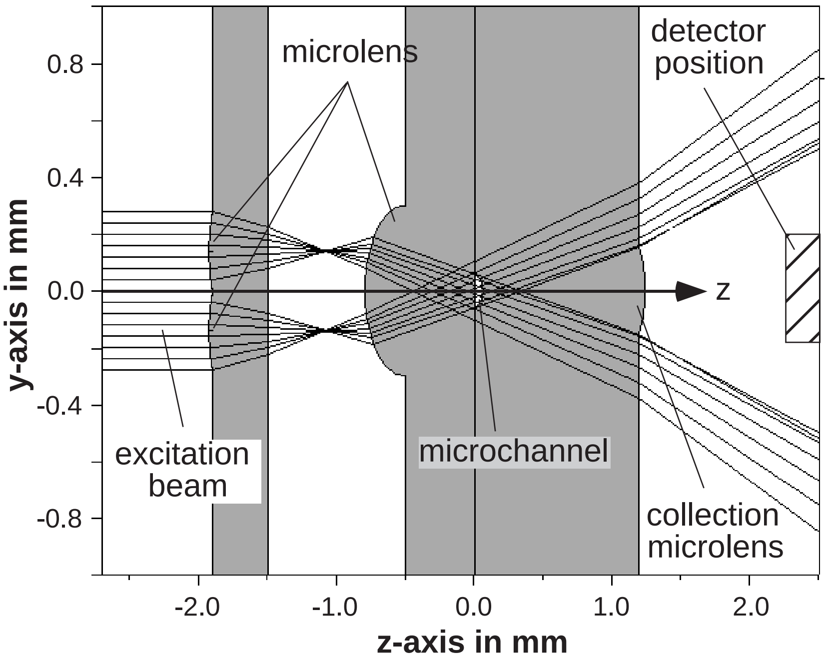

Figure 2.1: 2D raytrace simulation of a beam-splitting illumination system with two layers of microlenses. The first two microlenses are 280 μm wide and 27 μm high (focal length $\sim$ 650 μm). The third microlens on the second layer is 600 μm wide and 100 μm (focal length $\sim$ 800 μm).

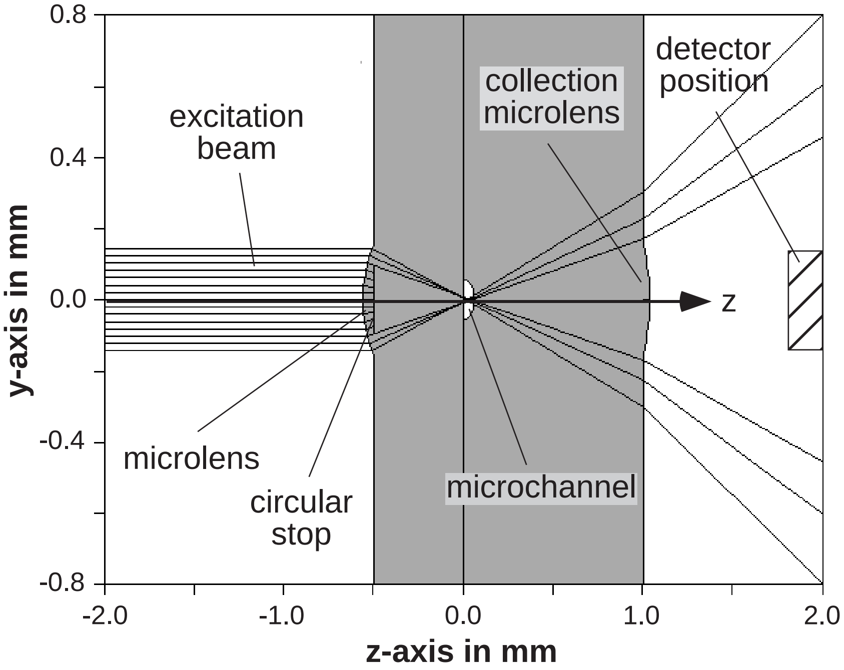

Figure 2.2: 2D raytrace simulation of a central-stop illumination scheme. The microlens is 310 μm wide and 34 μm high (focal length $\sim$ 550 μm). The circular stop has a diameter of 180 μm.

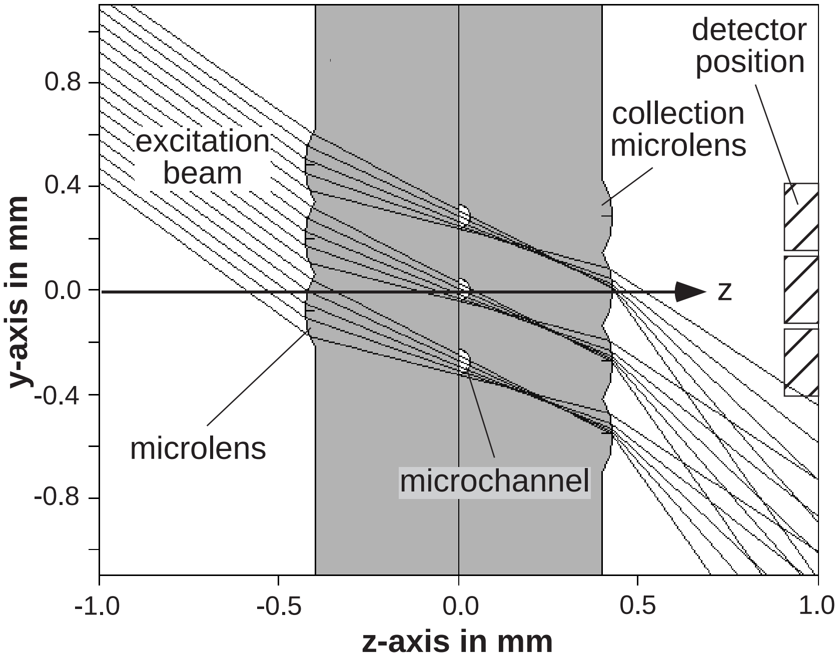

Figure 2.3: 2D raytrace simulation of an off-axis illumination scheme. The microlenses on both layers are 280 μm wide and 26 μm high (focal length $\sim$ 720 μm).

layer of microlenses splits and focuses the beam into several detection microchannels. A second layer of microlenses, deposited on the other side of the microchip, directs the light sideways and also collects and focuses the fluorescence light onto the detector. These three illumination systems can be based either on cylindrical or spherical microlenses, the main difference between the two being the shape of the light spot inside the microchannel. For spherical microlenses the spot is circular, whereas it is a line for cylindrical microlenses. A focal line which permits the excitation of a complete microchannel section could be a way to increase the illumination volume for detection of low fluorochrome concentrations.

In order to get a good optical quality, the fabrication technology imposes that the microlens height is $h_L \leq 120\ \mu m$ and that the microlens radius r_L to height ratio must range between $2 \leq r_L/h_L \leq 7$ (Sec. 3.3.2). In the paraxial approximation (inclination of the rays to the propagation axis sufficiently small), the microlens radius of curvature R is given by [57]

$$R \simeq \frac{n_2 - n_1}{\frac{n_1}{Z_1} + \frac{n_2}{Z_2}}, \tag{2.1}$$

where n_1 and n_2 are the refractive indices of the medium before and after the microlens surface. As shown in Fig. 2.4, Z_1 and Z_2 are the distances between the first and the second conjugate plane, respectively, and the microlens boundary. The radius of curvature R can also be expressed as a function of r_L and h_L in the form of

$$k\,R = \frac{r_L^2}{2\,h_L} + \frac{h_L}{2}, \tag{2.2}$$

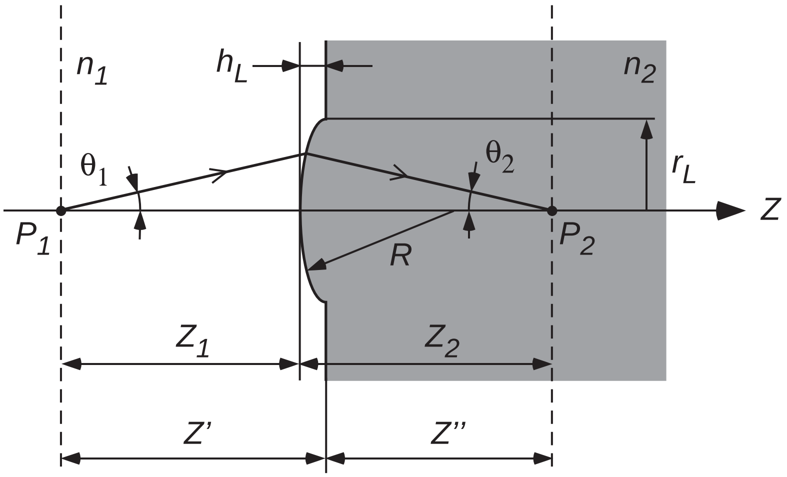

Figure 2.4: Refraction at a spherical boundary. In the paraxial approximation ϑ_1 and ϑ_2 are small.

with $k = 1$ for convex boundary, and $k = -1$ for concave boundary. Assuming that either the microlens is to be transferred into the glass substrate or that the refractive index difference between the melted photoresist and the glass substrate is negligible, the microlens radius can be obtained by replacing Z_1 and Z_2 in Eq. (2.1) by $Z' - k\,h_L$ and $Z''_L + k\,h_L$, respectively (Z' and Z'' being the distance between the conjugate planes and the microlens base which is the surface of the chip). Equations (2.1) and (2.2) can be combined to give

$$r_L = \sqrt{2\,h_L \left(\frac{k\,(n_1 - n_2)}{\frac{n_1}{Z' - k\,h_L} + \frac{n_2}{Z_2 + k\,h_L}} - \frac{h_L}{2} \right)}. \tag{2.3}$$

Since $2 \leq r_L/h_L \leq 7$, an approximation of the maximum microlens radius r_{max} for a given chip geometry Z' and Z'', can be found by solving Eq. (2.3) with $h_L = r_L/2$.

2.2 Beam-splitting illumination scheme

2.2.1 Demonstration of feasibility

The beam-splitting concept (Fig. 2.1) was realized with "off-the-shelf" components (i.e. microlenses optimized for other applications). The first two microlenses are 280 μm wide and 27 μm high (focal length $\sim$ 650 μm). The third microlens on the second layer is 600 μm wide and 100 μm (focal length $\sim$ 800 μm). Ideally, the microlens diameter and focal length should be adjusted to the thickness of the glass substrates in which the microchannels are formed, to ensure a maximum excitation intensity in the channel. The cylindrical microlenses used here were deposited on two 25 $mm \times 25$ mm glass plates 0.5 mm in thickness. The plates were assembled by precise alignment under a microscope followed by bonding using a UV-curable glue. Spacers (square pieces cut in a 1 mm thick glass wafer) and a transparency sheet, on which a pattern of apertures was printed, were inserted between the two plates. The purpose of this pattern was to block the light passing around the microlenses.

The photographs in Fig. 2.5 show the first plate with the two cylindrical microlenses and the intensity distribution of the excitation beam in a plane perpendicular to the z-axis and at different points within and behind the assembly. A 10 mW $HeNe$ laser was used for the excitation. The beam was expanded and collimated. The intensity distribution behind the systems was measured by means of a diffusing screen placed in front of a CCD camera. The images taken behind the layer which would normally contain the microchannels clearly show that the exiting beams diverged rapidly. The distance between the two beams increased from 0.45 mm at 1 mm distance from the chip to about 2 mm at 5 mm. The false light intensity behind the collection microlens (where the detector would be placed) was mainly the result of the fact that the aperture layer was not completely opaque. Despite some excitation light passing between the two first microlenses, the intensity was still about 10 times weaker than on the sides (Fig. 2.6). The excitation volume would be given here by the microchannel cross-section and the excitation spot dimension along the microchannel (i.e. by the length of the cylindrical microlens). For a microchannel 110 μm wide and 50 μm deep and a spot length of ~ 2.1 mm, the excitation volume would be ~ 8 nL. For a system based on a spherical microlens having the same focal length, the excitation volume would be reduced to ~ 3 nL.

2.2.2 System discussion

The beam-splitting scheme does not block any part of the excitation beam, unlike the central stop detection system. Therefore, more light intensity is available for generation of fluorescence. On the other hand, the excitation part of the detection system requires two layers of apertures and microlenses. The number of interfaces (i.e. straylight sources) is hence higher than for the other systems and the two layers of microlenses make the beam-splitting scheme more complex and difficult to realize than the off-axis and the central stop excitation systems.

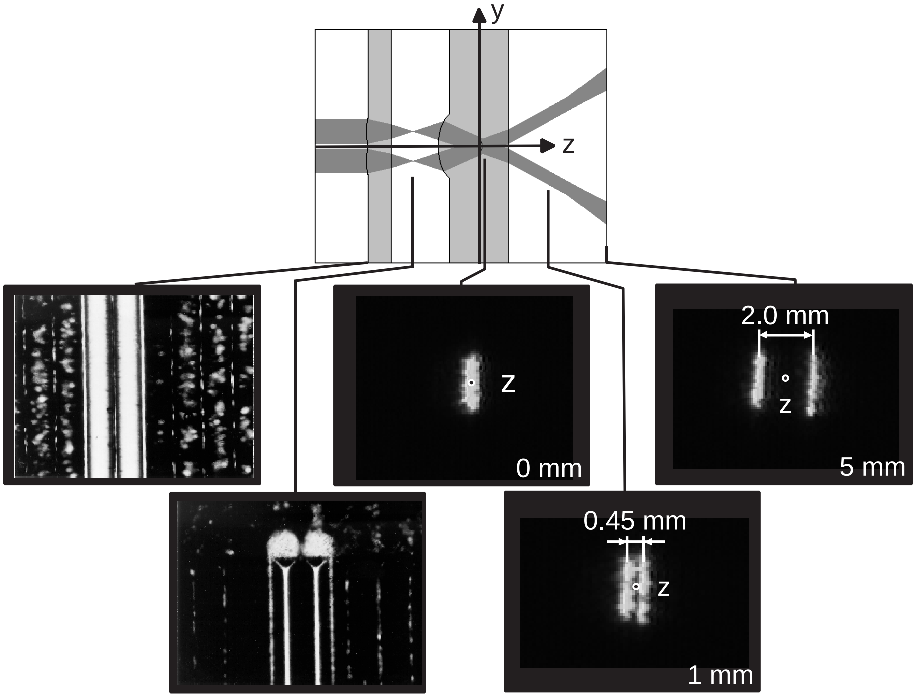

Figure 2.5: Top picture: illumination scheme of the beam-splitting illumination system. Five bottom pictures show (from left to right): first layer of cylindrical microlenses, focal lines situated between the two optical ayers, focus spot (probe volume) and diverging beams at 1 *mm* and 5 *mm* away from the probe volume.

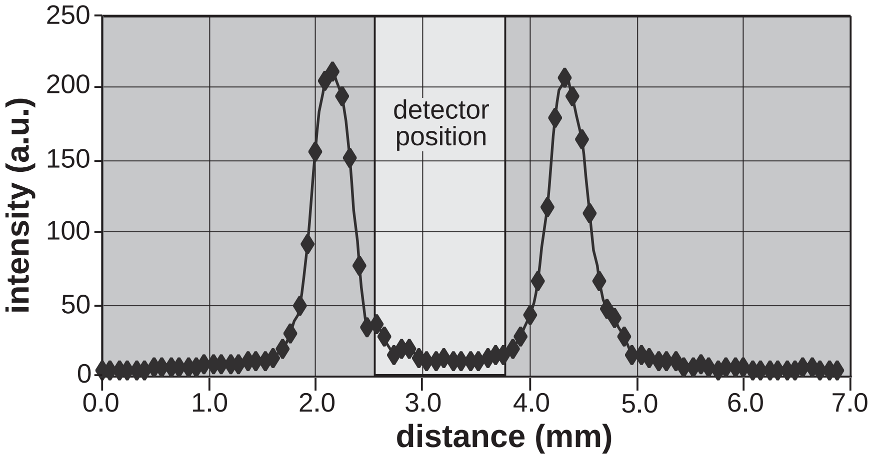

Figure 2.6: Line plot of the intensity distribution in a plane situated 5 *mm* away from the focal plane. The scan was taken along the y-axis, normal to the optical axis.

2.3 Central stop system

2.3.1 Demonstration of feasibility

The system with a central stop (chromium) was realized on a single glass wafer (diameter of 100 mm and thickness of 0.5 mm). The microlens is 310 μm wide and 34 μm high (focal length $\sim$ 550 μm). The circular stop has a diameter of 120 μm. As for the beam-splitting system, the intensity distribution behind the systems was measured by means of a diffusing screen placed in front of a CCD camera, with the same excitation intensity (10 mW) as described previously. The first photo from the left in Fig. 2.7 shows the microlenses with stops at their centers. On the following photographs, the intensity distribution of the excitation beam passing through the system can be observed. The light is first focused onto a spot where the probe volume would be placed and then diverges as it leaves the chip. A dark circular area with a radius of 0.4 mm is created in a plane perpendicular to the z-axis 3 mm away from the surface of the chip. There, as shown in Fig. 2.8, the intensity at the detector position is between 6 to 7 times weaker than on the sides. As it is clearly shown in Fig. 2.7, the light which is not focused by the microlens (bright outer ring) increases the false light. Again the solution to this problem is the integration (during the same fabrication step) of apertures in the chromium layer having the same diameter as the microlens.

Unlike the other systems, the excitation microlens is circular. The excitation volume is then given by the microchannel depth and the excitation spot radius (as long as the spot diameter does not exceed the width of the microchannel). For a spot radius of $\sim$ 40 μm and a 110 μm wide, 50 μm deep microchannel, the excitation volume would be $\sim$ 250 pL.

2.3.2 System geometry optimization

According to the criteria defined in Sec. 1.6.2, further geometrical raytrace simulations were carried out in order to determine the optimal geometry of the central stop system. The parameters which could be varied included (1) thickness of the two wafers comprising the microchemical chip, (2) the orientation of the microfluidic channel with respect to the excitation light propagation axis, (3) the stop radius, (4) the surface of the microchemical chip on which the stop is deposited (excitation side or collection side), and finally, (5) the dimensions of the excitation and collection microlenses.

To limit the number of possibilities, only three glass wafer thicknesses h_w were taken into consideration, namely 500 μm, 1000 μm and 1500 μm. These are commonly available thicknesses and such wafers can be easily processed on microfabrication equipment. This

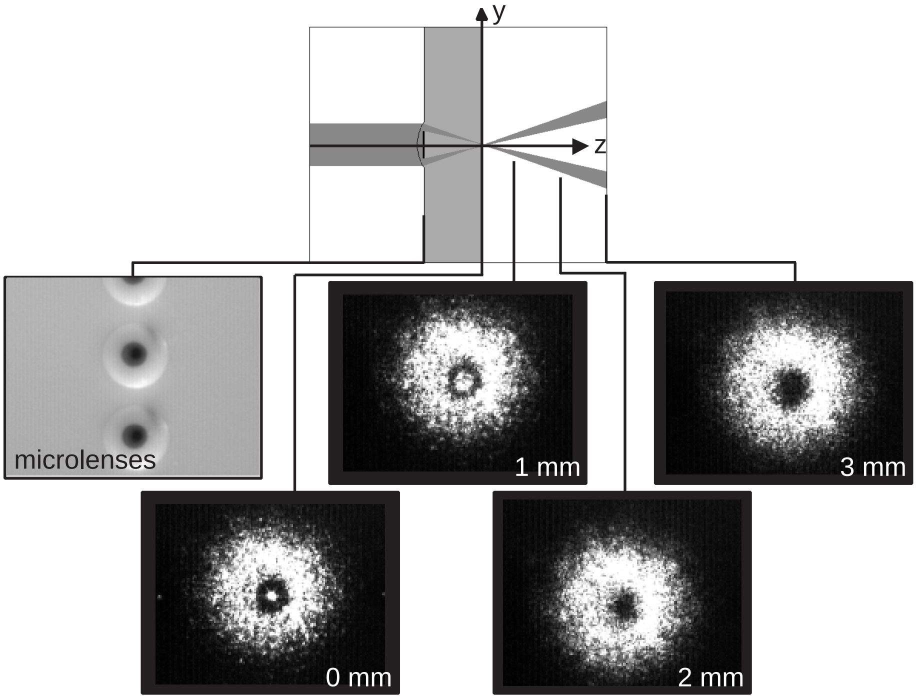

Figure 2.7: Top picture: illumination scheme of the central stop illumination system. Five bottom pictures show (from left to right): spherical microlens array with chromium stops, exiting beam at 0 *mm*, 1 *mm*, 2 *mm* and 3 *mm* away from the focal plane. The bright corona around the dark area is due to the light passing around the microlens.

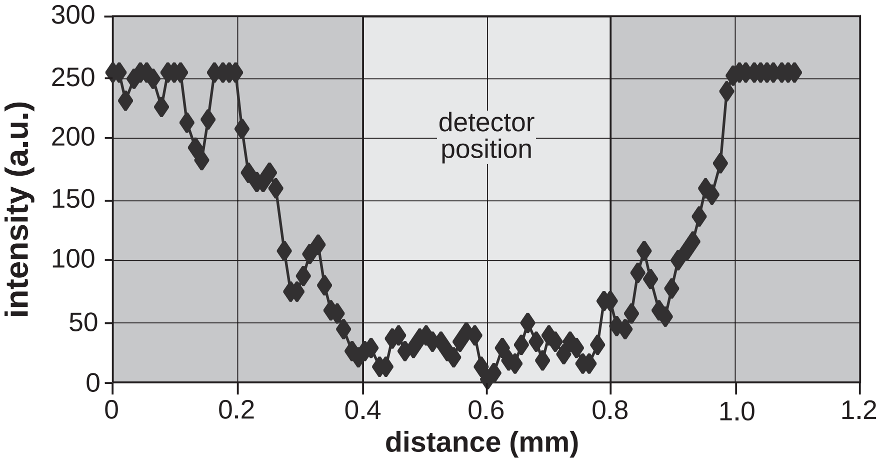

Figure 2.8: Line plot of the intensity distribution in a plane situated 3 *mm* away from the focal plane. The scan was taken along the y-axis, normal to the optical axis.

is not the case for thinner and thicker wafers. The orientation of the microchannel can be simulated as if etched on the left (excitation side) or on the right wafer (collection side). When the microchannel is etched in the excitation side wafer, the excitation beam first meets a cylindrical convex surface, then a flat surface. When the microchannel is etched on the collection side wafer, the excitation beam first meets the flat surface, then a cylindrical concave surface. According to the manufacturer's data sheets, the refractive index of melted photoresist n_p and Pyrex glass wafer n_g are 1.62 and 1.47, respectively, at 633 nm. The simulations are realized with the assumption that the microchannel has a semi circular profile with a radius of 30 μm. The microchannel is assumed to be filled with water (refractive index 1.33 at 633 nm).

As discussed in Sec. 1.6.2, the excitation beam coupling efficiency must be as good as possible to ensure maximum excitation intensity in the microchannel. An excitation side microlens with a large radius is thus favorable for good coupling of the excitation beam into the microchannel. The excitation microlens radius is thus set at 250 μm. This is the biggest microlens technically realizable (Chap. 3) with a focal length equal to the thinner glass wafer (500 μm). Larger microlenses would not be capable of focusing all of the excitation beam into the microchannel, and hence part of the excitation power would be lost. To avoid the photobleaching (destruction of fluorochrome molecules by a high excitation intensity in a small volume), the focal length of the excitation side microlens is chosen slightly shorter or longer (depending on the detection system geometry) than the distance between the excitation side chip surface and the center of the microchannel. The excitation spot diameter is then larger at the level of the microchannel than in the focal plane, reducing the excitation power per unit volume. The diameter of the spot is limited to $\sim 70\,\%$ of the microchannel width to avoid excitation beam scattering problems at the rim of the microchannel in case of bad alignment between the excitation microlens and the microchannel.

In this illumination scheme, the numerical aperture NA_c of the collection side microlens (and hence the amount of fluorescence light collected) increases proportionally with the stop radius r_s. Hence, for a given stop and excitation microlens radius r_e, NA_c should be maximum for the 500 μm thick excitation side glass wafer h_{we} and decrease for the thicker wafers. Figure 2.9 shows that except for a stop radius to microlens radius ratio $r_s/r_e = 0.9$ (i.e. for a stop radius almost equal to r_e), the best NA_c is obtained for the 1000 μm thick wafer rather than for the 500 μm thick one. Since the excitation side wafer is thin, the microlens focal length must be short in order to focus the excitation rays into the microchannel. The height to radius ratio of the microlens must then be chosen to the lower technical limit ($h_e/r_e = 1.9$). The microlens radius of curvature is hence important, and except when the most external rays are used for fluorochrome excitation ($r_s/r_e = 0.9$), the focused beam suffers from spherical aberrations which increase the beam dispersion and hence reduce the space available for the collection microlens.

Obviously, increasing the stop radius increases the surface which is free of outgoing rays on the right surface of the chip where the detection microlens is placed, and hence increases NA_c. Unfortunately, the excitation power which is lost in the stop (blocked) increases as well. Figure 2.10 shows that the best compromise between the power available for fluorochrome excitation and the power collected is obtained for a stop radius of $r_s = 175\ \mu m$ ($r_s/r_e = 0.7$) for an excitation side wafer thickness of $h_{we} = 1000\ \mu m$. The excitation power P_e usable for fluorochrome excitation is given by the integral of the optical intensity $I(\rho, z)$ over a transverse plane perpendicular to the light propagation axis z [57],

$$P_e = \int_{\varphi=0}^{2\pi} \int_{\rho=0}^{\infty} I(\rho, z)\, \rho\, d\varphi\, d\rho, \tag{2.4}$$

where ρ is the radial distance from the propagation axis to a point, and φ the angle formed by ρ and a reference axis, in the considered perpendicular plane. For a beam having a constant intensity distribution, $I(\rho, z) = I_0$, and the total optical power carried within a circular microlens of radius r_L is

$$P_m = \pi\, I_0\, r_L^2. \tag{2.5}$$

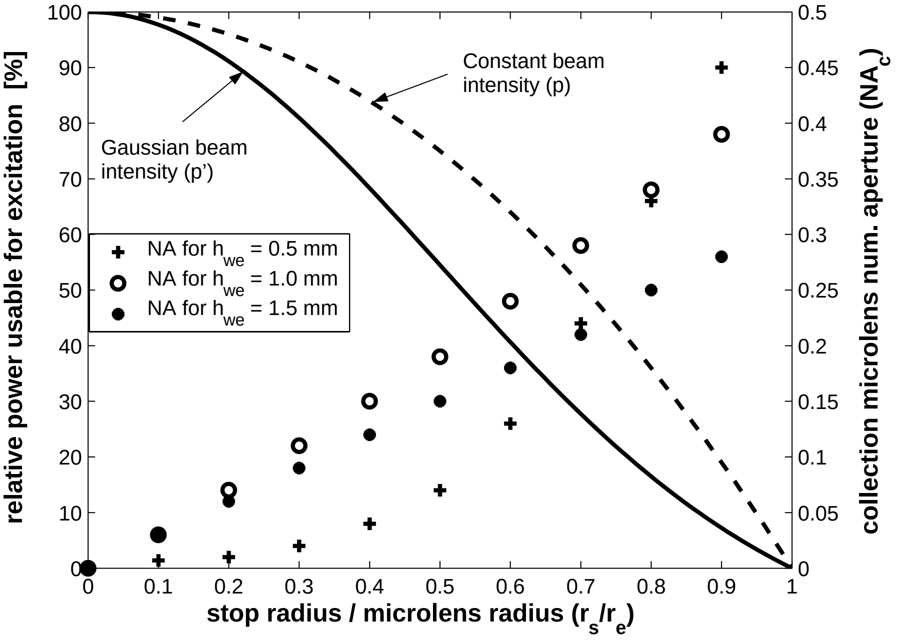

Figure 2.9: Excitation power usable for fluorochrome excitation (left) and (right) numerical aperture of the collection microlens as a function of the stop to microlens radius ratio r_s/r_e (excitation microlens radius 250 μm).

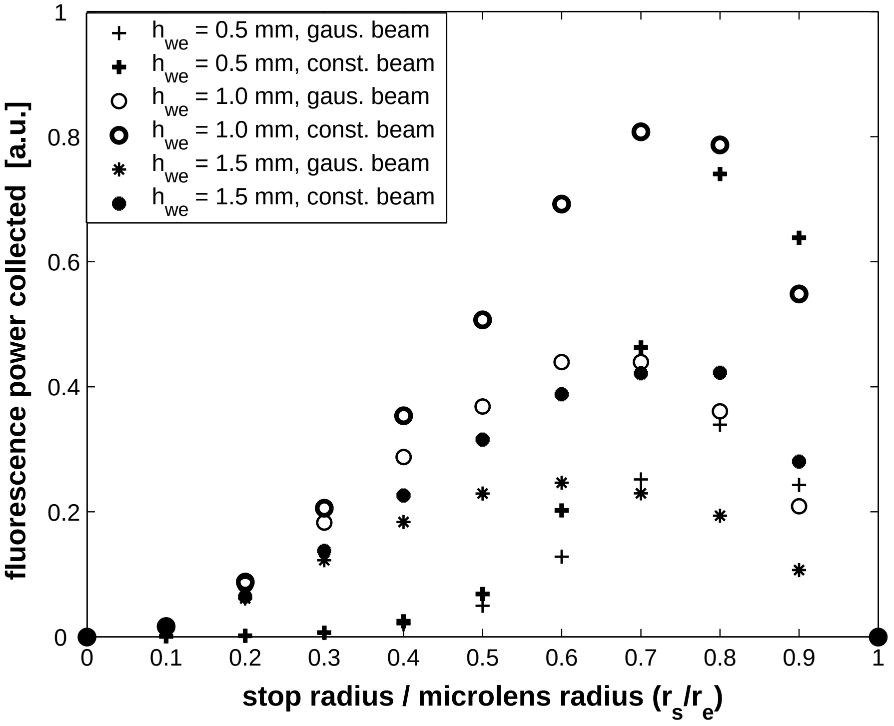

Figure 2.10: Fluorescence light power collected as a function of the stop to microlens radius ratio r_s/r_e.

The power which is blocked by a circular stop of radius r_s is

$$P_s = \pi\, I_0\, r_s^2. \tag{2.6}$$

The ratio of power usable for fluorochrome excitation to the total power is then

$$p = \frac{P_m - P_s}{P_m} = \left[1 - \left(\frac{r_s}{r_L}\right)^2\right]. \tag{2.7}$$

For a beam having a Gaussian intensity distribution,

$$I(\rho, z) = I_0' \left(\frac{W_0}{W(z)}\right)^2 \exp\left(-\frac{2\,\rho^2}{W^2(z)}\right), \tag{2.8}$$

where W_z is the beam radius at the level of the excitation microlens and W_0 (for $z = 0$) the minimum value of W_z in the plane perpendicular to the beam propagation. The total optical power carried within a microlens of radius r_L is

$$P_m' = \frac{\pi}{2}\, I_0'\, W_0^2 \left[1 - \exp\left(\frac{-2\, r_L^2}{W_z^2}\right)\right]. \tag{2.9}$$

Similarly, the power which is blocked by a stop of radius r_s is given by

$$P_s' = \frac{\pi}{2}\, I_0'\, W_0^2 \left[1 - \exp\left(\frac{-2\, r_s^2}{r_L^2}\right)\right]. \tag{2.10}$$

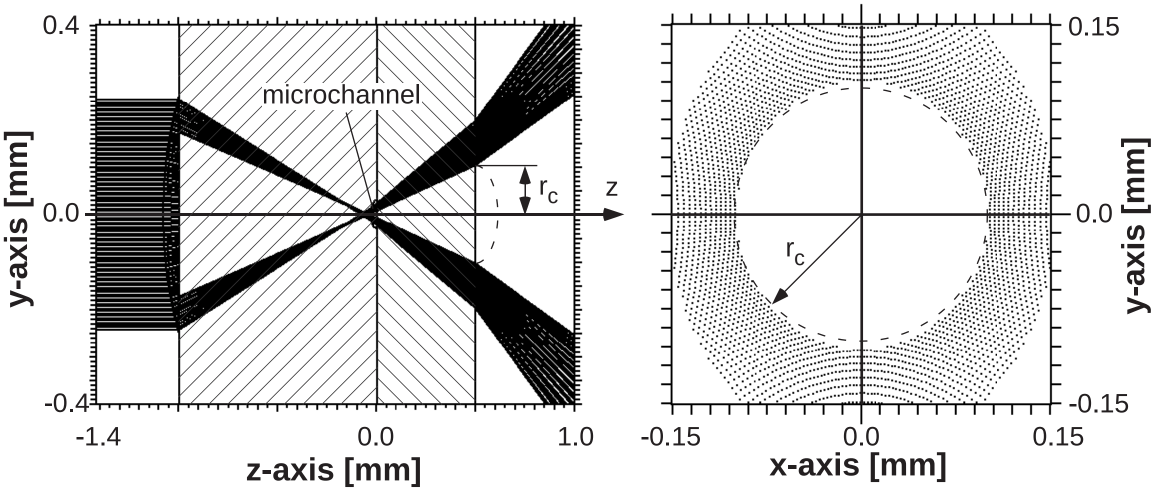

Figure 2.11: Raytrace simulation for the central stop system, stop placed on the excitation side. For the sake of clarity, only the rays passing through a 100 μm wide slit (along the x-axis) are shown on the left picture (yz-plan). The right picture shows the excitation ray distribution on the collection side surface of the chip (xy-plan).

Assuming that the beam waist radius is equal to the microlens radius ($W_z = r_L$) at the level of the excitation microlens, and assuming that the total power carried within the microlens for Gaussian and constant beam distributions are equal, the ratio of power usable for fluorochrome excitation to the total power is

$$p' = \frac{P'_m - P'_s}{P'_m} = \frac{\left[\exp\left(\frac{-2\,r_s^2}{r_L^2}\right) - \exp\left(-2\right)\right]}{\left[1 - \exp\left(-2\right)\right]}. \tag{2.11}$$

The relative excitation intensities for the two types of beams can then be calculated from Eqs. (2.7) and (2.11). Assuming that all the power which is not blocked by the stop is used for fluorochrome excitation, the collected fluorescent light intensity I_c, and hence the power, can then be calculated with the help of Eq. (1.11).

Figure 2.11 shows the raytrace simulation for a system with an excitation microlens radius of 250 μm (height of 79 μm) and a stop radius of 175 μm ($r_s/r_e = 0.7$). The excitation side wafer is 1000 μm thick. The collection side wafer is 500 μm thick. The microchannel is placed along the x-axis and is if etched on the excitation side wafer. The ratio r_e/h_e is ~ 3.1. As shown on the right raytrace diagram of Fig. 2.11, the excitation ray distribution at the level of the collection side of the chip allows the deposition of a collection microlens with a radius $r_c = 125$ μm. The numerical aperture is $NA_c = 0.29$, as calculated from the results of the simulation using Eq. (1.8). The cylindrical shape of the microchannel influences only slightly the distribution of the rays.

A variant of the central stop system is to deposit the stop on the other side of the microchemical chip. As shown in the left picture of Fig. 2.12, the excitation beam is focused through the microchannel onto a stop, centered with respect to the collection microlens. In comparison with the previous system, all the excitation light carried within the excitation microlens is used for fluorochrome excitation. The collection microlens radius r_c is now limited only by microfabrication technology (Sec.3.3.2) and no longer by the distribution of outgoing excitation rays. The drawback of this system is that some fluorescence light is blocked by the stop and hence lost. To collect as much fluorescence light as possible, the stop must be as small as possible. Therefore, the raytrace simulations must be carried out to find the smallest excitation spot radius at the level of the collection side interface. Figure 2.12 shows the result of these simulations.

The excitation side microlens radius was chosen equal to the previous system ($250\ \mu m$) and its height was $47\ \mu m$ ($r_e/h_e \simeq 5.4$). The thickness of the excitation side wafer is $h_{we} = 1500\ \mu m$; one then gets an excitation microlens with a more favorable ratio r_e/h_e and hence with less spherical aberrations. The collection side wafer is $h_{wc} = 500\ \mu m$ thick. The microchannel is placed along the x-axis as if etched on the excitation side wafer. The right picture of Fig. 2.12 shows that the size of the stop along the x-axis C_x and the y-axis C_y must be $C_x = 120\ \mu m$ and $C_y = 12\ \mu m$, respectively. In contrast to the previous system, the microchannel influences the distribution of the rays at the stop position. The microchannel acts like a cylindrical microlens which focuses the rays only along the y-axis. For limited stop size, placed along the z-axis, the non-blocked part of collected fluorescence light p_u can be evaluated by

$$p_u = \frac{A_m - A_s}{A_m}, \tag{2.12}$$

where A_m is the microlens base area and $A_s = C_x \cdot C_y$ is the stop area. Since the microlens is only limited by microlens fabrication technology, its maximum radius is hence (Sec. 3.3.2) $240\ \mu m$ ($NA_c = 0.64$) and the fluorescence light lost in the stop is negligible ($p_u > 99\,\%$).

Compared to the illumination system with the stop on the excitation side, this version is more efficient (no excitation power blocked and very low collected fluorescence light lost). The excitation beam is focused parallel to the z-axis at the center of the collection microlens, and hence this detection system is more sensitive to the scattering of the excitation beam at interfaces, especially at the level of the microchannel, than for the previous version of the stop system where the excitation beam is directed sideways. Since the size and shape of the stops are different in the two systems, requiring two different photolithographic masks, experiments were carried out only for the system with the stop on the excitation side, for which the mask was already available.

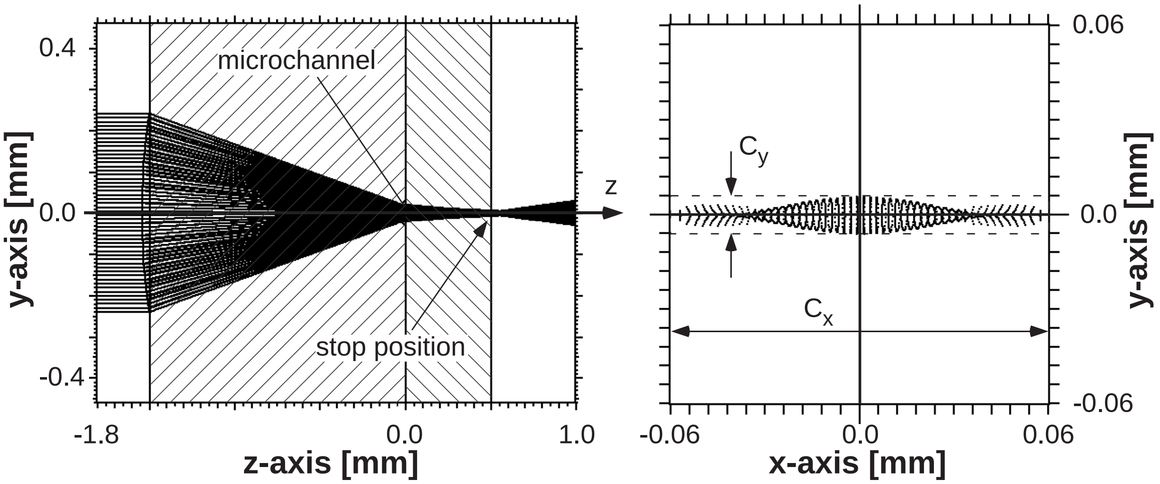

Figure 2.12: Raytrace simulation for the stop system, stop placed on the collection side. The stop is not present in the simulation. For the sake of clarity, only the rays passing through a 100 μm wide slit (along the x-axis) are shown on the left picture (yz-plane). The right picture shows the excitation ray distribution on the collection side surface of the chip (xy-plane).

2.4 Off-axis illumination scheme

2.4.1 Demonstration of feasibility

The off-axis illumination concept presented in Fig. 2.3 was realized using "off-the-shelf" glass plates with cylindrical microlenses, as for the beam-splitting scheme. The plates were aligned under a microscope and glued together with UV-curable glue.

The same light source (a 10 mW expanded and collimated $HeNe$ laser) was used for the excitation, and the intensity distribution behind the systems was measured by means of a diffusing screen placed in front of a CCD camera. Figure 2.13 shows a sequence of photographs of the microlens stack, the light distribution at the level of the second layer of microlenses, and the intensity distribution along the z-axis in perpendicular planes at various distances from the surface. The distance between the center of the exiting beam (light spot) and the z-axis (photodetector position) increased from 0 mm to 4.8 mm as the diffusing screen was moved from 1 mm to 10 mm away from the chip.

As Fig. 2.14 testifies, the intensity at the detector position is about 4 times weaker than in the exiting beam positions at a distance of 5 mm from the chip. The false light is mainly generated by the light passing through the gap between the microlenses or scattered at the rim of the microlenses. The integration of apertures could improve the separation of false light from fluorescence light. As in the previous system, the excitation is given by the microchannel cross-section and the excitation spot dimension along the microchannel. This yields the same excitation volume of $\sim 8\ nL$ as for the beam splitting

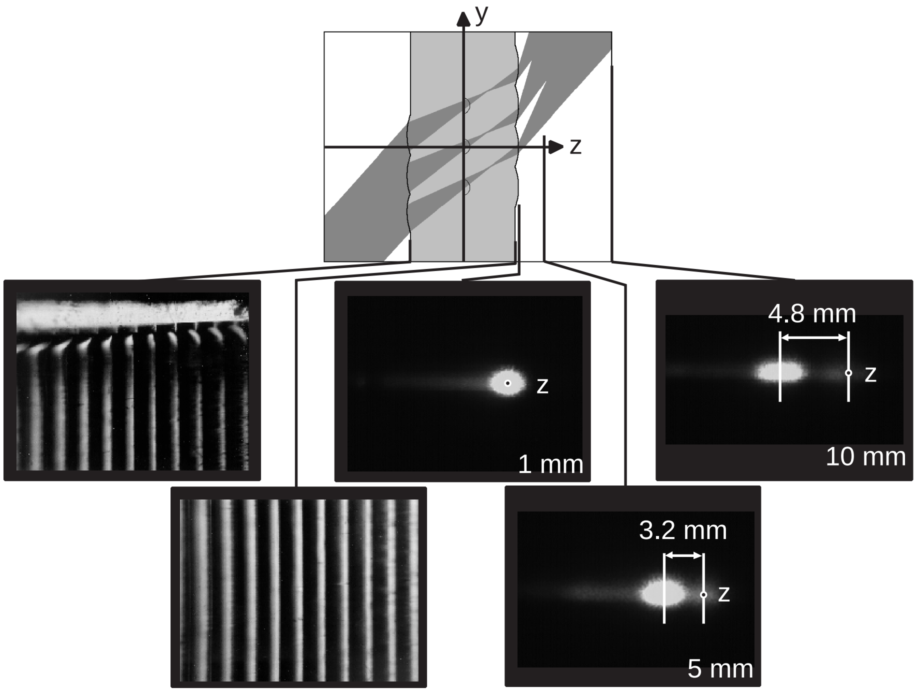

Figure 2.13: Top picture: illumination scheme of the off-axis illumination system. Five bottom pictures show (from left to right): stack of cylindrical microlens array, exiting beams moving sideway from the detection axis at about 3 *mm* and 10 *mm* away from the surface of the chip.

illumination (Sec. 2.2.1). For a spherical excitation microlens having the same focal length and for the same microchannel dimensions (110 μm wide and 50 μm deep), the excitation volume would be reduced to $\sim 400\ pL$.

2.4.2 System geometry optimization

The off-axis detection systems discussed below differ slightly from the demonstrator system presented in Figs. 2.3 and 2.13. As shown on Fig. 2.15, the difference lies in the microchannel orientation (placed now along the y-axis whereas it was placed along the x-axis previously), and in the fact that collection side microlenses are no longer used to redirect the outgoing excitation rays; These are blocked by an aperture array instead. The number and spacing of consecutive parallel microchannels is hence no longer limited by the outgoing excitation rays.

Due to the fact that the incident angle is different from 0°, the focused beam suffers from astigmatism (the focal length in the yz-plane is slightly longer than the focal length in the xz-plane) which increases the spreading of the excitation beam and hence the size of

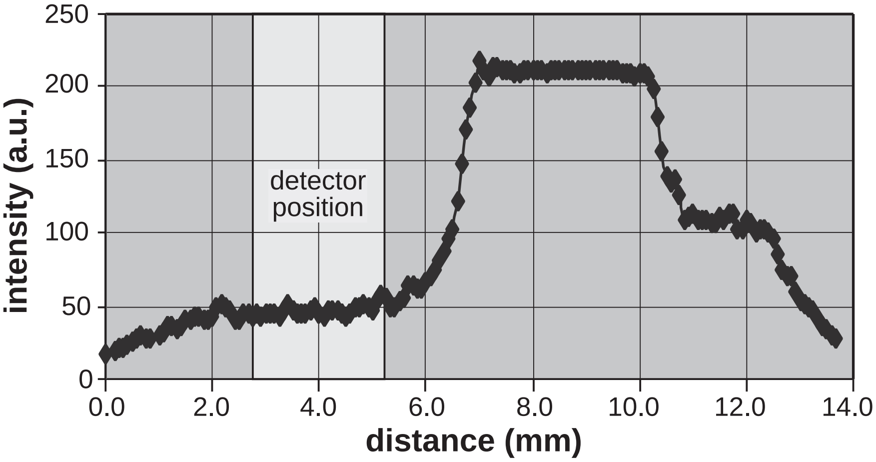

Figure 2.14: Line plot of the intensity distribution in a plane situated 5 mm away from the focal plane. The scan was taken along the y-axis, normal to the optical axis.

the excitation beam spot on the collection side of the chip. As shown on the right raytrace diagram of Fig. 2.15, the radius of the aperture r_{pc}, and hence of the collection microlens radius r_c, are limited by the excitation beam spot size and position. To get r_c and r_{pc} as large as possible, and thus increase the off-axis detection sensitivity, a first possibility is to increase the incident angle. However, this would result in larger aberrations, which makes the focusing of the excitation rays into the microchannel more difficult and increases the size of the excitation beam spot on the collection side. The amount of power coupled into the chip would therefore decrease as the incident angle increases. According to Eq. (2.4), and assuming that the entrance pupil is defined by the excitation microlens rim, the optical power carried within a microlens of radius r_L is

$$P_e = \int_{\varphi=0}^{2\pi} \int_{\rho=0}^{\rho} I(\rho, z)\, \rho(\varphi)\, d\varphi\, d\rho. \tag{2.13}$$

where $\rho(\varphi)$ is the distance from the center to the rim of the ellipse formed by the projection of the microlens onto a plane perpendicular to the excitation beam. The relation between $\rho(\varphi)$, r_L, and the incident angle θ is

$$\rho(\varphi)^2 = \frac{r_L^2 \left(1 - \sin^2\theta\right)}{1 - \sin^2\theta\, \cos^2\varphi}. \tag{2.14}$$

In the case of a constant intensity distribution $I(\rho, z) = I_0$, Eq. (2.13) becomes

$$P_m = I_0 \int_{\varphi=0}^{2\pi} \int_{\rho=0}^{\rho} \rho(\varphi)\, d\varphi\, d\rho. \tag{2.15}$$

By replacing $\rho(\varphi)$ in Eq. (2.15) by Eq. (2.14) and integrating, the power enclosed in the excitation microlens (for a constant beam intensity distribution) is then given by

$$P_m = I_0\, \pi\, r_L^2\, \cos\theta. \tag{2.16}$$

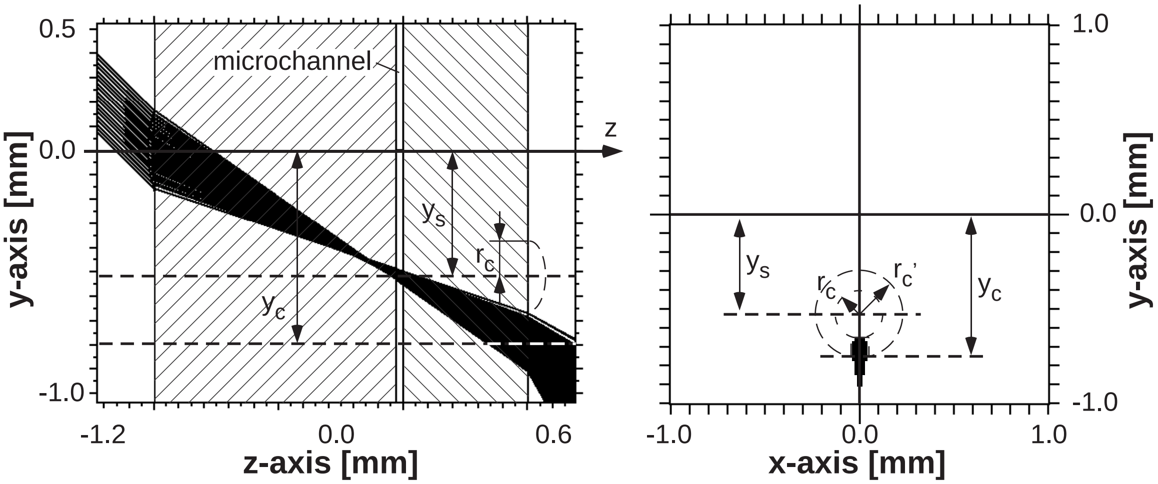

Figure 2.15: Off-axis illumination system. For the sake of clarity, only the rays passing through a 100 μm wide slit (along the x-axis) are shown on the left picture (yz-plane). The right picture shows the excitation ray distribution on the collection side surface of the chip (xy-plane). The collection microlens radius r_c could be increased to r_c' by using a rectangular stop which blocks the light at the bottom of the microlens. The microchannel is along the y-axis.

For a beam with a Gaussian intensity distribution (Eq. (2.8)), Eq. (2.13) can be written as

$$P_m' = 4\, I_0' \left(\frac{W_0}{W(z)}\right)^2 \int_{\varphi=0}^{\frac{\pi}{2}} \int_{\rho=0}^{\rho} \rho(\varphi)\, \exp\left[-2\left(\frac{\rho(\varphi)}{W(z)}\right)^2\right] d\varphi\, d\rho. \tag{2.17}$$

Replacing $\rho(\varphi)$ in Eq. (2.17) by Eq. (2.14) and integrating, one gets

$$P_m' = -I_0'\, W_0^2 \left\{\frac{\pi}{2} - \int_{\varphi=0}^{\frac{\pi}{2}} \exp\left[\frac{-2\, r_L^2 \left(1-\sin^2\theta\right)}{W(z)^2 \left(1-\sin^2\theta\cos^2\varphi\right)}\right] d\varphi\right\}, \tag{2.18}$$

which can be calculated numerically. Figure 2.16 presents the relative excitation power as a function of the incident angle θ for a constant intensity distribution ($P_m(\theta)/P_m(\theta=0)$) and a Gaussian intensity distribution ($P_m'(\theta)/P_m'(\theta=0)$). The maximum numerical aperture of the collection microlens, as a function of θ, is also shown. The reason why NA_c does not keep on increasing with θ is that the excitation microlens dimensions are optimized for an incident angle of 45° (System of Fig. 2.15). The collected fluorescence light intensity I_c, and hence the fluorescence light power, can be evaluated by means of Eq. (1.11) and the result is presented in Fig. 2.17. As expected, the best incident angle is 45°, angle for which the system was optimized.

Another solution for increasing the collection microlens radius (and hence the NA_c) is to reduce the radius of the excitation microlens r_e. Again, the reduction of the microlens size makes efficient power coupling more difficult. A third and better possibility is to use an asymmetrical aperture with a square or a flat edge surface on the collection microlens

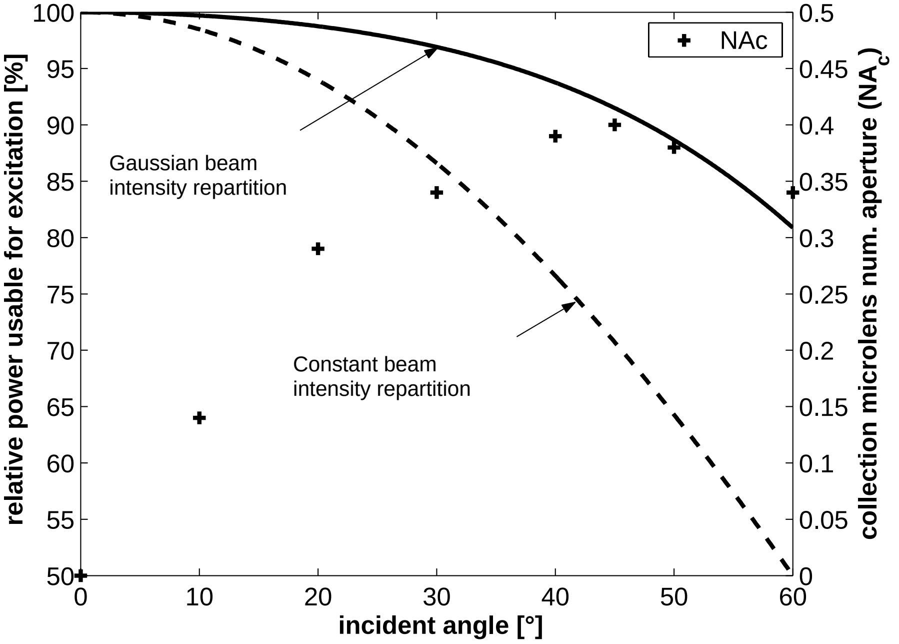

Figure 2.16: Percentage of the excitation power and numerical aperture NA_c of the collection microlens as a function of the incident angle θ.

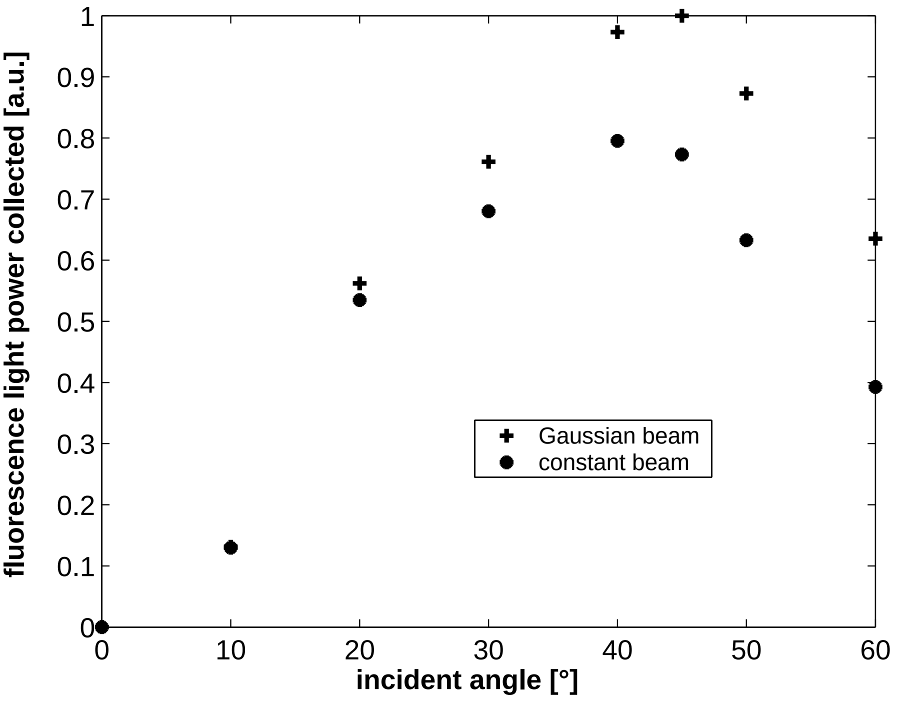

Figure 2.17: Fluorescence light collected as a function of the incident angle.

and blocking the outgoing rays. In this way, the microlens radius r'_c can be increased to the maximum technically feasible radius (Sec. 2.1).

The system presented in Fig. 2.15 is the detection system implemented onto microchemical chips which the fabrication is described in Chap. 3. The excitation side microlens ($r_e = 175\ \mu m$) is smaller than the maximum radius possible but was chosen to give an excitation power (for a constant distribution intensity (Eq. (2.5)) of the same magnitude as the stop system presented in Fig. 2.11. The thickness of the excitation side wafer was $h_{we} = 1500\ \mu m$, which gives a better r_c/h_c ratio ($r_c/h_c = 7$). The collection microlens radius is $r_c = 110\ \mu m$ and is taken equal to the maximum circular aperture radius r_{pc} possible.

2.5 Comparison of the illumination systems

2.5.1 Choice of the illumination system

Even if the performance of the beam-splitting illumination system was promising (Fig. 2.6), only the both variants of the central stop and the off-axis illumination systems were chosen for further investigations. The reason was they require only one microoptical element layer on the excitation side and hence are simpler to realize, whereas the beam-splitting illumination system requires two microoptical element layers.

2.5.2 Collection side wafer thickness

The thickness of the wafer placed on the collection side h_{wc} has, in geometrical raytrace simulations, no influence on the numerical aperture of collection microlens and hence on the amount of the collected fluorescence light. However, having a thick wafer increases the diameter of the collection microlens and hence limits the distance between two consecutive microchannels. Moreover, having a large collection microlens increases the sensitivity to cross talk. It was therefore decided to use a rather thin wafer (500 μm) wafer on the collection side.

2.5.3 Microchannel orientation and fabrication tolerances

For all detection geometries considered, the orientation of the microchannel had little influence on the excitation beam and can be easily compensated by a slight modification of the excitation microlens height (focal length). This is due to the small difference of the refractive indices between the glass of the wafers ($n_g = 1.47$) and the water in the microchannel ($n = 1.33$). The reservoirs, and therefore the access holes, must be placed on the top side of the chip. We chose to etch the microfluidic network and to drill the access holes onto separate wafers. This approach has the advantage, that the wafers can be processed in parallel (saving of time) and independently, which reduces the fabrication risks. For convenience, the detection set-up (photodetector/microscope) will be installed above the chip. Therefore, the microfluidic network is etched into the excitation side (bottom) wafer and the access holes are drilled into the cover wafer.

The influence of the alignment and the dimensional tolerances of the elements comprising the chemical chip were evaluated for the two variants of the stop detection systems and for the off-axis detection system. Simulations were carried out to find the smallest collection microlens radius as a function of the excitation microlens parameters (xy-position, height), the thickness of the excitation and collection side wafers, and the incident angle of the excitation beam. The microfabrication technologies used for the microchemical chip fabrication and for the microlens deposition (Chap. 3) makes it possible to have a microlens position deviation of less than $\pm 6\ \mu m$. The microlens height (i.e. the focal length) can be controlled to within $\pm 2\,\%$. The tolerance on the wafer thickness is, for standard wafers, $\pm 10\,\%$ of the nominal thickness. Finally, a $\pm 1^\circ$ variation on the incident angle was also taken into consideration.

For the first variant of the stop system (stop deposited on the excitation side), the worst tolerance combination reduces the maximum collection microlens radius r_c or collection aperture radius r_{pc} to 73 μm ($NA_c = 0.21$), instead of 125 μm ($NA_c = 0.29$) in the ideal case. The fluorescence power collected is hence divided by two. For the second variant (stop on the collection side), the influence of fabrication and alignment tolerances is very significant. In the worst case, to ensure that no excitation rays are focused onto the detector, the stop must be $400\ \mu m \times 100\ \mu m$ instead of $120\ \mu m \times 12\ \mu m$ in the ideal case. Though $\sim 20\,\%$ of the collection fluorescence light is blocked by the stop in the worst case, the NA_c is still larger (0.64 instead of 0.21) when the stop is deposited on the collection side. Hence, the amount of fluorescence light collected is greater than in the first variant (stop on the excitation side). The off-axis system is less sensitive to position and dimension variations than the stop systems. Thus, in the ideal case, the collection microlens radius is $r_c = 140\ \mu m$ ($NA_c = 0.4$) but when the fabrication tolerances are taken into account this value reduces to $r_c = 130\ \mu m$ ($NA_c = 0.37$).

Of the three systems discussed, the stop detection system with the stop on the collection side is the system with the highest NA_c, and hence the design capable of collecting the most fluorescence power. However, this system is very sensitive to position and dimension tolerances. Moreover, because of multiple reflections, part of the excitation beam blocked on the stop is likely to be collected (especially if a non-absorbing layer, such as chromium, is used for stop/aperture realization). A fortiori, even if the off-axis detection system presents a lower NA_c, it presents several advantages. The maximum collection microlens radius is given for a circular aperture. As discussed previously, r_c (or r_{cp}) is limited by the position of the excitation rays on the collection side of the chip. Since the outgoing spot is located just at the bottom of the aperture, it is possible to block the bottom section of the aperture with a square stop (left raytrace diagram of Fig. 2.15). Deposition of a collection microlens with a larger radius r'_c, limited only by microfabrication technology is then possible. In that case, the off-axis system competes favorably with the stop system with the stop on the collection side, because the surface area of the collection microlens which is blocked by the stop is smaller for the off-axis system. This means that more fluorescence light can be collected in the off-axis case than in the central stop case. Moreover, the astigmatism effect can be compensated by the deposition of elliptical microlenses. Due to the incident angle of the excitation beam on the aperture layer, this beam is directed downwards, away from the collection microlens (Fig. 2.3). The remaining excitation beam and its multiple reflections inside the microchemical chip are less critical than the stop system. Finally, the fact that the off-axis system is less sensitive to fabrication tolerances is a gage of robustness for the detection system. This is the reason why the off-axis system was chosen for implementation on microchemical chips.

Since the scattering of the excitation beam at the various interfaces (excitation microlens surface, chip surface and microchannel interfaces) is an important source of background light, the detection system must also be conceived so as to limit the scattered light collection. A solution to prevent the collection of the excitation light scattered on the excitation side is to insert an intermediate aperture layer at the level of the microchannel (between the two glass wafers).

2.6 Off-axis collection system

Figure 2.18 shows the collection system associated with the off-axis excitation system of Fig. 2.15. The microlens deposited on the collection side images the probe volume onto a pinhole placed between the chip and the photodetector, just in front of the interference filter. The function of this pinhole is to block the rays which do not originate from the

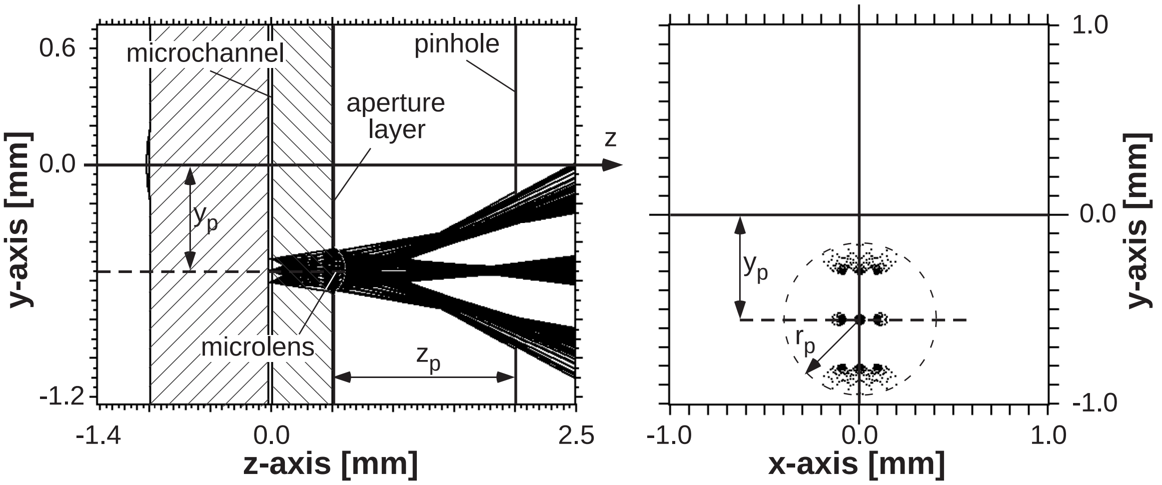

Figure 2.18: Collection system used with the excitation system shown in Fig. 2.15. The right graphic shows the ray distribution in a plane situated 1500 μm away from the surface of the chip (pinhole position). The microlens focal length is 320 μm.

probe volume and hence to reduce the background signal. The probe volume is defined along the x-axis by the microchannel rim, and along the y-axis by the area covered by the excitation spot, whose position shifts as a function of system tolerances and excitation beam incident angle variation. The probe volume dimensions are 60 μm and 120 μm along the x-axis and the y-axis, respectively. To get the highest sensitivity as possible, all the rays transmitted through the pinhole must reach the photosensitive area of the photodetector when the fabrication tolerances are taken into consideration. The pinhole position Z_p is determined by the pinhole mount thickness and the filter/pinhole holder space in front of the photodetector which gives a distance Z_p of about 1500 μm. As a consequence of the imaging condition, the focal length of collection microlens becomes 320 μm which is realized with a hight of $h_c = 49$ μm and a radius of $r_c = 130$ μm ($r_c/h_c \simeq 2.6$), and the imaging magnification is 1:3. The microlens radius was chosen equal to the maximum aperture radius found in the raytrace simulation of Fig. 2.15 (for a circular aperture array). Since the the magnification is 1:3, the size of the image of the probe volume at the pinhole position is 180 $\mu m \times 360$ μm.

Figure 2.18 shows the raytrace diagram of the collection system with a pinhole having a radius $r_p = 400$ μm. The simulation is carried out assuming nine light sources equally spread out over the 60 $\mu m \times 120$ μm probe volume. In this configuration, all but the most extreme rays issued from the probe volume and collected by the microlens reach the photodetector. The size of the spot at the photodetector window is 1.3 $mm \times 2.1$ mm, whereas the photodetector window is 2.0 $mm \times 13.0$ mm. Therefore, all the light collected from the probe volume reaches the active area of the photodetector.

Chapter 3

Fabrication of the microchemical / microoptical device

3.1 Introduction

As discussed in Chap. 1, we take advantage of the microfabrication technology to realize the microfluidic chip and to directly implement the detection system onto the chemical chip. The chip is made up of a 0.5 mm thick cover wafer and a 1 mm thick wafer in which the microfluidic networks are patterned. Both wafers are 100 mm in diameter. Two patterned chromium layers and refractive microlenses deposited directly on both sides of the chemical chip form an off-axis detection system, as described in Sec. 2.4. Figure 3.1 shows a 3D drawing of the central part of the microchemical chip where the illumination and collection elements of the detection system are deposited.

3.2 Microchemical chip fabrication

3.2.1 Microfluidic channel etching

As control of the light transport inside microchips is a major issue to obtain high detection sensitivity, particular attention must be paid to avoid excitation beam scattering sources and therefore to microchannel surface roughness. The main chemical chip fabrication steps are summarized in Fig. 3.2. The etching process begins by cleaning the wafers for 10 min in 100% fuming nitric acid (HNO_3). The wafers are then carefully rinsed with deionized water (DI water) in a cascade bath and dried with pressurized nitrogen. A wet etching mask of a 2000 $\AA$ polysilicon (poly-Si) layer is first deposited on both sides of the 1 mm thick wafer by low pressure chemical vapor deposition (LPCVD). A 1.5 μm thick

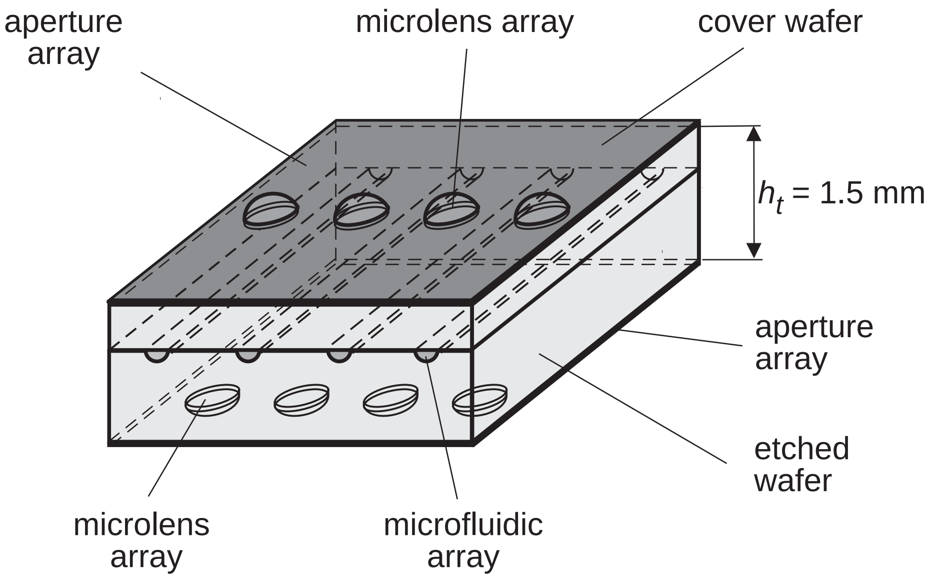

Figure 3.1: Microchip configuration. For the sake of clarity, microlens and microfluidic arrays are exaggerated in size.

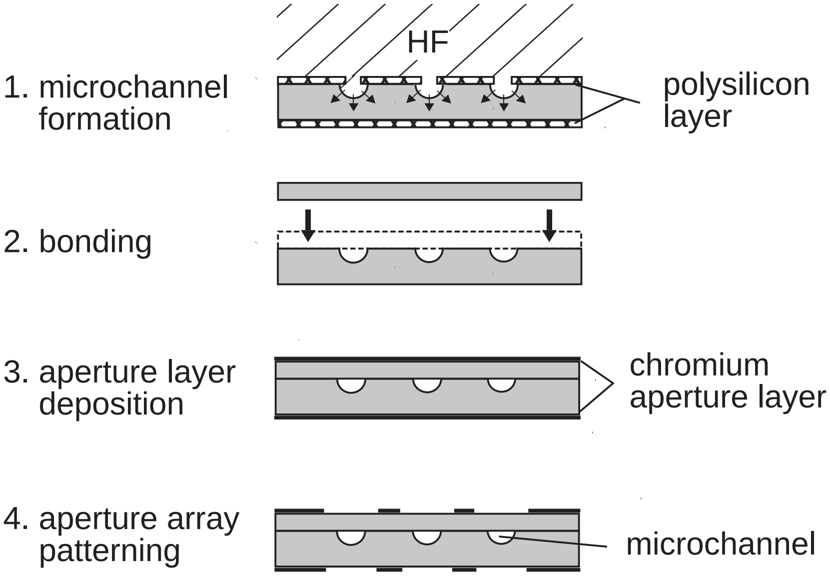

Figure 3.2: Schematic diagram of microchemical chip fabrication and aperture layer deposition (for the case where no intermediate aperture layer is desired).

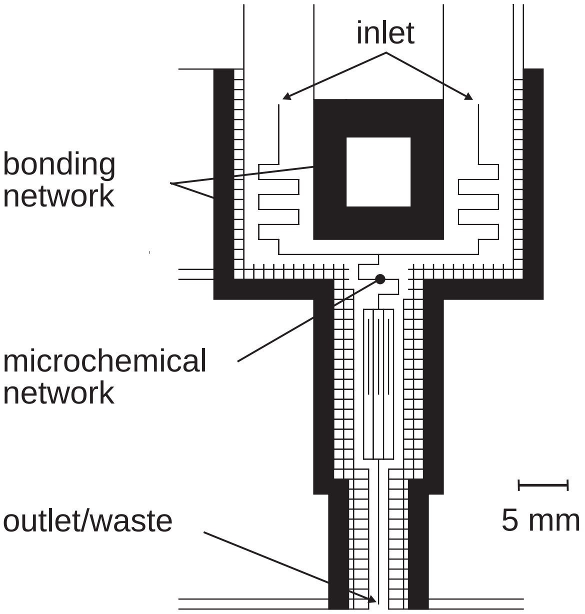

Figure 3.3: Mask pattern for wet etching. Black regions are openings in the chromium layer and thus etched regions. Network lines are 10 μm wide.

AZ1518 (Clariant AG, Muttenz, Switzerland) photoresist layer is then spin-coated on one side of the wafer. After prebaking ($85°C$, 35 min), the photoresist is exposed through a chromium mask (Fig. 3.3) with the help of an AL6-2 mask aligner (Karl Süss KG, München, Germany). After development in an AZ351B solution (Clariant AG, Muttenz, Switzerland), the wafer is rinsed with DI water and dried with pressurized nitrogen. The patterned photoresist layer is then hardened in a postbake step ($120°C$, 30 min), and the unprotected poly-Si layer removed by reactive ion etching (RIE). The photoresist is stripped with MOS quality acetone. The wafer is then rinsed with MOS quality isopropanol and dried with pressurized nitrogen. In order to get rid of all the photoresist traces and RIE etching residues, the procedure is completed by a 10 min oxygen plasma cleaning ($100 \cdot 10^{-3}$ torr, 100°C). The microfluidic networks are then isotropically etched in $20\% HF$ at cleanroom temperature (21°C). The etching time is ~ 22 min (etching rate of ~ 1.1 $\mu m/min$). The etching process is followed by a thorough rinse with DI water. The poly-Si mask is then removed in a 40% KOH bath at $60°C$ (2 min), followed by a rinse in DI water.

The 0.5 mm thick cover wafers have 1 mm ultrasonically drilled holes to enable access to the microfluidic networks. If an intermediate aperture layer is needed, a low pressure chemical vapor deposition (LPCVD) of a 1000 $\AA$ aluminum layer is performed on one side of the cover wafers. The aluminum layer is patterned using the same photolithographic techniques as those used to pattern the poly-Si layer, except that the aluminum layer is etched in an AZ400K (Clariant AG, Muttenz, Switzerland) solution for 5 min.

Any Al deposited in the access holes is removed during this step. A 1000 $\AA$ plasma-enhanced-chemical-vapor-deposited (PECVD) silicon nitride (Si_3N_4) layer then covers the aluminum layer. This non-conducting layer not only enables wafer bonding but also isolates electrically the microfluidic channels, which is necessary for electroosmotic pumping and capillary electrophoresis separation (requiring high potentials between the inlets). Si_3N_4 has further been chosen for its transparency at the fluorescence wavelength of interest ($\sim 670\ nm$). To test the fabrication of systems with intermediate aperture arrays and avoid the cost of a standard chromium mask, the aperture pattern was printed on a transparent polyester film (Alliance Recording HN, Agfa-Gevaert, Belgium) with a resolution of 3600 dpi. This film was then taped onto an old $5inch$ standard mask from which the chromium layer had been removed. Two microfluidic structures were laid out on each wafer. Both the microfluidic wafer and cover wafer were made of Borofloat 33 glass (Schott, Germany), which is equivalent to Corning 7740 (Pyrex). Wafer surfaces were delivered with a "3 diamond" polished finish, which means that the arithmetic average deviation Ra of the absolute values of the roughness profile from the mean line is better than or equal to 20 $\AA$ and the root-mean-square roughness R_{rms} is $< 50\ \AA$.

Small 1 cm x 1 cm wafer pieces were used to evaluate the etched surface roughness. These samples were etched to a depth of $\sim 25\ \mu m$ in 20% HF and the surface roughness was measured on an Alpha Step 500 profilometer (Tencor Instruments, Mountain View, Ca) equipped with a 12.5 μm stylus. The Ra of Pyrex glass samples after wet etching was better than 21 $\AA$ (Ra $< 13\ \AA$ before etching). Though the surface roughness increased, it remained close to the "three diamond" limit (Ra $< 20\ \AA$). Half-spherical cavities with a radius ranging from a few μm to a few tens of μm were also visible after etching. It is likely that micro-bubbles, occlusions or local chemical modifications [58] were at the root of these cavities. These were few in number, though, and did not pose any problems in the etching of the microfluidic networks. These etching tests also showed that the etching rate is strongly dependent on acid temperature [58] and the number of wafers already etched. This is why the etching process was performed in two steps. Wafers were first etched for 20 min and, after rinsing and drying, the microchannel depths were determined using a profilometer. Measurements were taken in six places spread equally over the wafer. The etching rate is given by the average depth divided by the etching time. Wafers were then etched a second time. The etching duration was given by the microchannel depth desired (25 μm) minus the average depth, all divided by the etching rate determined previously. Table 3.1 shows the etching rate of four batches (total of 8 wafers) made in the same acid bath. The etching rate decreased linearly from 1.2 $\mu m/min$ (first batch i.e. freshest acid bath) to 0.9 $\mu m/min$ (fourth batch). The relative difference between the microfluidic average depths and the nominal desired depth h_m of 25 μm is better or equal to 4%. This means that it is possible to accurately predict the time required to obtain a particular etch depth. The standard deviation of microfluidic depths within the same batch is better than 0.6 μm.

Table 3.1: Etching rate and microfluidic depths.

`batch number` `(2 wafers/batch)`	`etching rate`	`average microfluidic` `depths` (±0.6 μm)
1	1.2 $\mu m/min$	24.0 μm
2	1.1 $\mu m/min$	24.4 μm
3	1.0 $\mu m/min$	24.8 μm
4	0.9 $\mu m/min$	24.7 μm

3.2.2 Glass substrate bonding

Microfluidics and cover wafers are bonded together using two different methods. Systems with an intermediate Al aperture layer were anodically bonded [59, 60], while the systems without such a layer were thermally bonded [61, 62]. To get as few unbonded regions as possible, the surfaces must be perfectly clean and free of dust particles. Wafer cleaning was therefore carried out in a class 100 atmosphere. To reduce the surface to be bonded and thereby reduce bonding imperfections, a second microchannel grid is patterned around the chemical microfluidic network (Fig. 3.3). This network is etched at the same time as the chemical microfluidic channels and is directly connected with the outside atmosphere. This enables the escape of trapped air and gases from hot wafers during the bonding process [62]. Figure 3.4a shows the thermal bonding set-up. The cover wafer is first placed manually (using tweezers) on the etched wafer, so that the access holes align with the ends of the channels. The stacked system is then placed between two 2 mm thick ceramic plates and transported outside the cleanroom to a furnace (Heraeus Instruments M110, Hanau, Germany). To ensure good contact between the wafers, a metal cylinder ($\sim 1\ kg$) is placed on top of the stack. Some chips were bonded with two 0.5 mm thick non-woven alumina/silica fabrics (Goodfellow Cambridge Ltd, Cambridge, England) placed between the wafers and the ceramic plates (Fig. 3.4a). This soft layer ensures better pressure distribution. The bonding temperature profile is given in Fig. 3.5. This bonding cycle is repeated once or twice with weights of $\sim 150\ g$ placed over unbonded or poorly bonded regions, as evidenced by whitish or slightly opaque regions or interference fringes

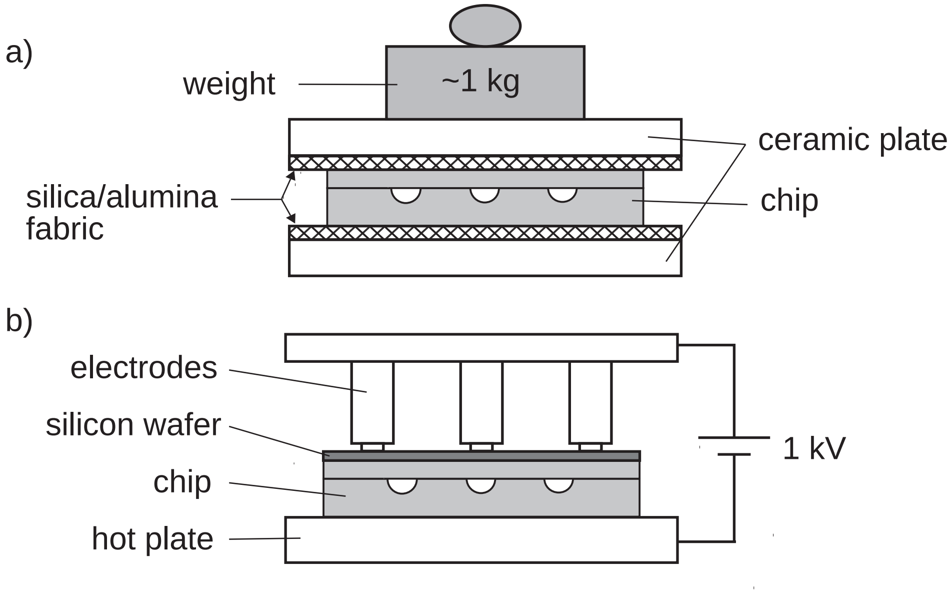

Figure 3.4: Set-ups for a) thermal bonding, and b) anodic bonding.

(so-called Newton rings). Figure 3.4b presents the anodic bonding set-up. The glass wafers are aligned under the microscope (with the help of alignment marks) and then placed on the hot plate of the bonding set-up. A single-sided polished silicon wafer is placed on top of the chip. This conductive wafer enables a homogeneous electric field distribution. The rough side of the silicon wafer is placed in contact with the glass surface to prevent the silicon wafer and glass wafer from bonding. The electrodes (three metallic feet fixed on an aluminum plate and weighing $\sim 150\ g$) are then lowered onto the stacked wafers. The system is heated up from ambient cleanroom temperature to $450°C$ in 15 min. The voltage between the hot plate and the electrodes is then increased (with a current limitation of 4 mA) from 0 kV to $0.7 - 0.8\ kV$. The temperature and potential are kept constant during $\sim$ 15 min as the current slowly decreases to $\sim$ 2.6 mA. The potential and the hot plate are then switched off. The system is left on the hot plate and cooled down from $450°C$ to room temperature.

The open lines in the masking layer (same width as the chromium mask lines) are 10 μm wide. This means that the microchannel section consists of a half circle with a flat bottom as shown in Fig. 3.6. The width of the flat bottom is given by the mask opening, and the microchannel depth by the etching time.

In comparison with a previous chip design not having microchannel networks for bonding [63], the average bonding cycle number necessary to get sealed microfluidic networks was reduced from three to two on average. This number decreased further to just one for the chips bonded with the alumina/silica fabric. Chips bonded in this way were perfectly sealed without any unbonded regions and, as shown in Fig. 3.6, there is no visible inter-

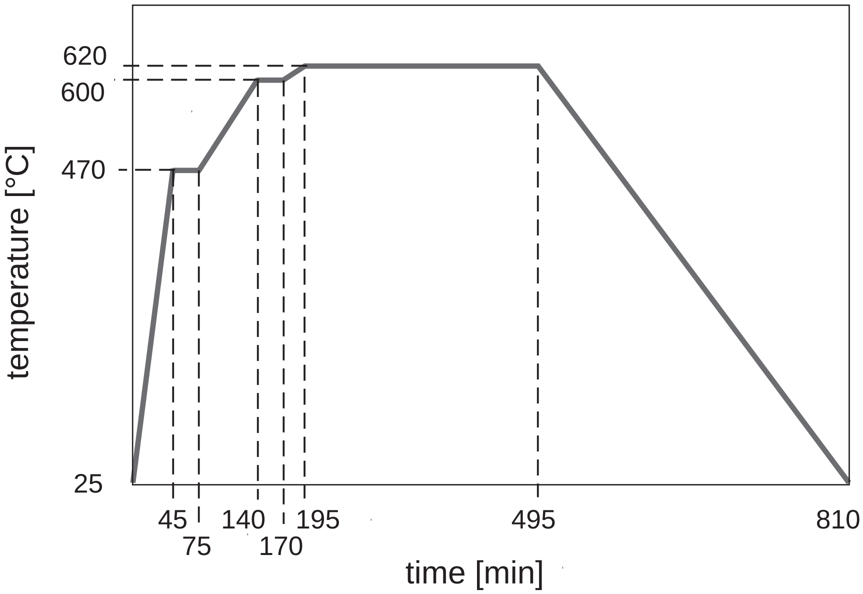

Figure 3.5: Thermal bonding temperature profile.

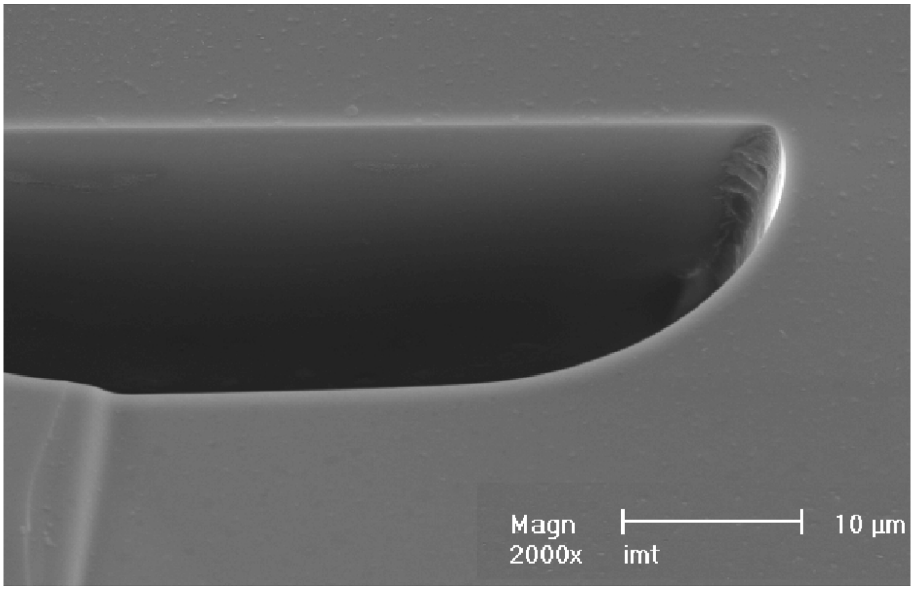

Figure 3.6: SEM picture of a cross-sectional view of a microchannel.

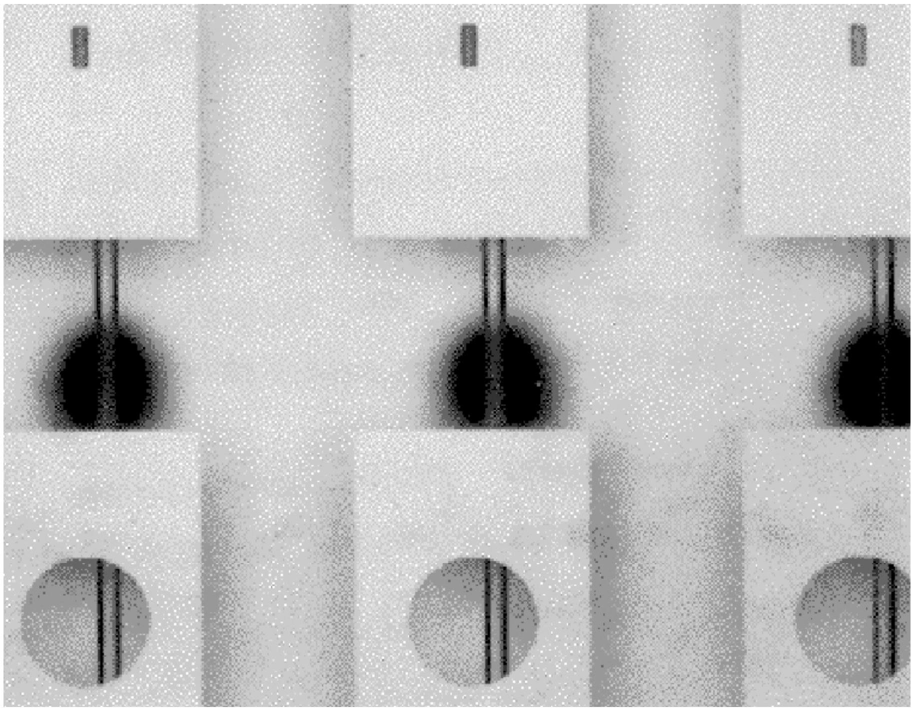

Figure 3.7: Intermediate aperture layer deposited along parallel microfluidic channels. Slightly unfocused, one can see the aperture layer deposited on the bottom surface (excitation side) of the chip (dark circles).

face between the wafers. As no further cycles were necessary, the chip surfaces were not permanently and strongly marked by the weight deposited on unbonded spots. This is an important point, as a flat glass surface is necessary to control the microlens photoresist deposition (i.e. control the microlens focal length) and to avoid scattering at the interfaces. The non-woven fabric slightly marked the chip surfaces, however. To prevent the alumina/silica fibers from marking the softened glass, thin, smooth aluminum sheets can be inserted between the fabric and the glass. Anodic bonding also required one cycle to seal microfluidic networks. This process is faster (cycle of $\sim 45\ min$) than the thermal bonding process (cycle of $13\ h\ 30\ min$) and enables the bonding of two glass wafers with an intermediate aperture layer if needed (Fig. 3.7). On the other hand, the process requires a Si_3N_4 layer deposition. Two kinds of intermediate apertures were integrated: 1) a rectangular aperture with the same width as the microchannels and 2) a circular aperture larger than the microchannel width. The circular apertures are less efficient (they do not block all the light which is not focused into the microchannel) but they are more tolerant to misalignment. The anodic bonding set-up used was very simple and did not allow the monitoring or modification of wafer alignment when the electrodes were lowered. As the feet did not touch the silicon wafer exactly at the same time, it often caused a slight displacement of the stacked wafers. This is why the apertures are not perfectly aligned with the microfluidics, and why the rectangular apertures (at the top of Fig. 3.7) would prevent the fluorescence light from being collected. The printed film used as the photolithographic mask worked well. A precise alignment was difficult to achieve, though, as the taped film sometimes rubbed against the photoresist. Moreover, when the wafer was placed within proximity of the mask for exposition, the film tended to move slightly. This technique is cheap and useful for systems with simple and low resolution structures, but is not suitable when precise alignment ($< \pm 20\ \mu m$) for a multimask process is required.

3.3 Microoptical system

3.3.1 Aperture array deposition

Before the formation of integrated aperture and microlens array layers, the inlets of the bonded microfluidic chip are sealed up with small 5 mm squares of polyimide-silicone adhesive tape (3M, Austin, USA). This prevents contamination of the microchannels by solvent and photoresist developer, or clogging with photoresist. As shown in point 3 of Fig. 3.2, the microoptical element fabrication begins with an LPCVD deposition of a 2000 $\AA$ chromium layer on each side of the chemical chip. These layers are successively patterned by means of the same techniques as described in Sec. 3.2.1 (poly-Si patterning), except that the KOH etchant is replaced by a chromium-etching solution (100 g of $Ce(SO_4)_2 \cdot 4H_2O$, 135 g of $(NH_4)_2Ce(NO_3)_6$ and 50 mL of H_2SO_4 in 1000 mL of H_2O). The etching time is $\sim 15\ min$ at room temperature ($\sim 21°C$). Special alignment marks on the photolithographic mask allow precise positioning of the aperture arrays with respect to the microchannels ($< 5\ \mu m$). Alignment marks are also etched into the chromium layer at the same time. These alignment marks later allow precise alignment of the microlens arrays with respect to the aperture arrays, and hence also with the sealed microchannels.

Figure 3.8 shows the base of a cut photoresist microlens deposited on an aperture formed in the chromium layer. The difference between the glass surface situated under the microlens and the chromium layer is clearly visible. Since the microlenses are deposited within $\pm 2\ \mu m$ with respect to the aperture array, the aperture radius is chosen 5 μm smaller than the microlens radius to ensure that all the light going outside the collection microlens is blocked, even in case of misalignment. Moreover, since the microlens profile is very steep at the rim, the rays focused in the outer ring of the microlens suffers from aberrations and increases the false light. This is why the apertures radius (on the collection side and on the excitation side) are taken not only 2 μm smaller than the microlens radius (as required by the microlens deposition tolerance) but 5 μm smaller (Fig. 2.18).

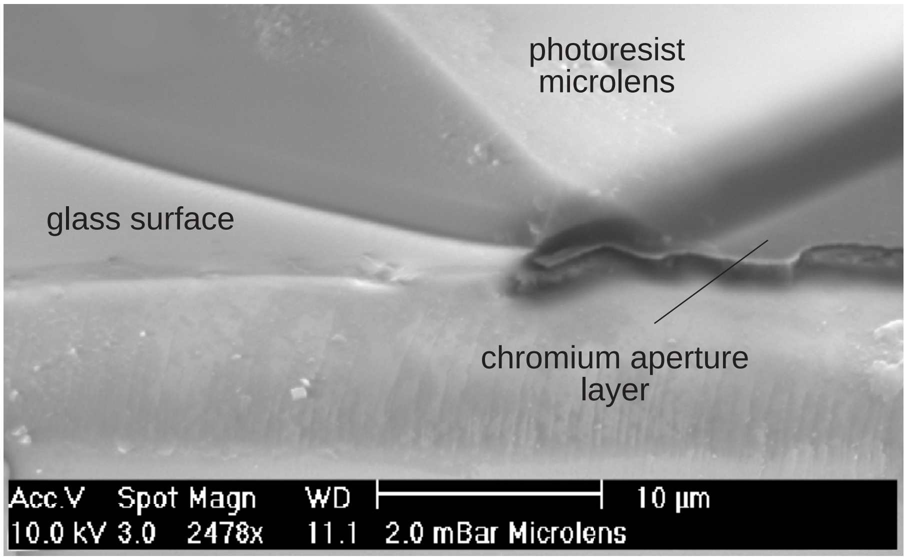

Figure 3.8: SEM picture of a cut microlens deposited on an chromium aperture layer (see Fig. 2.18).

3.3.2 Microlens array deposition

To get low background light, the focusing of the excitation beam is more important than the collection of the fluorescence light. Hence, excitation microlens quality is more important than the collection microlens quality. Therefore, to reduce the risk of scratching the surfaces and thus creating a source of scattering, the microlenses used to focus the excitation light are deposited after the microlenses used to collect the fluorescence light. Figure 3.9 shows the microlens array fabrication steps. A 30 μm thick layer of AZ4562 photoresist (Clariant AG, Muttenz, Switzerland) is deposited on the side of the chip with drilled holes. The thick photoresist deposition is performed by a RC8THT spin-coater coupled with an ACS hot plate (Karl Süss, Garching / Munich, Germany). After the photoresist deposition, the wafers are directly and automatically transported to the hot plate for 4 min of soft-baking at 110°C. A MA8-BA6 mask aligner (Karl Süss, Garching / Munich, Germany) is then used to expose and pattern the photoresist. An AZ400K (Clariant AG, Muttenz, Switzerland) is used as developer. The rinsed and dried wafers are finally placed (photoresist structures up) 0.5 mm above the ACS hot plate (150°C, 2 min). The heated photoresist cylinders melt, and under the influence of surface tension, microlenses are formed. The excitation microlenses are deposited in the same way on the other side. The only difference lies in the photoresist thickness which is 16.5 μm (a thinner photoresist layer leads to a thinner microlens and hence to a longer focal length). A 70 μm PVC adhesive film is used to protect the first deposited microlens array during the second deposition. The film is removed just before the melting procedure. As will

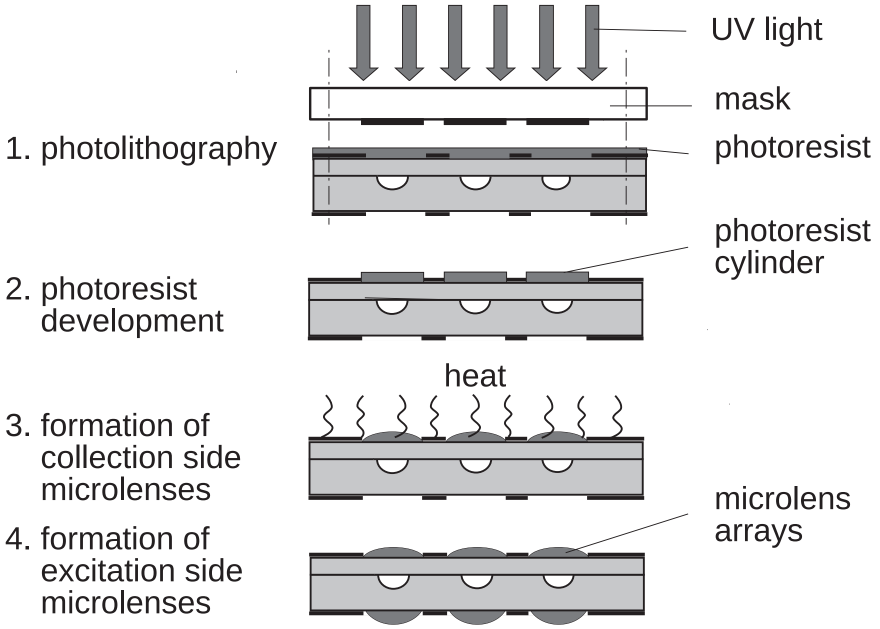

Figure 3.9: Refractive microlens deposition. The focal length of the excitation and the collection microlenses are $\sim 1.4\ mm$ and $\sim 2.0\ mm$, respectively.

be shown in Sec. 3.3.3, the processing of the microchemical chip with microlenses on the excitation side and the removing of the protecting adhesive film do not debase the microlenses quality.

A wide choice of microlens shapes (spherical, elliptical, cylindrical, etc.) and sizes can be obtained with this melting fabrication technique [54]. However, use of this technique does impose some limitations on microlens dimensions. The microlens height h_L is limited by the photoresist layer thickness which can be spun on the substrate. Since the maximum thickness is $\sim 80\ \mu m$, the maximum microlens height is smaller than $120\ \mu m$ (when the photoresist cylinder melts, the surface tension forms a lens which is ~ 1.5 times higher than the cylinder height). The achievable microlens radius to height ratio r_L/h_L of the microlens is between 2 and 7. A microlens with $r_L/h_L \leq 2$ is very high, and has a small radius of curvature. Such lenses are characterized by a small radius of curvature and with spherical aberrations which are significant even for a non-imaging system. When the $r_L/h_L \geq 7$, the photoresist layer thickness is too small and the microlens profile obtained after melting is flat or even concave at the center of the microlens. The microlens is thus not usable for light focusing or collimation. The best microlens shape is obtained when r_L/h_L is close to 5.

Figure 3.10 shows the section of a photoresist microlens. In this system, two kinds of refractive microlenses were deposited to focus the excitation beam into the microchannel: a circular microlens of $175\ \mu m$ radius and $25\ \mu m$ hight, and an elliptical microlens of $350\ \mu m \times 400\ \mu m$ size and $27\ \mu m$ hight. The elliptical microlenses allows the reduce

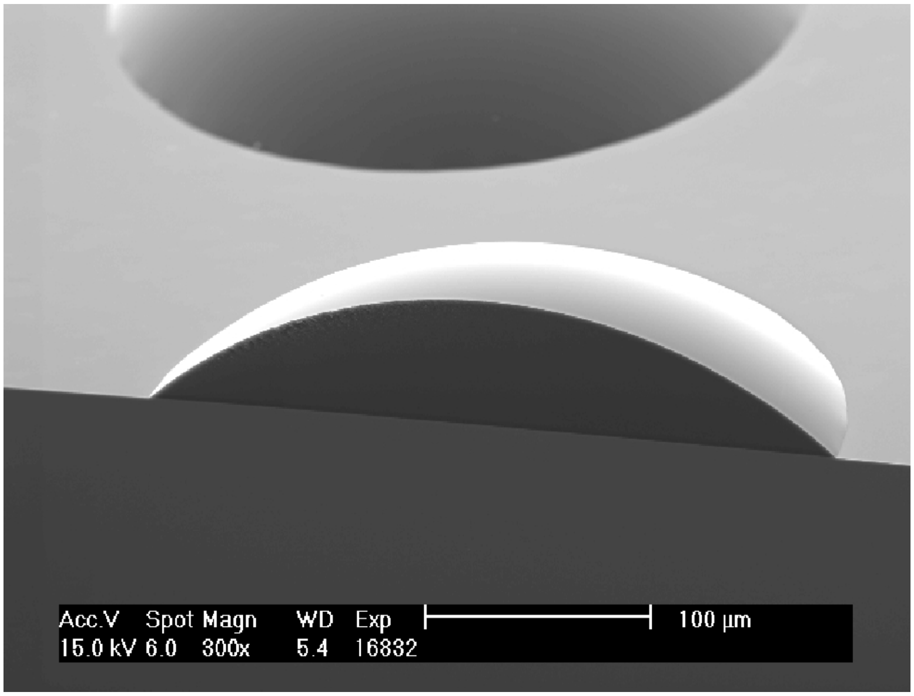

Figure 3.10: Section of a 310 μm diameter photoresist microlens.

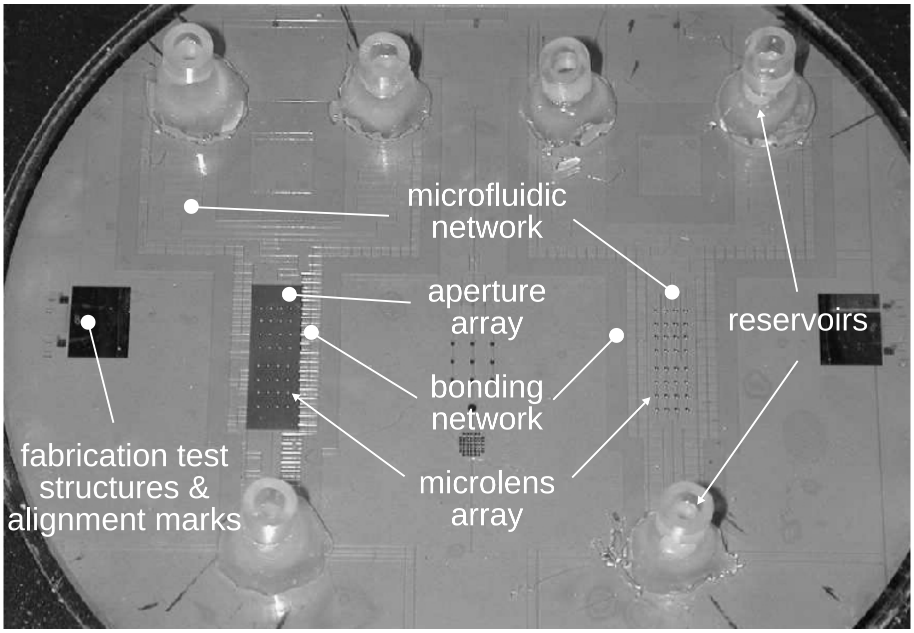

Figure 3.11: View of the complete chip with two microchemical systems. The left microchemical system possesses all the optical element layers, whereas the right one has no aperture layer on the collection side. The glued reservoirs where the sample/buffer solution is introduced are also visible.

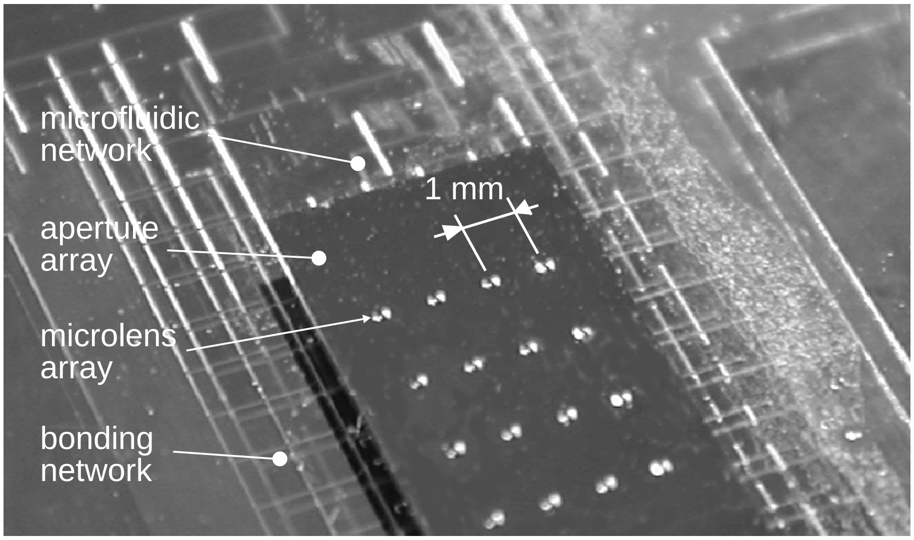

Figure 3.12: View of the collection side of the microchemical system. An array of microlenses (130 μm in radius and 49 μm high) have been deposited on the collection side aperture array. Unlike the excitation side aperture array, which is deposited over the entire wafer surface, the collection side aperture array is 5 $mm \times 16$ mm large. This allows the flow inside the microchannels to be visualized. The microfluidic and bonding network, as well as their reflection on the excitation side aperture array, are also visible.

the optical aberrations for off-axis excitation, and therefore yields a smaller spot size. A better-focused excitation beam leads to a higher excitation intensity and facilitates more efficient fluorescent light collection. Figure 3.11 shows a view of the complete system as seen from the collection side and Fig. 3.12 shows a closer view of the aperture/microlens arrays. Several collection microlenses are deposited along each sealed microchannel.

3.3.3 Photoresist microlens quality

Microlens quality was tested with the help of a Twymann-Green interferometer [64, 65]. Figure 3.13 shows the standard deviation σ_w of an excitation and collection side microlens surface profile from an ideal sphere [66, 67]. In both cases, $\sigma_w = 0.11\,\lambda$, which corresponds to a Strehl ratio of ~ 0.76. Since the interference fringe contrast at the microlens rim is not sufficient to make measurements over the whole microlens surface, the excitation and collection side microlens measurements were carried out only for surfaces of radius 160 μm and 120 μm, respectively. Even if the microlenses are not diffraction limited (one consider that an optical system is diffraction limited when the Strehl ratio is ≥ 0.8), the microlens quality is sufficient for non imaging systems. Moreover, the collection side microlenses deposited first were not damaged or affected by the fabrication of the excitation side microlenses. Microlenses of equal quality can hence be directly deposited on both sides of the same substrate in two subsequent fabrication steps.

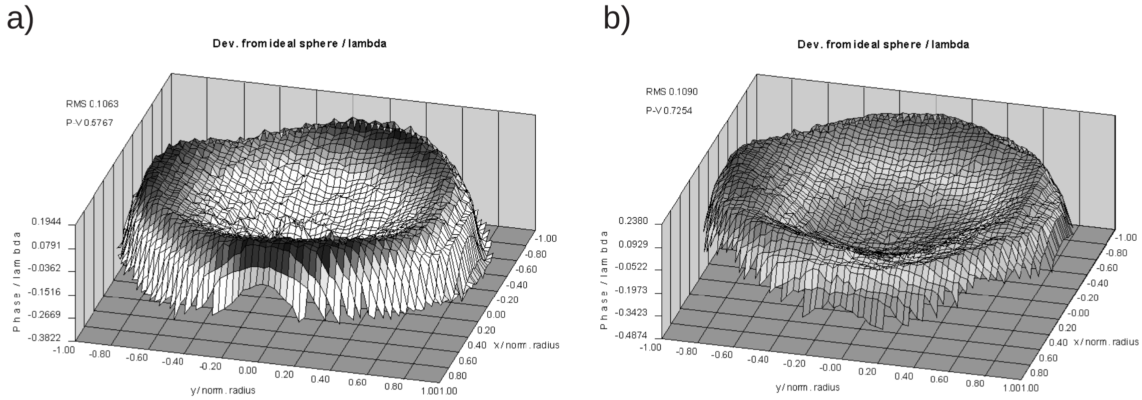

Figure 3.13: Aberrations of the a) excitation side microlens b) and collection side microlens, measured with a Twyman-Green interferometer.

Chapter 4

Experimental Results

4.1 Introduction

In this chapter, measurements realized with the microchemical chips described in Chap. 3 are presented. The measurement set-up and procedure are first presented. The position and shape of the excitation beam spot at the microchannel and collection side position is then presented, which allows a comparison with the raytrace simulations of Chap. 2. The influence of the excitation side microlens on the spot in the microchannel as well as the influence of the microchannel roughness on the background level are also addressed. Finally, measurements with Cy5$^{\text{TM}}$ cyanine fluorochrome solution are presented. The excitation spot in microchannels filled with Cy5$^{\text{TM}}$ solution is measured and compared with the spot in DI water. The sensitivity of the integrated detection system is determined and compared to other relevant work. The influence of the excitation power and cross-talk issues are then presented.

4.2 Measurement set-up

4.2.1 Fluidic set-up

As discussed in Sec. 1.6, glass was chosen as the microchemical chip material, since it is transparent in the visible and electrically non-conductive, enabling electroosmotic pumping. As shown in Fig. 4.1, the microfluidic network layout is T-shaped, with the holes allowing for the access to the microchannels placed at the end of each branch of the "T". This layout was designed for basic sample concentration monitoring after the T-junction by controlling the potential applied between the outlet (waste) and the inlets. Thus, if one of the inlet reservoirs is filled with a buffer solution and the other one filled with a dye solution, the sample concentration after the T-junction is proportional to the ratio of electroosmotic flows in each branch and hence to the potentials applied between the outlet and the inlets. The meander geometries placed between the inlets and the T-junction, and between the T-junction and the detection area (separation of the single microchannel in four parallel microchannels, numbered from 1 to 4 from left to right), increase the overall length of the microchannels from one inlet to the outlet. Channel resistance is also increases with length which, for a given potential between one inlet and the outlet, reduces the current. The power that must be dissipated in the microchannels in the form of heat is also reduced. The length from the inlet to the T-intersection is 45 mm, the total length from one of the inlets to the outlet is 89 mm and 91 mm for the inner and the outer detection area microchannels (microchannels number 2, 3 and 1, 4 respectively). As discussed in Chap. 3, the microchannels are $\sim 25\ \mu m$ deep and $\sim 60\ \mu m$ wide.

Figure 4.2 shows the two types of reservoirs used during this work. The first type (shown in Fig. 4.2a) is made from sections of polyvinyl chloride (PVC) tubing glued onto the microchemical chip around the access holes, by means of a two component epoxy glue. Since the tube section was not always perfectly flat and in contact with the chip surface, it was thought that some solution might leak into the interstice, which would render complete rinsing of the reservoirs difficult. This is why a more advanced type of connector was designed (Fig. 4.2b). This one was formed by gluing a stainless steel nut onto the chip and screwing a PE reservoir into it. Since it could be removed and even replaced by another type of reservoir if needed, the reservoir and the chip surface around

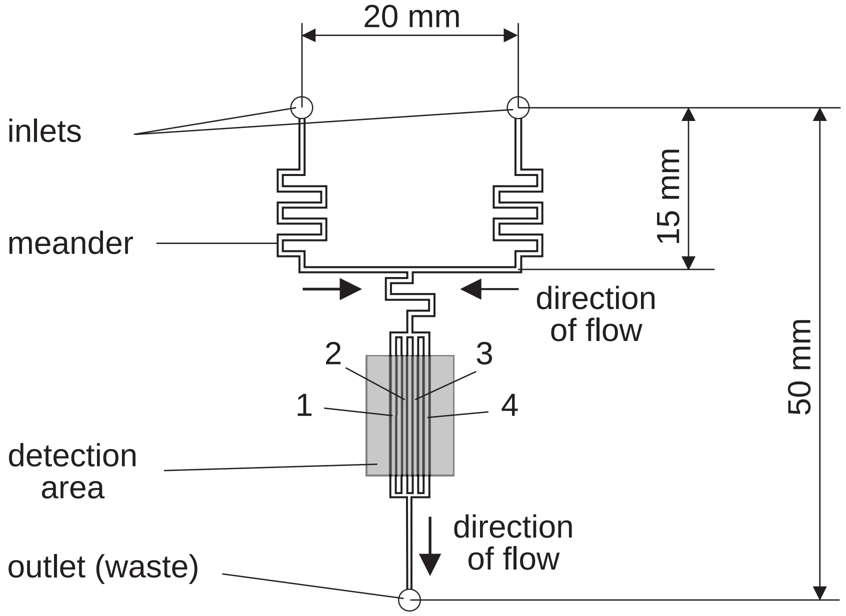

Figure 4.1: Microchannel layout of the chemical chip.

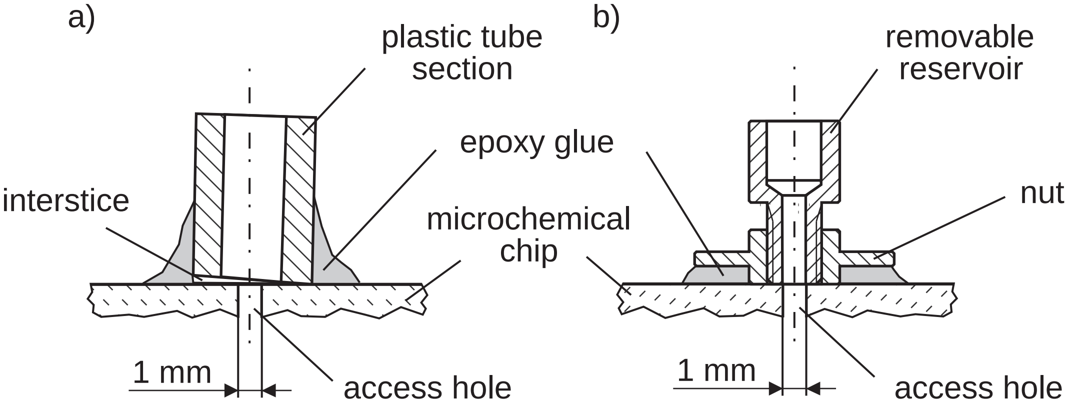

Figure 4.2: Microfluidic channel connectors composed of a) a PVC tube section directly glued onto the chip and b) a stainless steel nut glued onto the chip and a removable polyethylene (PE) reservoir.

the inlet/outlet could be perfectly rinsed.

Though the chip was designed for electroosmotic flow, it was decided to use vacuum as a simpler means to draw solutions through the channels for these experiments. Samples and cleaning solutions were simply introduced into the inlet reservoirs and pumped through the microfluidic channels to the outlet by means of a membrane pump connected to the outlet. The vacuum at the outlet was $\sim 320\ mbar$ and the flow rate, established by measuring the DI water volume pumped through the system for more than two hours, was $42 \pm 3\ nL/s$. The measurements with the microchemical chips were all performed on the same set-up and according to the same microchemical chip preparation protocol. One hour before the beginning of each series of measurements, the $HeNe$ laser used as excitation source was switched on in order to have a stabilized excitation power. At the same time, the chemical system was thoroughly cleaned and conditioned for use. All solutions were filled into the reservoirs (Fig. 4.2), using syringes equipped with $0.2\ \mu m$ Millex-FG filter (Millipore SA, Bedford (MA), USA). First, the reservoirs were rinsed three times with deionized water (DI water). DI water was then drawn through the microchannels for $20\ min$. Then, the DI water in the reservoirs was replaced in the reservoirs by a $0.1\ M$ solution of $NaOH$. The $NaOH$ solution was drawn for $10\ min$ through the microchannels. The $NaOH$ solution was in turn replaced by DI water, which was pumped through the microchannels for $20\ min$. The microchemical chip was then ready to be used for the measurements. The dye chosen here is a Cy5™ cyanine fluorochrome (Amersham Life Science Ltd., Bucks, England) and all the samples used for fluorescence measurements were prepared from stock solution consisting of $50\ \mu M$ Cy5™ in a $50\ mM$ phosphate buffer at pH 7.4. The $50\ \mu M$ solution was obtained by dissolving $0.4\ mg$ of Cy5-OSu monofunctional reactive dye in $10\ mL$ of a pH 7.4 phosphate buffer solution. The buffer

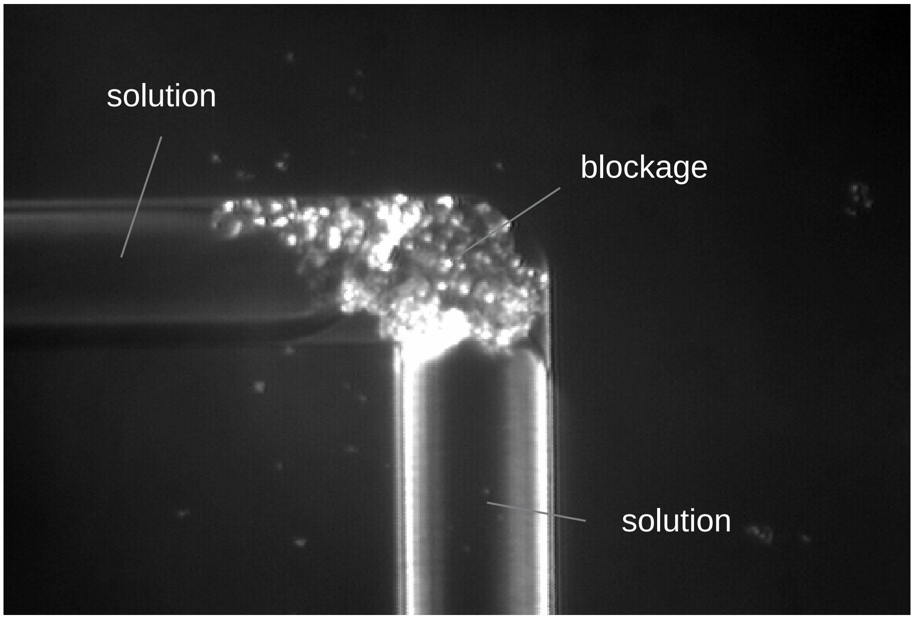

Figure 4.3: Blocked microchannel.

itself was prepared by mixing 19 mL of 100 mM NaH_2PO_4 with 81 mL of 100 mM Na_2HPO_4. The stock solution was kept in the dark at $\sim 6°C$. Samples at lower concentration were prepared by dilution of the stock solution with phosphate buffer. Samples were always allowed to warm up to ambient temperature before utilization.

Observation of the solution flow in the four parallel detection microchannels with a microscope showed that the flow tended to establish itself mainly in the two inner microchannels. Since the path length is shorter for the inner microchannels, and hence the flow resistance slightly lower, the solution flowed preferentially into these inner microchannels. Sometimes though, the flow switched from one inner microchannel to an outer microchannel. This was often due to dust particles perturbing the solution flow or even clogging a microchannel, as shown in Fig. 4.3. Even though, all precautions were taken during the fabrication and utilization of the chips to avoid microchannel contamination or clogging by dust particles, microchannels did clog. The solution to unequal microchannel length would be to connect the inlet microchannel to the detection area to microchannel number 1 and to connect the outlet microchannel to the end of microchannel number 4 (Fig. 4.1). To prevent dust particles from clogging the microchannels, integrated filters could be microfabricated at the inlet at the same time as the microfluidic network [68, 69]. However, this approach was not tried here, as it would have increased the complexity of the structure.

4.2.2 Optical and acquisition set-up

The experimental set-up was composed of two parts, the excitation set-up and the chip holder/collection set-up. The excitation set-up was made up of a 10 mW 1135p $HeNe$ laser (Uniphase Corp., San Jose (CA), USA). The waist radius W_0 of this laser was 0.35 mm. In order to get the largest excitation intensity in the microchannel, the polarization of the laser was turned parallel to the incident plane. To control the excitation intensity, an intensity controller consisting of a half-wave plate followed by a linear polarizer was placed at the laser output. By setting the polarizer parallel to the laser polarization and turning the half-wave plate, it was possible to control the excitation intensity while keeping the polarization orientation of the excitation beam constant (parallel to the incident plane). For ease of use, the excitation power was always measured after the intensity controller. The excitation power coupled into the microchannel, useful for fluorochrome excitation, was given by the power coupled into the chip by the excitation side microlens (calculated by Eq. (2.4)) minus the interface losses (air-photoresist, photoresist-Pyrex and Pyrex-water), which can be calculated using the Fresnel equations [57]. The excitation power coupled into the microchemical chip for an excitation microlens radius of 175 μm and for an incident angle of 45° was estimated to be 14 %, with the reflections losses for a polarization parallel to the incident plane of 1.5 %. Table 4.1 gives the calculated excitation power in the microchannel as a function of the excitation power. A measurement of the excitation power coupled into the chip was realized with a special chip for an incident angle of $\theta = 0°$. This chip was made up of the excitation side part of the detection system (Fig. 4.4) deposited on a single 1.5 mm thick Pyrex glass wafer (hence without microfluidic network). The power was measured by placing the photodetector head on the collection side of the chip, in place of the photodetector (Fig. 4.5). The difference between the calculated excitation power and the measured one is < 0.6 %. The actual excitation power was measured experimentally with a Labmaster power meter (Coherent, Auburn (CA), USA) equipped with an LM-2 detector based on a calibrated photodiode. The power meter precision was ±5 %.

Table 4.1: Calculated excitation power coupled into the microchannel.

Int. controller power (mW)	1.0	2.0	3.0	4.0	5.0	6.0	7.0	8.0	9.0
Microchannel power (mW)	0.05	0.09	0.14	0.19	0.24	0.28	0.33	0.38	0.42

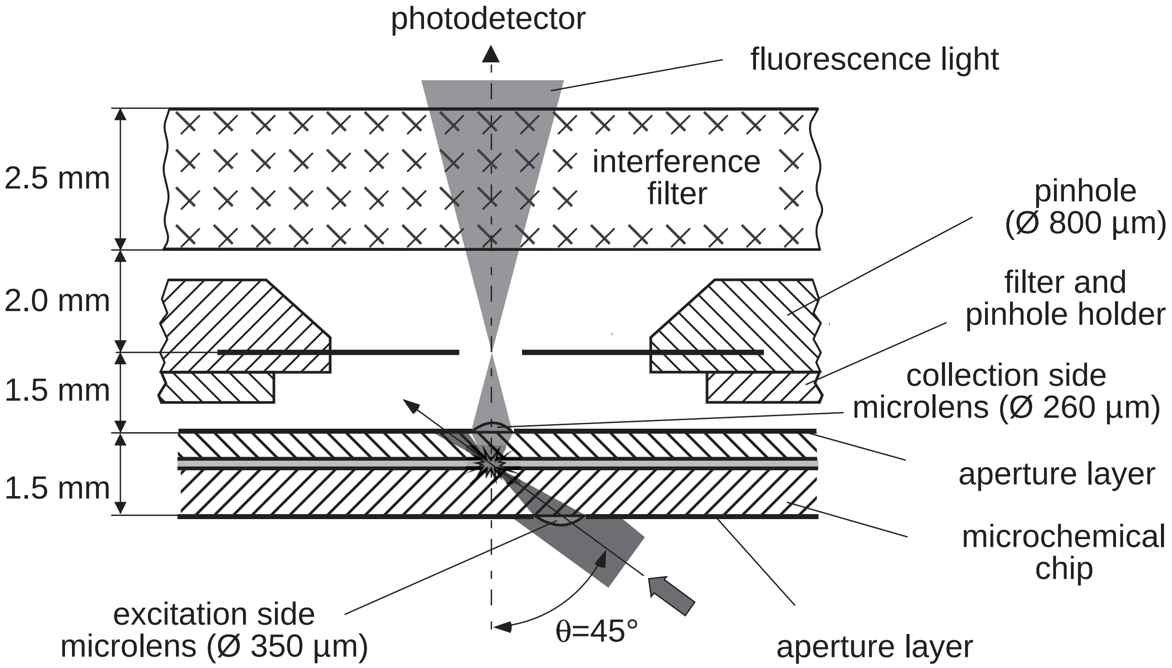

Figure 4.4: Cross section of the optical detection system.

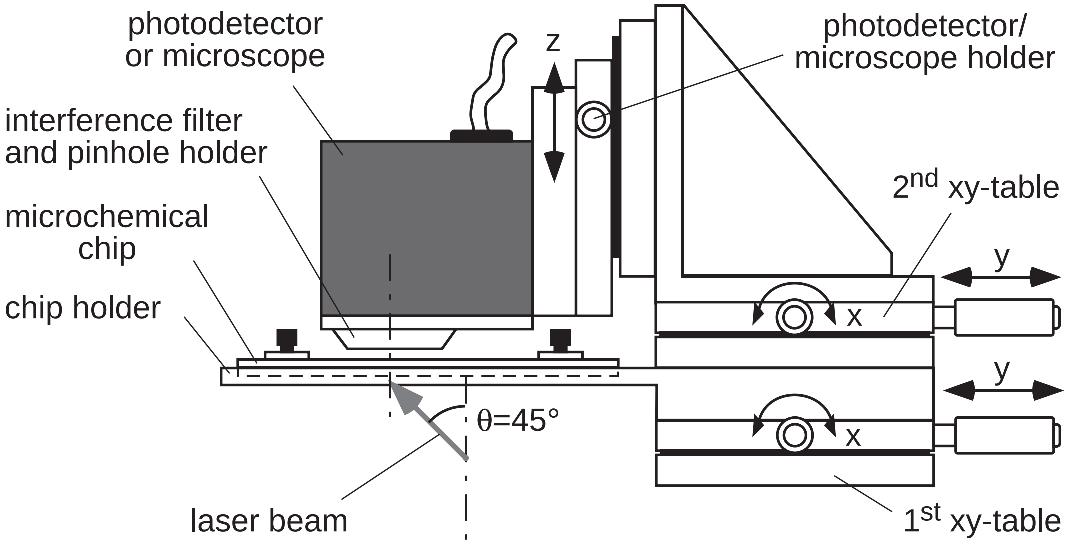

Figure 4.5: Chip holder and detection set-up.

Figure 4.5 shows the chip holder and the detection set-up. The chip holder was mounted on an xy-table so that the chip, and hence the microlens chosen for the excitation, could be precisely aligned with respect to the excitation beam. The detection system was composed of a second xy-table, mounted directly onto the chip holder, and a z-axis translation stage. Either a standard microscope or a photodetector holder could be mounted on the z-axis translation stage. The photodetector, an H5701-5 photomultiplier (Hamamatsu, Japan), could be used with the microscope, mounted in the ocular with a special adapter or mounted in place of the microscope by means of another holder. In both cases, the photomultiplier was designed for use with an interference filter and a pinhole. The 670DF40 interference filter (Omega Optical Inc, Brattelboro, USA) was specially designed for the Cy5™ fluorochrome. The transmission was $\sim 90\,\%$ between 662 and 688 nm, with an attenuation $> 10^{-3}\,\%$ at 633 nm (excitation wavelength). The pinhole was a precision 04 PPM-series mounted pinhole (Melles Griot Inc., Irvine (CA), USA). Figure 4.4 shows a closer view of how the pinhole and the interference filter were positioned with respect to the microchemical chip. Following the data sheet, the electronic bandwidth of the photomultiplier output signal is 20 kHz. The acquisition of the photomultiplier signal was realized with a PC equipped with a PCI-MIO-16E-4 data acquisition card and LabVIEW software (National Instruments Corp., Austin, USA).

4.3 Excitation beam

4.3.1 Excitation spot position and shape

Figure 4.6 shows the distance between the center of the excitation beam spot and the center of the circular excitation microlens as a function of the incident angle. These distances, y_s and y_c, were measured at the level of the microchannel and on the collection side surface (Fig. 2.15). The results are compared with the distances obtained from the raytrace simulation diagrams. Since direct observation of the microchannel was necessary, the microchemical chip used here was without collection side aperture and microlens arrays. Moreover, to make the outgoing excitation beam spot clearly visible on the collection side, the glass surface over the second microfluidic structure was depolished with fine-grained sand paper. The microchannels were filled with DI water. The images at the level of the microchannel were taken with a 6700-series CCD camera (Cohu Inc., San Diego (CA), USA) mounted on a 04 TFF 002 microscope body (Melles Griot Inc., Irvine (CA), USA) equipped with a ×25 (0.25) microscope objective (Spindler & Hoyer, Göttingen, Germany). The images on the collection side were taken by the same CCD

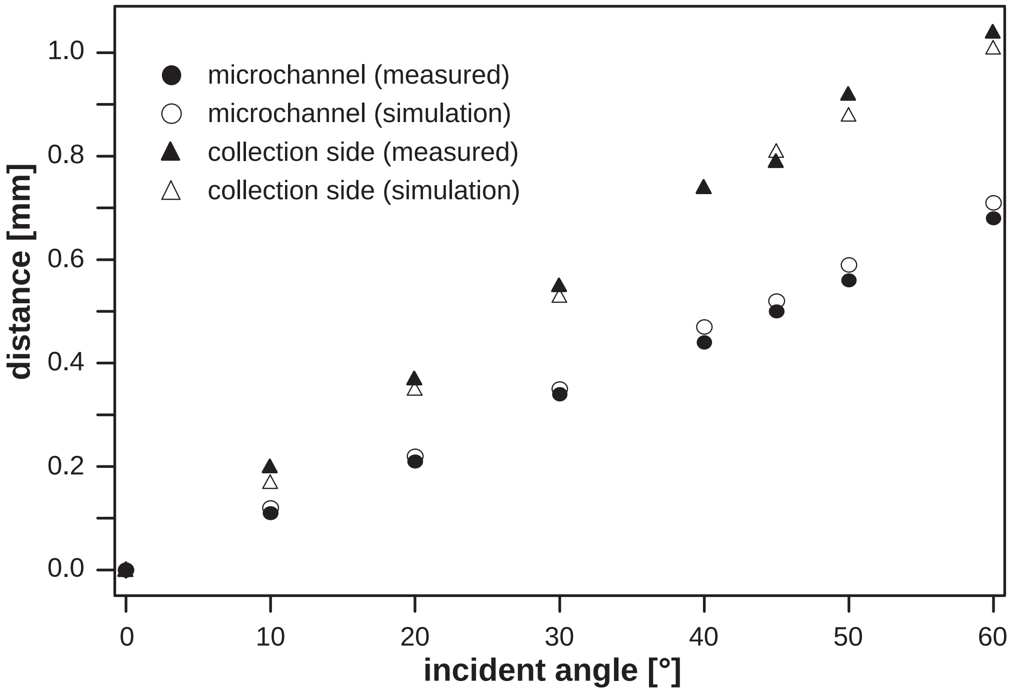

Figure 4.6: Position of the excitation spot with respect to the excitation side microlens.

camera mounted on a type-S M3Z stereoscopic microscope (Leitz, Heerbrugg, Switzerland). The image acquisition and treatment was realized on a Macintosh computer with Nih Imager software (Scion Corp., Frederick (MD), USA). The image acquisition set-up was calibrated by means of a USAF-1951 resolving power target.

The difference between the lengths measured on the CCD pictures and the lengths obtained from the raytrace diagrams are within 30 μm and 40 μm at the level of the microchannel and on the collection side surface, respectively. The measurements are in good agreement with the simulations.

The left side of Fig. 4.7 shows the CCD picture of the excitation spot at the level of the microchannel. The microchannel side walls are clearly visible on both sides of the excitation beam spot. Except for two "tails" trailing from the spot along the y-axis parallel with the microchannel, the spot shape and dimensions are in good agreement with the raytrace simulation shown on the right side of Fig. 4.7 (black spot). The spot measured on the CCD picture is 47 $\mu m \times 58\ \mu m$, whereas the spot measured on the raytrace diagram is 40 $\mu m \times 59\ \mu m$. The reason why the size of the spot along the y-axis is longer than the size measured on the CCD picture (and why one "spike" is brighter than the other one) is that the raytrace simulation diagrams present the ray distribution in a 2-D plane (parallel to the chip surface), while the CCD pictures show the rays scattered by the microchannel surface, which is a 3-D structure. Thus, the excitation beam begins to be scattered at the center of the microchannel position, in a plane situated $\sim 25\ \mu m$

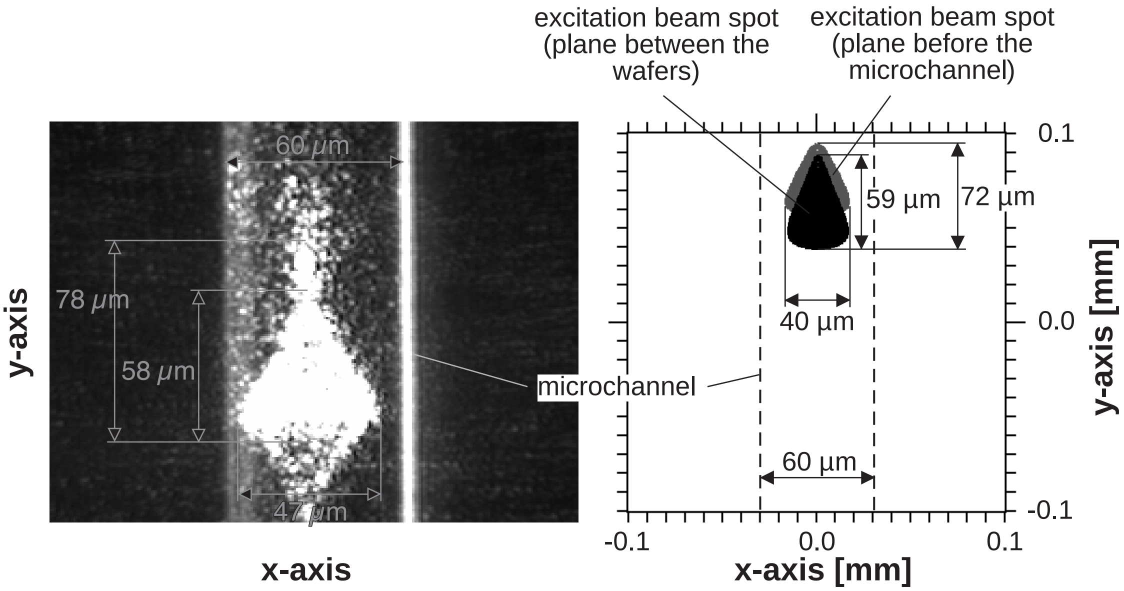

Figure 4.7: Picture of the excitation beam at the level of the microchannel (left picture) compared to the raytrace simulation result (right picture). The microchannel is filled with DI water.

before the interface between the two glass wafers (gray spot in the right picture of Fig. 4.7). Then, as the light continues along its path, the beam is scattered by the microchannel walls. The distance between the top of the gray spot (ray distribution in the plane where the rays begin to be scattered by the microchannel) and the bottom of the black spot (ray distribution in the plane situated at the interface between the wafers) is comparable on the CCD picture and on the raytrace diagram (78 μm and 72 μm, respectively). The tails come mainly from aberrations due to the off-axis illumination scheme. When the circular excitation microlens with 350 μm radius (Fig. 4.8a) is replaced by a 350 $\mu m \times 400\ \mu m$ elliptical lens (Fig. 4.8b) the tails disappear.

Figure 4.9 shows the CCD picture (left) and the raytrace diagram (right) of the excitation spot on the collection side. Due to the large surface roughness and the fact that the picture was not taken in the dark, the exact shape of the spot is difficult to determine. The presence of the excitation beam reflection on the excitation side (the bright spot on the right) makes the spot shape and size even more difficult to determine. Although the shapes seem similar in both cases, the spot size measured on the CCD picture seems larger (210 $\mu m \times 420\ \mu m$) than the spot of the raytrace diagram (106 $\mu m \times 290\ \mu m$).

The fact that the reflection of the excitation beam on the excitation side of the chip is visible, and that there is a shift of Δx between the midpoints of the collection side spot and the excitation microlens, is due to the use of a stereoscopic microscope. The CCD camera is connected to one ocular only and hence views the chip surface under a certain angle. Since the collection side spot, the microchannel and the excitation microlens are

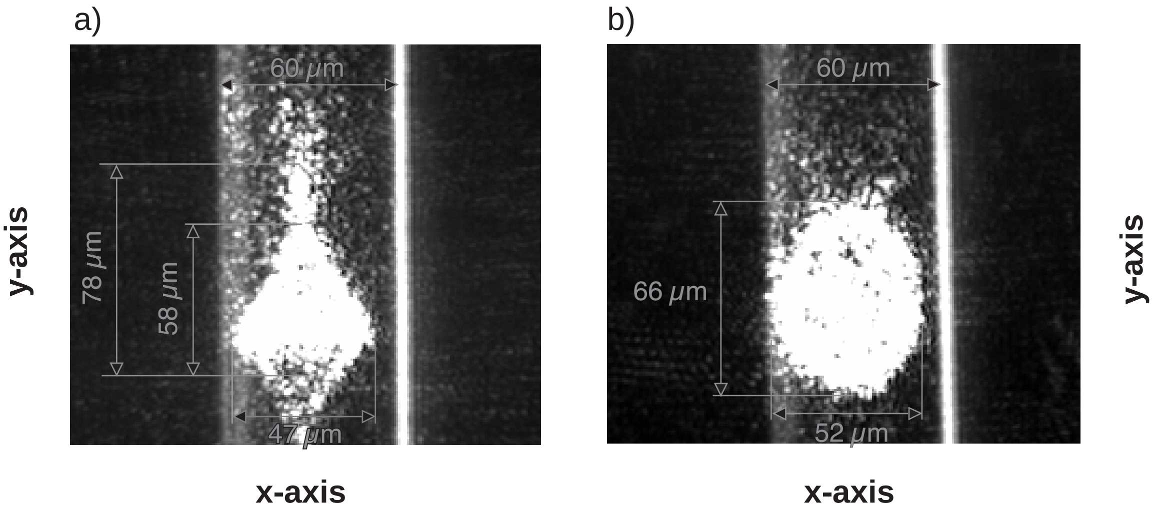

Figure 4.8: Images of the excitation beam spot when (left) a circular microlens and (right) an elliptical microlens are used on the excitation side. The microchannel was filled with DI water.

not situated in the same plane, they appear to be shifted with respect to each other.

4.3.2 Influence of the microchannel excitation on the scattering

To evaluate the background light generated by the scattering of the excitation beam at the microchannel interfaces, and especially by the wet-etched surface of the microchannel (Chap. 3), the signal intensity was recorded under the same conditions (same set-up, same excitation intensity, and same detection sensitivity) for two different chips, one having a microfluidic network, the other one not. The latter chip was simply a single 1.5 mm thick Pyrex glass wafer. The same detection system (microlens and aperture arrays on both sides of the chip) was deposited on both systems. The microchemical chip with the microfluidic network was filled with DI water. The excitation beam was focused onto both chips by means of a circular microlens. The 670DF40 interference filter was placed in front of the photodetector. The sampling frequency was 10 Hz (10 samples per second) and all data were smoothed using a 21 point box smooth algorithm implemented in Igor Pro (Wavemetrics, Lake Oswego, USA). The equivalent bandwidth of these 21 sample points taken from the 20 kHz bandwidth photomultiplier output signal is 950 Hz. During the first 30 s the signal was recorded with the $HeNe$ laser switched on. For the next 30 s the $HeNe$ laser was switched off (no excitation). When the laser was on, the difference between the average signal for the chip with and without the microfluidic network is less than 6 % (Fig. 4.10). The signal for the system without the microchannels is greater though and this difference can be explain by two arguments: the reflection of part of the

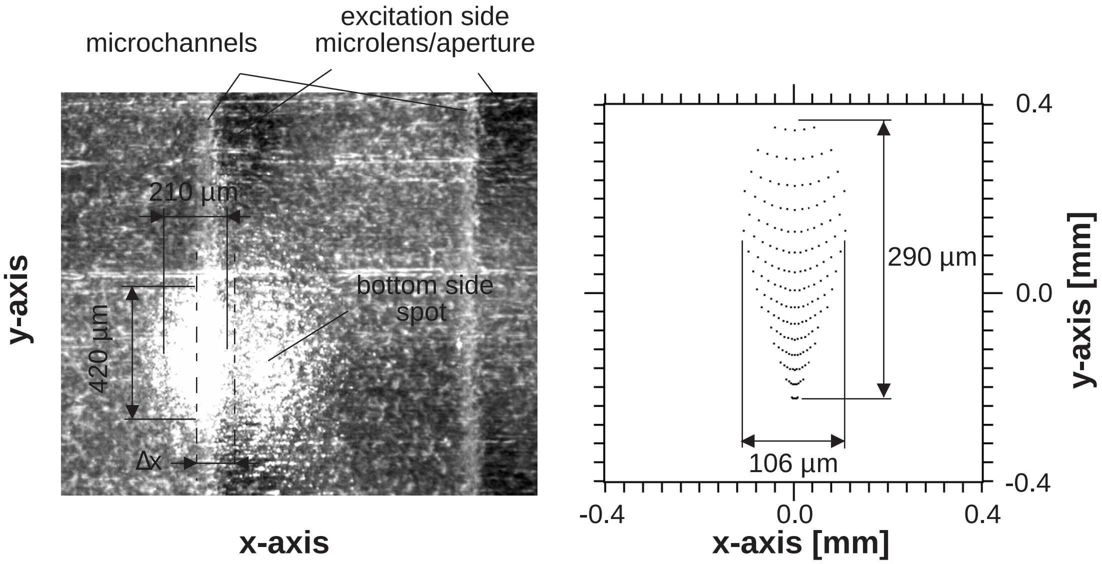

Figure 4.9: Image of the excitation beam spot on the collection side of the chip (left) compared to the raytrace simulation result (right). The microchannel was filled with DI water.

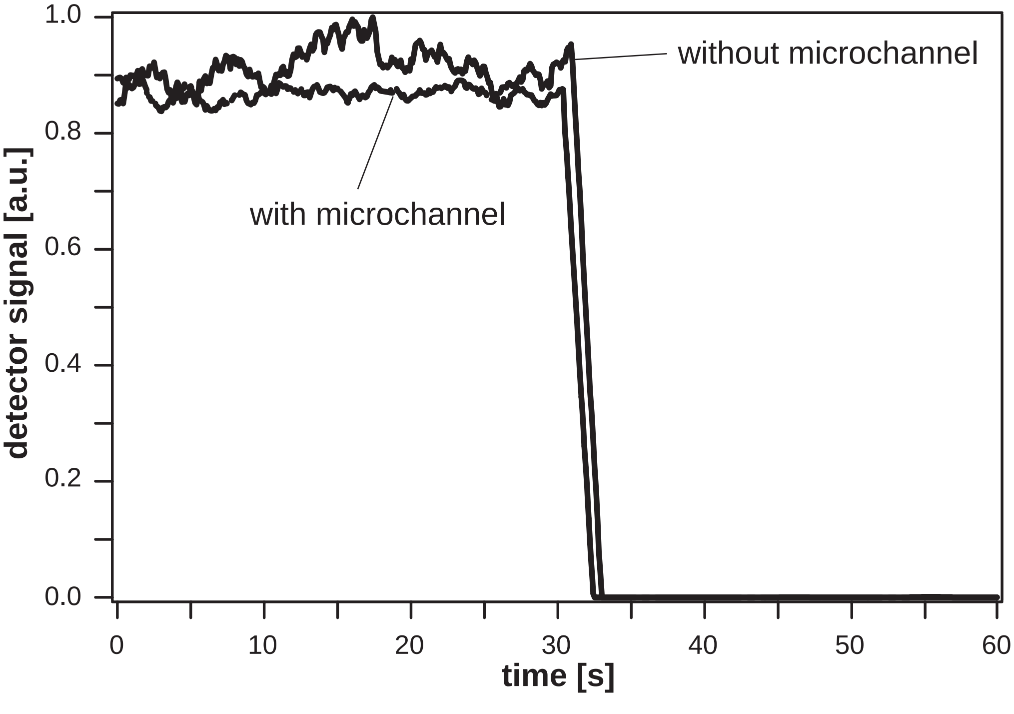

Figure 4.10: Signal recorded for a chip with and without a microfluidic network. Excitation power of $0.24 \pm 0.02\ mW$.

excitation beam at the microchannel interfaces and/or, due to the lack of microchannel, a displacement of the position of the excitation beam y_c toward the collection aperture and hence an increase of the background light collection (Fig. 2.15). Since the Fresnel equations [57] gives an excitation beam reflection lower than 0.1 % for a polarization in the incident plane, the signal difference is mainly due to the modification of the position of the excitation beam. Raytrace simulations confirmed that y_c is 17 μm smaller for a system without microchannels than for a system with the microchannels. In any case, the scattering of the excitation light by the microchannel surface is not an issue for the signal-to-noise ratio compared to excitation light which reaches the photodetector with or without microchannels.

4.4 Fluorescence light measurements

4.4.1 Influence of the excitation microlens shape

As shown previously in Sec. 4.3.1, the size and shape of the excitation spot in the microchannel is different when focused by a circular microlens (radius 350 μm) or by an elliptical microlens (350 μm × 400 μm). Figure 4.11 shows the fluorescence spots taken in the same chip and under the same conditions as those of Fig. 4.8 but with the microchannels filled with a 50 μM Cy5™ solution instead of DI water. In both cases, the dimension and shape of the spots are the same. The detection volume can be evaluated by the intersection of a cylinder of radius r (r being the average radius of the excitation spot between the two wafers) with a perpendicular half-cylinder having a 30 μm (microchannel) radius. The detection volume is 60 ± 10 pL for the circular excitation microlens (without the tails seen in Fig. 4.11a) and 66 ± 11 pL for the elliptical one.

The fluorescence signal was then recorded in a chemical chip with the complete detection system (Fig. 4.4). Cy5™ solution concentrations ranging from 50 μM to 0 nM (buffer solution only). The signal was first recorded for the full concentration range with the same excitation microlens, then the measurements were repeated with the other microlens. The same stock solution of each dye concentration was used for both series of measurements. Figure 4.12 shows the recording procedure used for all the measurements and the signal obtained for DI water and a 10 nM Cy5™ solution (excitation power of 0.24 ± 0.02 mW). For the Cy5™ solution the signal was recorded during 50 s with the pump switched on then for another 50 s with the pump switched off. The average signal was calculated from 300 data points, between the 10^{th} and the 40^{th} s for the pump on and between 70^{th} and the 100^{th} s for the pump off. The data for the pump switched off were taken only after

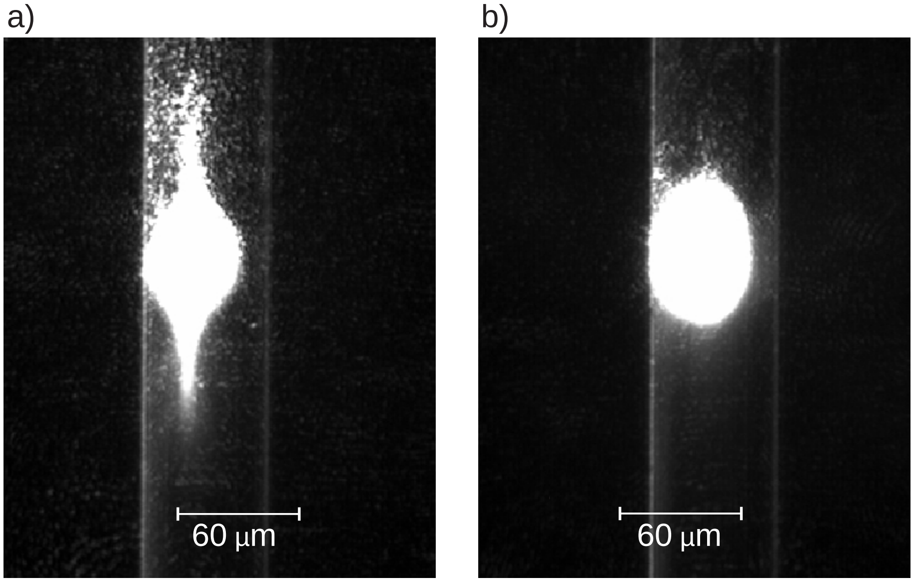

Figure 4.11: Fluorescence spots in a microfluidic channel when the light is focused by a circular microlens (left) and by an elliptical microlens (right). The images are taken without an interference filter.

70 *s* because the signal was only stable after 10-20 *s*. For the DI water, the procedure was the same, except that the excitation laser was switched off after 90 *s* to give an idea of the background level due the remaining excitation beam reaching the photodetector. The average signal for DI water with the pump switched off was calculated with 200 points, between the 70 *s* and the 90 *s*.

Figure 4.13 shows the average signal with the pump switched on, when the excitation beam is focused with an elliptical and a circular microlens. The signals obtained for the buffer solution are presented as horizontal lines. The absolute values of the average signal obtained with the elliptical excitation microlens ($\overline{S}_E$ and $\overline{S}_{BE}$) were greater than the signals obtained with the circular microlens ($\overline{S}_C$ and $\overline{S}_{BC}$). On average, $\overline{S}_E$ is 15 % greater than $\overline{S}_C$ whereas, for the buffer solution, $\overline{S}_{BE}$ is 9 % greater than $\overline{S}_{BC}$. Since the size of the elliptical excitation microlens is 13 % greater than the circular excitation microlens, a signal difference of this magnitude was expected. The better excitation spot shape obtained with the elliptical microlens (Fig. 4.11) explains why the signal difference is more important for the microchannels filled with Cy5™ solution ($\overline{S}_E - \overline{S}_C$), than for the microchannels filled with DI water ($\overline{S}_{BE} - \overline{S}_{BC}$). Therefore, the elliptical microlens, beside enabling a slightly larger excitation intensity coupling into the microchemical chip, improves slightly the signal difference when the microchannel are filled with Cy5™ solution and with buffer solution, and hence improves the signal-to-noise ratio.

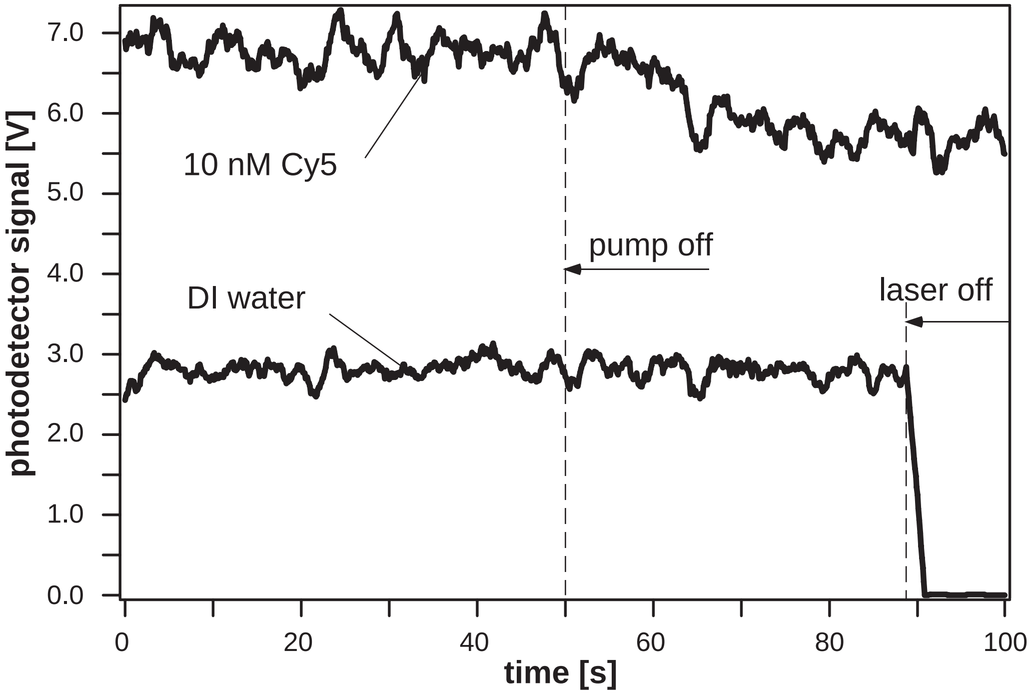

Figure 4.12: Photodetector signal for a 10 nM Cy5™ solution and DI water. The data are smoothed using a 21 point box smooth algorithm.

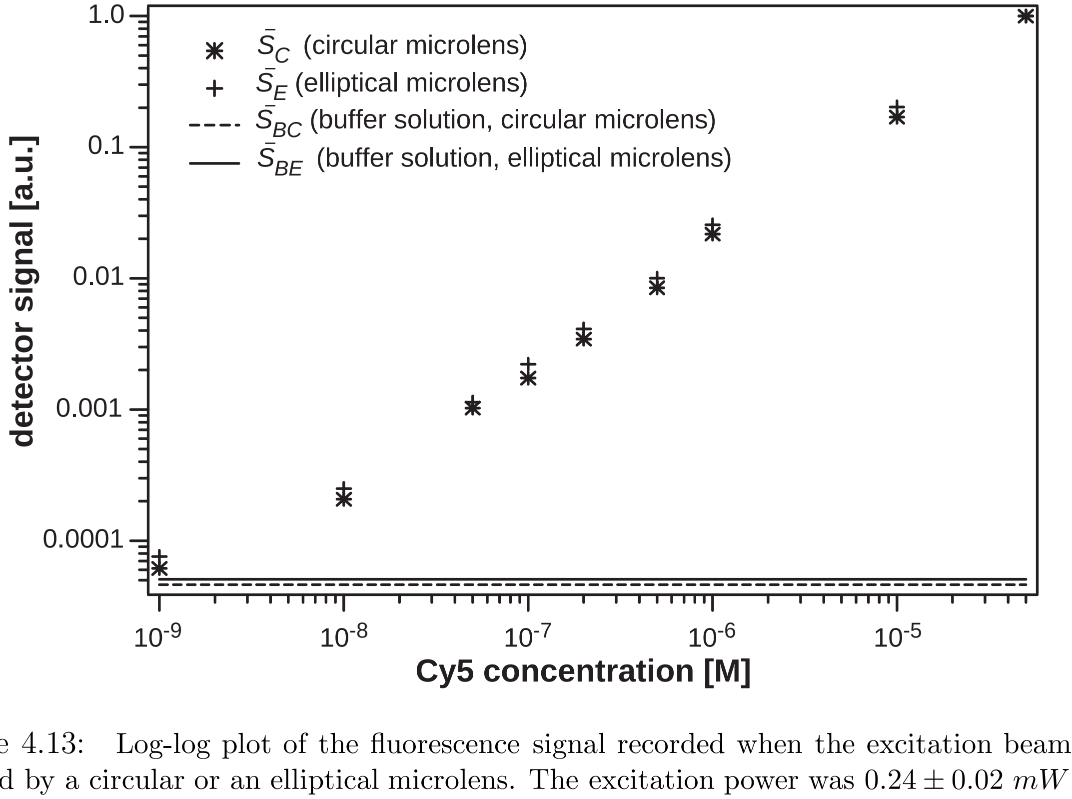

Figure 4.13: Log-log plot of the fluorescence signal recorded when the excitation beam was focused by a circular or an elliptical microlens. The excitation power was 0.24 ± 0.02 mW.

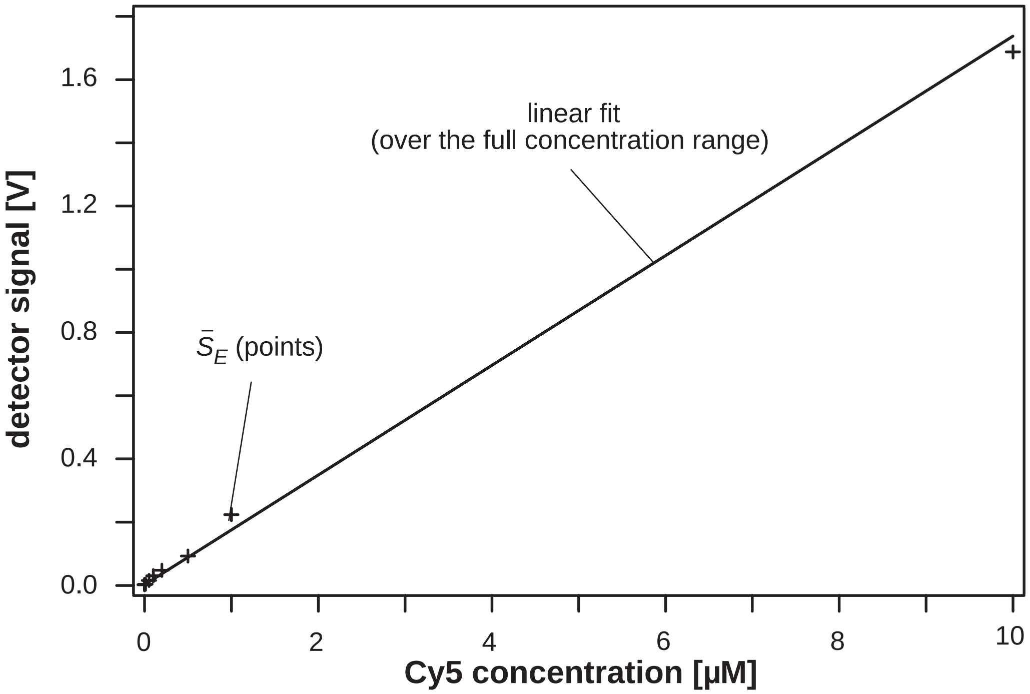

Figure 4.14: Fluorescence signal recorded for Cy5^{TM} concentrations ranging from 1 nM to 10 μM (excitation power of 0.24 ± 0.02 mW). The linear fit was calculated over the full concentration range (1 nM to 50 μM).

4.4.2 System sensitivity

As shown in Fig. 4.14 and Fig. 4.15, which is an expanded view of Fig. 4.14 at lower concentrations (below 500 nM), the average photodetector signal is proportional to the Cy5^{TM} solution concentration from 1 nM to 50 μM. The slope of the curve is $\alpha = 174 \cdot 10^3\ V\ M^{-1}$.

Figure 4.16 is again an expanded view of Fig. 4.14, showing the average signal for Cy5^{TM} concentrations ≤ 50 nM, the average background signal obtained when the microchannels were filled with buffer solution only ($\overline{S}_{BE}$) and the detection floor. The detection floor is defined as a signal which is three times the total noise σ_N above the background signal. The total noise is calculated as the sum of the variances σ_E^2 and σ_{BE}^2 of the fluorescence $\overline{S}_E$ and the background $\overline{S}_{BE}$, respectively, which means

$$\sigma_N = \sqrt{\sigma_E^2 + \sigma_{BE}^2}. \tag{4.1}$$

In Fig. 4.16 the detection floor was calculated for 1 nM concentration. Since $\sigma_N = 188 \cdot 10^{-6}\ V$ and $\overline{S}_{BE} = 2.3 \cdot 10^{-3}\ V$, the limit of detection (LOD) of the system calculated from the intersection of the linear response curve ($\alpha = 174 \cdot 10^3\ V\ M^{-1}$) with the detection floor is $LOD = 3.3\ nM$.

The signal-to-noise ratio (power of the background corrected signal/noise power) is

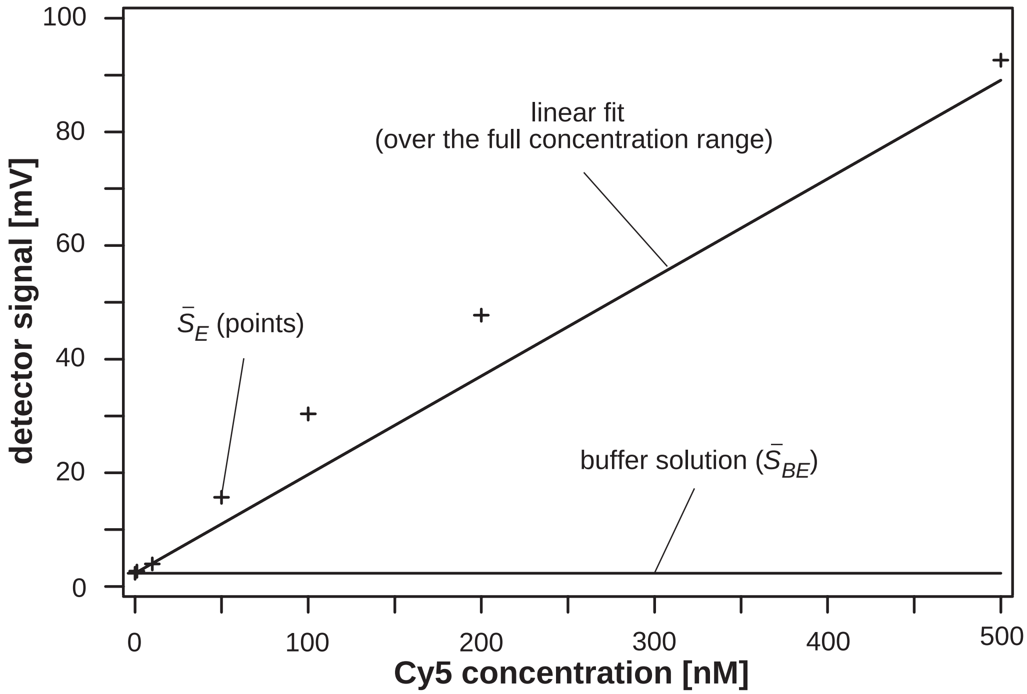

Figure 4.15: Photodetector signal vs. dye concentration. The excitation beam was focused by an elliptical microlens and the excitation power was $0.24 \pm 0.02\ mW$. The linear fit was calculated over the full concentration range ($1\ nM$ to $50\ \mu M$)

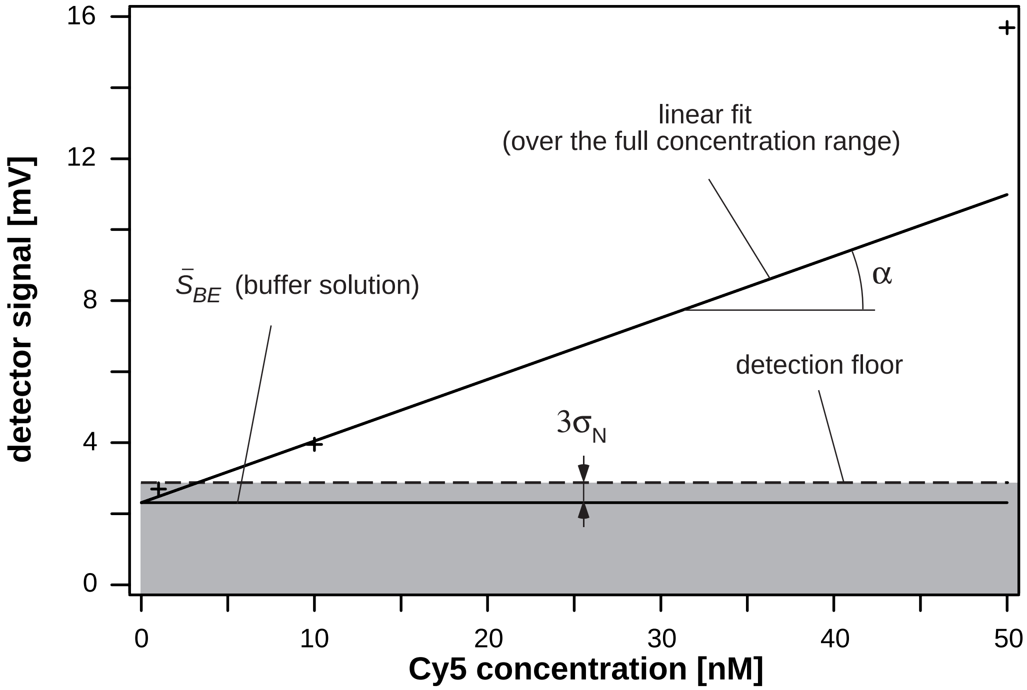

Figure 4.16: Photodetector signal vs. dye concentration. The excitation beam was focused by an elliptical microlens, and the excitation power was $0.24 \pm 0.02\ mW$. The detection floor was calculated for $1\ nM$ concentration. The linear fit was calculated over the full concentration range ($1\ nM$ to $50\ \mu M$)

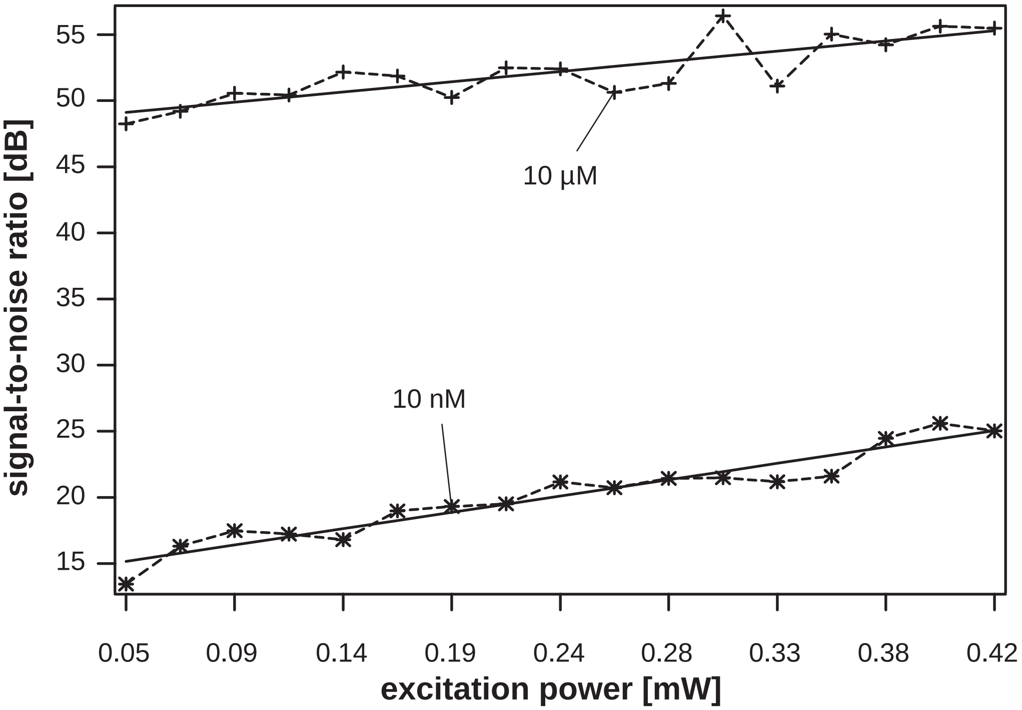

Figure 4.17: SNR$_{dB}$ as a function of the excitation power.

given by the relation

$$SNR = \frac{\left(\overline{S}_E - \overline{S}_{BE}\right)^2}{\sigma_E^2 + \sigma_{BE}^2}, \tag{4.2}$$

or

$$SNR_{dB} = 10 \log \frac{\left(\overline{S}_E - \overline{S}_{BE}\right)^2}{\sigma_E^2 + \sigma_{BE}^2}. \tag{4.3}$$

The SNR of the 1 nM Cy5™ signal is hence 4.3 or 6.4 dB. As emphasized by Mathies *et. al* [70], the SNR increases as the excitation power increases up to an optimum. Then, owing to ground state depletion and photobleaching, the SNR will decrease. The power density giving the optimum SNR for a 10 nM Cy5™ fluorochromes was determined by Jiang *et. al* [41][1] and is $\sim$ 540 $W\,cm^{-2}$ for a flow rate of 3.8 $\mu L\,min^{-1}$. Figure 4.17 shows the SNR$_{dB}$ as a function of the excitation power for a 10 μM and a 10 nM Cy5™ solutions. The excitation power ranges from 0.05 mW to 0.42 mW, corresponding to a power density range from 5 $W\,cm^{-2}$ to 44 $W\,cm^{-2}$. Both signals are proportional to the excitation power and hence, even if the flow rate in our chip is $\sim$ 6 smaller, the maximum excitation intensity before bleaching is not yet reached.

Since $\overline{S}_E$ and $\overline{S}_{BE}$ and σ_N^2 (assuming shot noise limitation) are proportional to the

---

[1] in this reference, the SNR was defined by the background corrected fluorescence signal divided by the standard deviation which gives a SNR equivalent to square root of the SNR defined in Eq. 4.2.

Table 4.2: system parameters and limit of detection comparison.

	Jiang *et al.*	system of this work
power density (in microchannel)	$1000\,W\,cm^{-2}$	[1]$8.5\,W\,cm^{-2}$
spot size (diameter)	$18\,\mu m$	$60\,\mu m$
excitation power (in microchannel)	$2.6\,mW$	$0.24\,mW$
analog signal filtering	low-pass filter cut-off 25 Hz	photomultiplier output bandwidth of 20 kHz
sampling rate	$50\,Hz$	$10\,Hz$
data smoothing	21 pts. box	21 pts. box
equivalent bandwidth	$2.4\,Hz$	$950\,Hz$
[2]LOD (SNR = 9)	$1.5\,nM$	$3.3\,nM$
[3]LOD @ $1\,Hz$	$1.0\,nM/\sqrt{Hz}$	$0.24\,nM/\sqrt{Hz}$
[4]LOD @ $1\,Hz$ and $1\,mW$	$1.6\,nM\sqrt{mW}/\sqrt{Hz}$	$0.05\,nM\sqrt{mW}/\sqrt{Hz}$

[1] calculated for an excitation power of 0.24 mW and a spot radius of 60 μm.
[2] 670DF40 Omega interference filter used in both systems.
[3] LOD referred to the same equivalent bandwidth.
[4] LOD referred to the same equivalent bandwidth and to the same excitation power.

excitation power, the SNR for an excitation power $P_2 = k\,P_1$ compared with the SNR for the excitation power P_1 is given by

$$SNR\ (P2) = \frac{\left(k\,\overline{S}_E - k\,\overline{S}_{BE}\right)^2}{k\ (\sigma_E^2 + \sigma_{BE}^2)} = k\,SNR\ (P1)\,. \tag{4.4}$$

Thus, for $k = 0.42\ mW/0.05\ mW = 8.9$, the maximum and minimum power in Fig. 4.17, the SNR increase should increase by a factor of 8.9 or 9.5 dB. This result is confirmed with the 10 nM solution (Fig. 4.12) where a SNR$_{dB}$ difference of about 10 dB is measured. For the 10 μM however, the measured SNR$_{dB}$ difference is only about 6 dB. The SNR$_{dB}$ difference between the 10 μM and 10 nM is $\sim$ 34 dB. Since the fluorescence signal $\overline{S}_E$ is proportional to the fluorochrome concentration (Fig. 4.14) and for increasing fluorescence signal the total noise σ_N^2 will be dominated by σ_E^2, which is proportional to $\overline{S}_E$ (assuming shot noise limitation) should increase proportional to the concentration. This behavior is confirmed by the 30 dB improved SNR for the increase of the concentration from 10 nM to 10 μM shown in Fig. 4.17.

Results for a comparable microchemical chip, but with a confocal epifluorescence detection scheme, were reported by Jiang *et al.* [41]. With the same interference filter as we used here and before optimization of the excitation source and the collection system parameters, they reached a limit of detection (LOD) of 1.5 nM for Cy5™. As excitation source, they used a 11.5 mW laser diode at $\lambda = 634.5\ nm$. The photodetector signal was filtered with a 25 Hz low-pass filter and the A/D sampling rate was 50 Hz. The digital signal was smoothed by means of a 21 point box smooth. Table 4.2 gives a comparison of our results and those reported in [41]. The first part of Table 4.2 summarizes the characteristics of the systems. The second part of Table 4.2 gives a comparison of the limit of detection (LOD) reached for the two systems, as raw data and terms of LOD for equal bandwidth and for equal bandwidth and equal excitation power (in the microchannel). This comparison shows, that the integrated system presented in this thesis is 10–20 times more sensitive. With a more selective interference filter and further optimization of excitation source and collection parameters, Jiang *et. al* [41] reached an ultimate LOD of 9 pM of Cy5™. The better performance of the off-axis illumination scheme compared to the epifluorescence detection scheme is due to a better suppression of background light. In the epifluorescence scheme, $\sim 4\,\%$ of the excitation power is reflected back on the surface of the microchemical chip. Part of this light is then collected by the microscope objective which increases the background signal. This is not the case for the off-axis system since the fluorescence light collection is not performed on the same side of the chip as the illumination.

4.4.3 Cross-talk

The amount of fluorescence and scattered excitation light emitted from a microchannel and collected by the collection optics of a consecutive microchannel was determined as shown in Fig. 4.18a and Fig. 4.18b. The first measurement (Fig. 4.18a) was performed by exciting the fluorescence dye in microchannel n° 1 and measuring the signal intensity in the collection optics of microchannel n° 2 (cross-talk signals). To obtain the highest possible fluorescence signal (and hence the highest cross-talk signal intensity), a 50 μM solution Cy5™ was injected in the microchannels. The second measurement (Fig. 4.18b) was performed as previously by exciting the fluorescence dye in microchannel n° 1 and measuring the signal intensity in microchannel n° 2. This time though, microchannel n° 2 was filled with DI water whereas 50 μM Cy5™ solution was injected in microchannel n° 1,

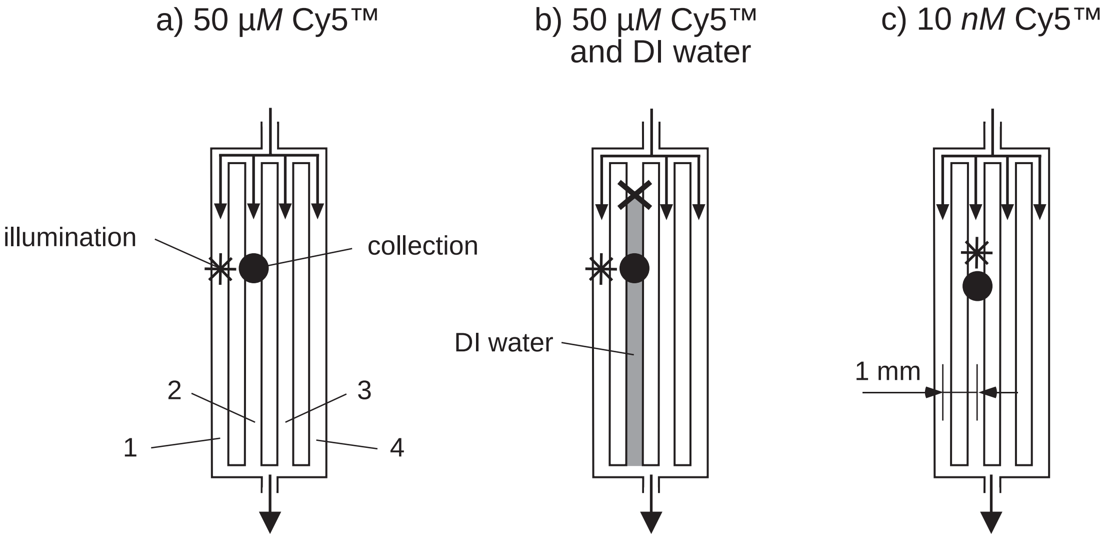

Figure 4.18: Cross-talk measurement layout.

3 and 4. This measurement was possible because microchannel n° 2 get clogged during rinsing of the chip with DI water. Finally, the signals obtained in the case of Fig. 4.18a and Fig. 4.18b were compared to the signal obtained when the fluorescence dye excitation and the fluorescence light collection were carried out in microchannel n° 2 (Fig. 4.18c). A 10 nM solution Cy5™ was injected in the microchannels in that case.

The cross-talk signals were recorded during 40 s with the liquid flow pump switched on while the next measurements were performed with the pump switched off. After 80 s, also the excitation ($HeNe$ laser) was switched off. The comparison signal (Fig. 4.18c) was recorded during 60 s with the pump switched on and the next measurements with the pump switched off. Figure 4.19 shows the two cross-talk signals (designated by letter a and b, respectively) and the comparison signal (designated by letter c). These letters referred also to the measurement layout of Fig. 4.18.

Since both cross-talk signals decrease when the pump is switched off (indicative for photobleaching), it can be concluded that the cross-talk is mainly due to fluorescence light, rather than scattered excitation light. Moreover, the cross-talk signals are about the same wether the microchannel n° 2 is filled with Cy5™ solution (a) or filled with DI water (b) (the average signal is 1.8 V and 1.7 V, respectively). Hence, the measured fluorescence originates from microchannel n° 1 and not from the Cy5™ solution in microchannel n° 2 excited by scattered light from microchannel n° 1. The system sensitivity, for collection microlenses placed 1 mm apart would be limited to $\sim$ 10 nM, with samples of high Cy5™ concentration in adjacent microchannels. The cross-talk C_T is given by the photodetector signal intensity $\overline{S}_c$ measured in the same microchannel as the excitation (case of Fig. 4.18c) divided by the signal intensity $\overline{S}_a$ measured in a consecutive microchannel (case of Fig. 4.18a) for the same fluorochrome concentration as $\overline{S}_c$. Since $\overline{S}_c$ and $\overline{S}_a$ are,

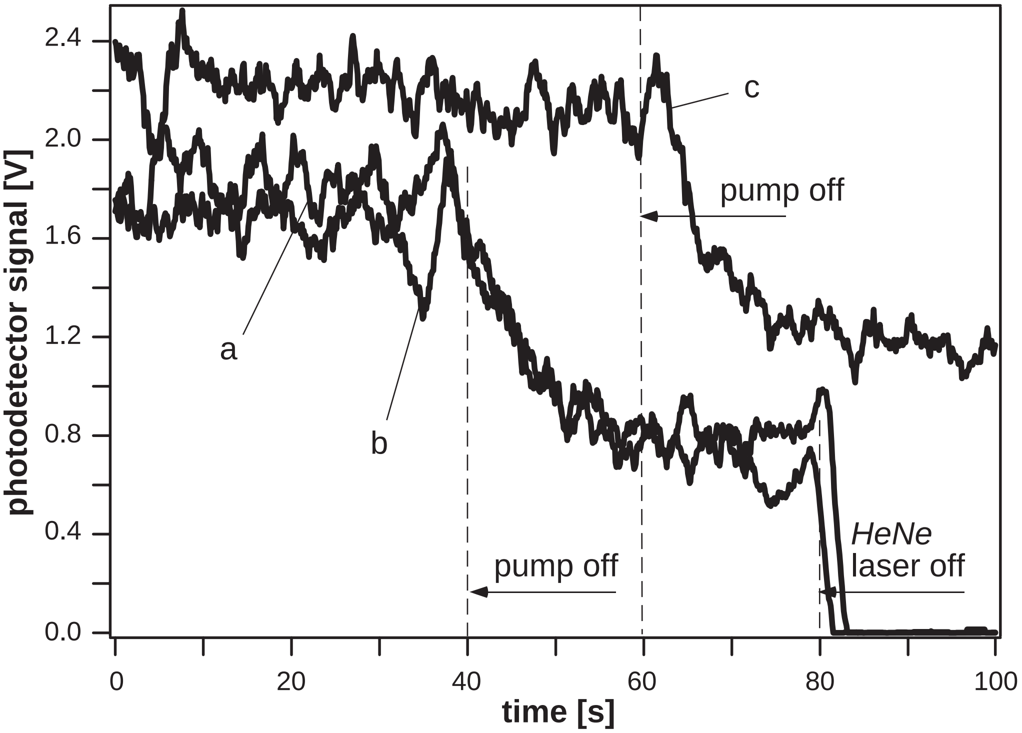

Figure 4.19: Signal measured a) with 50 μM Cy5™ solution in every microchannels b) with DI water in microchannel n° 2 and c) with a 10 nM Cy5™ solution in every microchannels (collection and excitation on the same microchannel). The excitation power is $0.24 \pm 0.02\ mW$.

for a 50 μM Cy5™ solution, $10 \cdot 10^3\ V$ and $1.8\ V$, respectively, $C_T = 10 \cdot 10^3/1.8 \simeq 5'600$. $\overline{S}_c$ was corrected to take into account the difference of sensitivity of the photodetector with $\overline{S}_a$). C_T could be further reduced by increasing the distance between microchannels or by placement of the collection microlenses in staggered rows instead of a single row, to preserve the 1 mm distance between channels.

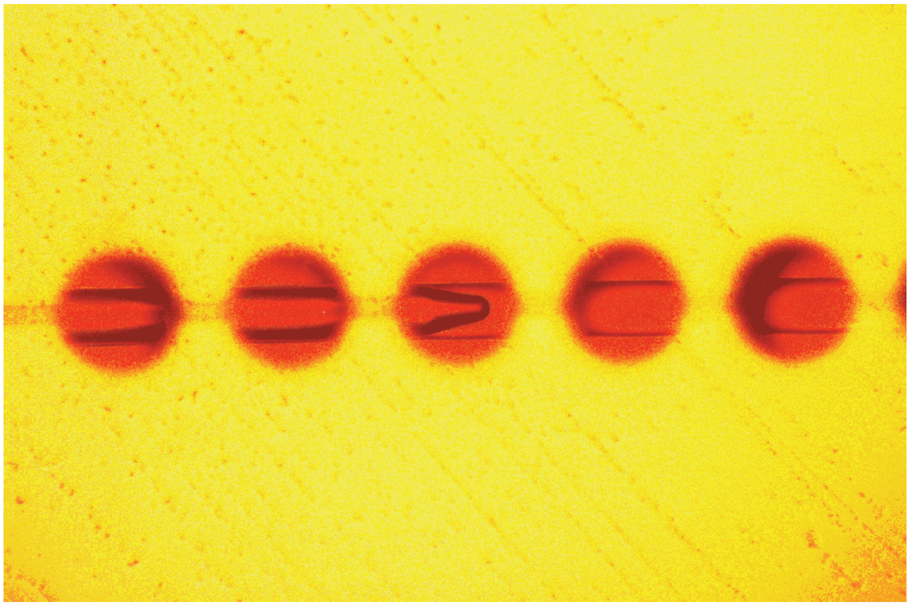

Figure 4.20: Liquid flowing from left to right in a 110 μm wide and 50 μm deep microchannel. The microchannel is magnified by 310μm radius and 64 μm high photoresist microlenses (focal length of ~ 280 μm).

Chapter 5

Summary and conclusions

The present thesis is devoted to the development and the integration of a fluorescence detection system onto a microchemical chip designed for basic heterogeneous immunoassays. The refractive microlenses composing the detection system are typically 260 μm to 400 μm wide and 25 μm to 50 μm high. The detection system, as well as the microchemical chip, have been miniaturized by using microfabrication technologies. The overall system (without the light source and the photodetector) is less than 2.1 mm thick. The detection volume is $\sim 60\ pL$ and the limit of detection for Cy5™ in 50 mM phosphate buffer (pH 7.4) is 3.3 nM with a signal integration time of 525 μs (950 Hz equivalent bandwidth) and 0.7 mW excitation power. This limit corresponds to the detection of $\sim 120 \cdot 10^3$ molecules.

The thesis focuses first on general issues of fluorescence detection, on how to realize and integrate detection systems and on raytrace simulations and evaluations of the proposed detection systems. The successful implementation of a detection system relies on the following factors: the excitation beam must be focused into a tiny detection volume, the fluorescence light must be collected and separated from unabsorbed excitation light, and finally, the fluorescence light must be transported to the photodetector. The thesis shows how an adroit placement and combination of microfabricated lenses and stops can fulfil all these requirements.

An off-axis detection scheme (the excitation beam forms a 45° angle with respect to the collection axis) is integrated onto the microchemical chip. The microchemical chip is made of a glass wafer in which microfluidic networks are patterned and sealed by a second glass wafer. Even if the fabrication of refractive microlenses and microfluidic networks is based on commonly used techniques, the realization of a system combining stacks of microlens and aperture arrays on both sides of a microfluidic chip is a major success. The possibility to integrate an intermediate aperture layer between the sealed glass wafers is also demonstrated.

Measurements with the microchemical chip are presented in the last part of the thesis. The shape and position of the excitation spot, measured in the microchannel and on the collection side of the chip, are in good agreement with raytrace simulations. The photodetector signal is proportional to the Cy5™ concentration in the range from 1 nM to 50 μM. The limit of detection (corresponding to 3σ or $SNR = 9$) is 3.3 nM (950 Hz equivalent bandwidth) for a 0.7 mW excitation power. The cross-talk measured between two adjacent microchannels at 1 mm distance is 1:5600, meaning that less than $\sim 0.18 \cdot 10^{-3}\,\%$ of the fluorescence light power emitted from one microchannel reaches the photodetector of the adjacent microchannel.

The comparison with a microchemical chip where the fluorescence detection was carried out with a confocal epifluorescence set-up shows that the integrated system is 10 to 20 times more sensitive. These good results show that the combination of geometrical and spectral filtering enables to efficiently reduce the false light reaching the photodetector. The better performance of the off-axis illumination scheme compared to the epifluorescence detection scheme is due to a better suppression of background light. In the epifluorescence scheme, $\sim 4\,\%$ of the excitation power is reflected back on the surface of the microchemical chip. Even for an epifluorescence detection scheme combined with a confocal set-up, part of this light is still collected by the microscope objective, which increases the background signal. This is not the case for the off-axis system, since the fluorescence light is not collected on the same side of the chip as the illumination. We believe that with improved electronic signal processing and a further optimization of the detection system, a limit of detection in the range of 100 pM should be possible. Since the control of false light is also a major issue in absorbance detection, integration of micro-optical elements onto a microchemical chip could also be used to realize absorbance based detection systems.

This work presents a solution for the realization of microchemical chips integrating small and closely spaced microoptical elements, their precise alignment with respect to microfluidic channels, and the realization of an original detection system capable of detecting pM Cy5™ concentration. This kind of system is an important step toward the realization of high throughput μTAS. Among the four detection system configurations presented in Chap. 2, the central stop (with the stop on the collection side of the chip) and the off-axis detection schemes are the most promising ones. The off-axis system has the advantage that the excitation beam is directed sideways, and also that it is less sensitive to fabrication tolerances than the central stop system. However, the central stop system could be a good option, because integration of excitation light sources is easier than for the off-axis system. Since the propagation axis of the excitation beam is perpendicular (incident angle of 90°) to the microchemical chip surface for the central stop system, the wafer, or part of the wafer, with the excitation light sources could be placed onto precise spacers and aligned with respect to the excitation side microlens/aperture array using the same alignment marks as those used for deposition of the microlens/aperture arrays. In the case of the off-axis system, an incident angle (here 45°) must also be ensured in addition to the alignment with respect of the microlens/aperture arrays. In any detection scheme, replacing chromium aperture layers by an absorbing material (at the excitation beam wavelength) would reduce the false light intensity inside the microchemical chip and hence will improve the SNR. For example, silicon nitride, silicon dioxide or silicon carbide layers could be used. The techniques presented in this work enable the realization of chips with large numbers of channels in parallel and hence reduce the cost per analysis. The system can also be produced in plastic to further reduce the cost. The fabrication techniques described in this work could be used to make the moulds for replication by plastic injection or hot embossing. Such techniques have already been investigated for refractive/diffractive microlenses [71, 12] and microfluidic channel [72, 73] replication.

Chapter 6

Acknowledgements

I would like to take this occasion to express my gratitude and appreciation to Prof. Dändliker and Prof. Herzig for offering me the opportunity to work in the facinating world of microsystems, optics and microoptics and for all they taught to me. One of the most interesting aspects of this work were its multi-disciplinarity and its strong relation to chemical/biological fields. I would like therefore to gratefully acknowledge Dr. S. Verpoorte and Dr. K. Fluri who introduced me to the weird world of ”electroosmotic pumping”, ”heterogeneous immunoassay” and ”laser induced fluorescence detection”. My special thank also go to S. Verpoorte for her help, advices and for the time given to read proceedings, papers as well as the manuscript of the present thesis.

All my gratitude to the members of the jury, Prof. H. P. Herzig, Dr. R. Kunz and Dr. S. Verpoorte and especially (with my apologies) Dr. R. Kunz for putting up with a very short delay to read the manuscript. I regret that a busy timetable did not allow Prof. D. J. Harrison to be part of this jury but I would like to thank him for having accepted.

During these years passed at the IMT, I had the chance to work with many wonderful people and I would like to thank them all. So thank you everybody! A special thank though to K. Weible for his help and his always judicious advices. Ken, sorry for preventing you from working a couple of week-ends! Thank you to R. Völkel who shared his office with me when I came to IMT, for his help at the beginning of this project and, after his departure of IMT, for giving me access to Karl Süss Neuchâtel facilites. A very special thank to P. Blattner for sharing his office with me during, in my point of view, a too short period of time. I am very much indebted to you Peter for a lot of things that it would be too long to list. Thank you also to C. Bohley who is sharing the office with me now and who shared it during the worst times...

I wish to express my gratitude to L. Ceriotti, O. Guenat and J. Lichtenberg for their invaluable help. Thank you also to all the other members of Prof. de Rooij's team with a special thank to the wonderfull technological team, namely S. Jeanneret, S. Jenny,

S. Pochon, P.-A. Clerc and G. Mondin for freely letting me work in the clean-room facilities and for their help in the realization of my chips.

Thank you to Dr. P. Rossi of the Institute of microbiology of the University of Neuchtel for the helpfull discusions and to provinding me with a providential pump necessary to my measurements. Thank you also to ”philosopher farmer” P. Proellochs for have read part of this manuscript.

I also wish to express my gratitude to my parents and familly who supported me during my (long) studies. A very special thank to my former maternal grandfather who bears an strong reponsability for the path I choose. Thank you for a certain steam engine... Finally, the words fail to express my gratitude for the support and encouragement I have received at home. So thank you Murielle for your presence and your love.

This work would not have been possible without the support of the Swiss governement and the priority program Micro- and Nanosystems Technology.

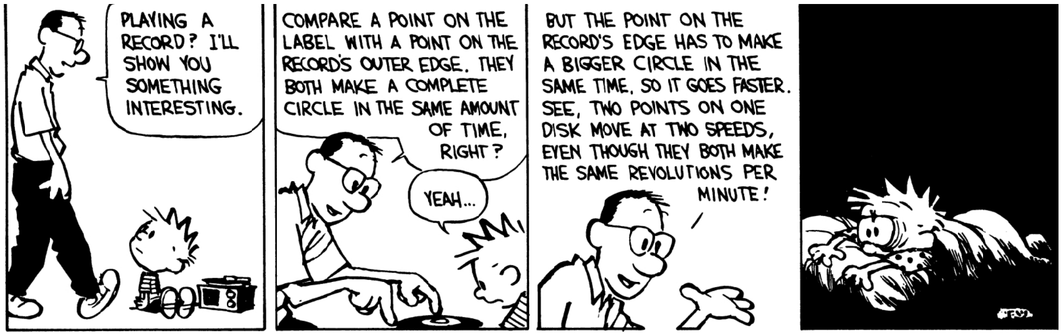

Bill Watterson, *The Indispensable Calvin and Hobbes*, Andrews McMeel Publishing, 1992.

Appendix A

Bibliography

Bibliography

[1] H. M. Widmer, "Trends in industrial analytical chemistry," *Trends in analytical chemistry* **2**(1), pp. 77–79, 1983.

[2] N. Graber, H. Lüdi, and H. M. Widmer, "The use of chemical sensors in industry," *Sensors and Actuators B* **1**, pp. 239–243, 1990.

[3] A. Manz, N. Graber, and H. M. Widmer, "Miniaturized total chemical analysis systems: a novel concept for chemical sensing," *Sensors and Actuators B* **1**, pp. 244–248, 1990.

[4] A. Manz, C. S. Effenhauser, N. Burggraf, D. J. Harrison, K. Seiler, and K. Fluri, "Electroosmotic pumping and electrophoretic separations for miniaturized chemical analysis systems," *J. Micromech. Microeng.* **4**, pp. 257–265, 1994.

[5] C. S. Effenhauser, G. J. M. Bruin, and A. Paulus, "Integretad chip-based capillary electrophoresis," *Electrophoresis* **18**, pp. 2203–2213, 1997.

[6] E. Verpoorte, B. H. van der Schoot, S. Jeanneret, A. Manz, H. M. Widmer, and N. F. de Rooij, "Three-dimensional micro-flow manifolds for miniaturized chemical analysis systems," *J. Micromech. Microeng.* **4**, pp. 246–256, 1994.

[7] D. J. Harrison, P. G. Glavina, and A. Manz, "Towards miniaturized electrophoresis and chemical analysis systems on silicon: an alternative to chemical sensors," *Sensors and Actuators B* **10**, pp. 107–116, 1993.

[8] S. M. Sze, *Semiconductor devices, physics and technology*, John Wiley & Sons, New York, 1985.

[9] G. T. A. Kovacs, *Micromachined Transducers Sourcebook*, McGraw-Hill, New York, 1998.

[10] S. C. Terry, J. H. Jerman, and J. B. Angell, "A gas chromatographic air analyzer fabricated on a silicon wafer," *IEEE Transactions on Electronic Devices* **26**(12), pp. 1880–1886, 1979.

[11] S. Shoji and M. Esashi, "Microflow devices and systems," *Journal of Micromechanic and Microengineering* **4**, pp. 157–171, 1994.

[12] H. P. Herzig, ed., *Micro-optics, elements, systems and applications*, Taylor & Francis, London, 1997.

[13] N. F. Borrelli, *Microoptics technology*, Optical Engineering, Marcel Dekker, Inc., New York, 1999.

[14] S. Sinzinger and J. Jahns, *Microoptics*, Wiley-VCH, New York, 1999.

[15] E. Verpoorte, A. Manz, H. Lüdi, A. E. Bruno, F. Maystre, B. Krattiger, H. M. Widmer, B. H. van der Schoot, and N. F. de Rooij, "A silicon flow cell for optical detection in miniaturized total analysis systems," *Sensors and Actuators B* **6**, pp. 66–70, 1992.

[16] Z. Liang, N. Chiem, G. Ocvirk, T. Tang, K. Fluri, and D. J. Harrison, "Microfabrication of a planar absorbance and fluorescence cell for integrated capillary electrophoresis devices," *Analytical Chemistry* **68**, pp. 1040–1046, 1996.

[17] H. Salimi-Moosavi, Y. Jiang, L. Lester, G. McKinnon, and D. J. Harrison, "A multireflection cell for enhanced absorbance detection in microchip-based capillary electrophoresis devices," *Electrophoresis* **21**, pp. 1291–1299, 2000.

[18] B. Krattiger, A. E. Bruno, H. M. Widmer, M. Geiser, and R. Dändliker, "Laser-based refractive-index detection for capillary electrophoresis: ray-tracing interference theory," *Applied Optics* **32**(6), pp. 956–965, 1993.

[19] J. M. Saz, B. Krattiger, A. E. Bruno, F. Maysre, and H. M. Widmer, "Enhanced refractive index detection for capillary electrophoresis using flared capillaries," *Analytical Methods and Instrumentation* **1**(4), pp. 203–207, 1993.

[20] N. Burggraf, B. Krattiger, A. J. de Mello, N. F. de Rooij, and A. Manz, "Holographic refractive index detector for application in microchip-based separation systems," *Analyst* **123**, pp. 1443–1447, 1998.

[21] R. Kunz, J. Edlinger, P. Sixt, and M. T. Gale, "Replicated chirped waveguide gratings for optical sensing applications," *Sensors and Actuators A* **46**, pp. 482–486, 1995.

[22] K. Swinney, D. Markov, and D. J. Bornhop, "Chip-scale universal detection based on backscatter interferometry," *Analytical Chemistry* **72**(13), pp. 2690–2695, 2000.

[23] A. T. Woolley, K. Lao, A. N. Glazer, and R. A. Mathies, "Capillary electrophoresis chips with integrated electrochemical detection," *Analytical Chemistry* **70**, pp. 684–688, 1998.

[24] J. S. Rossier, M. A. Roberts, R. Ferrigno, and H. H. Girault, "Electrochemical detection in polymer microchannels," *Analytical Chemistry* **71**, pp. 4294–4299, 1999.

[25] R. S. Martin, A. J. Gawron, and S. M. Lunte, "Dual-electrode electrochemical detection for poly(dimethylsiloxane)-fabricated capillary electrophoresis microchips," *Analytical Chemistry* **72**, pp. 3196–3202, 2000.

[26] J. R. Alcala, "Real-time chemical sensing employing luminescence techniques," in *Topics in Fluorescence Spectroscopy*, J. R. Lakowicz, ed., vol. 4, pp. 255–292, Plenum Press, New York, 1994.

[27] C. E. Hooper, R. E. Ansorge, and J. G. Rushbrooke, "Low-light imaging technology in the life sciences," *Journal of Bioluminescence and Chemiluminescence* **9**, pp. 113–122, 1994.

[28] G. Ocvirk, T. Tang, and D. J. Harrison, "Optimization of confocal epifluorescence microscopy for microchip-based miniaturized total analysis systems," *Analyst* **123**, pp. 1429–1434, 1998.

[29] J. C. Fister III, S. C. Jacobson, L. M. Davis, and J. M. Ramsey, "Counting single chromophore molecules for ultrasensitive analysis and separations on microchip devices," *Analytical Chemistry* **70**, pp. 431–437, 1998.

[30] B. B. Haab and R. A. Mathies, "Single-molecule detection of DNA separations in microfabricated capillary electrophoresis chips employing focused molecular streams," *Analytical Chemistry* **71**, pp. 5137–5145, 1999.

[31] A. Dodge, K. Fluri, E. Verpoorte, and N. F. de Rooij, "Electrokinetically driven microfluidic chips with surface modified chambers for heterogeneous immunoassays," *accepted in Analytical Chemistry* , March 2001.

[32] A. J. Ozinskas, "Principles of fluorescence immunoassay," in *Topics in Fluorescence Spectroscopy*, J. R. Lakowicz, ed., vol. 4, pp. 449–497, Plenum Press, New York, 1994.

[33] D. L. Taylor and E. D. Salmon, "Basic fluorescence microscopy," *Methods in Cell Biology* **29**, pp. 207–237, 1989.

[34] F. H. Kasten, "Introduction to fluorescent probes: Properties, history and applications," in *Fluorescent and Luminescent Probes for Biological Activity*, W. T. Mason, ed., pp. 12–33, Academic Press, London, 1993.

[35] D. G. Peters, J. M. Hayes, and G. M. Hieftje, *Chemical separations and measurements*, W. B. Saunders Company, Philadelphia, 1974.

[36] D. C. Harris, "Fundamentals of spectrophotometry," in *Quantitative Chemical Analysis*, pp. 511–534, W. H. Freeman and Company, New York, 5th ed., 1999.

[37] D. A. Skoog, F. J. Holler, and T. A. Nieman, "Molecular luminescence spectrometry," in *Principles of Instrumental Analysis*, pp. 355–376, Harcourt Brace College Publishers, Philadelphia, 5th ed., 1998.

[38] D. J. S. Birch and R. E. Imhof, *Topics in Fluorescence Spectroscopy*, vol. 1, Plenum, New York, 1991.

[39] R. J. H. Clarck and R. E. Hester, eds., *Time-Resolved Spectroscopy*, vol. 18 of *Advances in spectroscopy*, John Wiley & Sons, Chichester, 1989.

[40] I. Kheterpal and R. A. Mathies, "Capillary array electrophoresis," *Analytical Chemistry* , pp. 31A –36A, 1999.

[41] G. Jiang, S. Attiya, G. Ocvirk, W. E. Lee, and D. J. Harrison, "Red diode laser induced fluorescence detection with a confocal microscope on a microchip for capillary electrophoresis," *Biosensors & Bioelectronics* **14**, pp. 861–869, 2000.

[42] M. C. Wu, "Micromachining for optical and optoelectronic systems," *Proceedings of the IEEE* **85**, pp. 1833–1855, 1997.

[43] R. A. Conant, J. T. Nee, K. Y. Lau, and R. S. Muller, "A flat high-frequency scanning micromirror," in *Solid-State Sensor and Actuator Workshop*, pp. 101–104, (Hilton Head Island, South Carolina, USA), 2000.

[44] D. Sun, C. Yeh, and M. Rosa, "Scanning microlens shuttles fabricated using silicon-on-insulator wafers," in *Solid-State Sensor and Actuator Workshop*, pp. 259–262, (Hilton Head Island, South Carolina, USA), 2000.

[45] C. Pu, Z. Zhu, and Y.-H. Lo, "Highly sensitive optical coherent detection system using surface micromachining technology," in *MEMS'99*, (Orlando, USA), 1999.

[46] G. Ocvirk, E. Verpoorte, A. Manz, M. Grasserbauer, and H. M. Widmer, "High performance liquid chromatography partially integrated onto a silicon chip," *Analytical Methods and Instrumentation* **2**(2), pp. 74–82, 1995.

[47] A. Okumura, Y. Miyahara, M. Sakairi, and H. Koizumi, "Integrated chemical analysis systems as a step toward ionoelectronics," *Analytical Methods & Instrumentation, Special Issue* $\mu TAS'96$, pp. 22–23, 1996.

[48] A. Bruno, E. Baer, R. Völkel, and C. S. Effenhauser, "Micro-optical fluorescence detection for chip-based multiplexed analysis systems," in *Micro Total Analysis Systems'98*, D. J. Harrison and A. van den Berg, eds., pp. 281–285, Kluwer Academic Publishers, (Banff, Canada), 1998. ISBN 0-7923-5322-6.

[49] R. E. Kunz, G. Duveneck, and M. Ehrat, "Sensing pads for hybrid and monolithic integrated optical immunosensors," in *Medical Sensors II and Fiber Optic Sensors*, A. V. Scheggi, F. Baldini, P. R. Coulet, and O. S. Wolfbeis, eds., vol. 2331, pp. 2–17, proc. SPIE, (Lille, France), 1994.

[50] O. Leistiko and P. F. Jensen, "Integrated bio/chemical microsystems employing optical detection: the clip-on," *Journal of Micromechanic and Microengineering* **8**, pp. 148–150, 1998.

[51] M. T. Gale, M. Rossi, H. Schütz, P. Ehbets, H. P. Herzig, and D. Prongué, "Continuous-relief diffractive optical elements for two-dimensional array generation," *Applied Optics* **32**(14), pp. 2526–2533, 1993.

[52] P. Ehbets, M. Rossi, and H. P. Herzig, "Continuous-relief fan-out elements with optimized fabrication tolerances," *Optical Engineering* **34**(12), pp. 3456–3464, 1995.

[53] M. E. Warren, W. C. Sweatt, J. R. Wendt, C. G. Bailey, C. M. Matzke, D. W. Arnold, S. A. Kemme, A. A. Allerman, T. R. Carter, R. E. Asbill, and S. Samora, "Integrated micro-optical fluorescence detection system for microfluidic electrochromatography," *proc. SPIE* **3878**, pp. 185–187, 1999.

[54] P. Nussbaum, R. Völkel, H. P. Herzig, M. Eisner, and S. Haselbeck, "Design, fabrication and testing of microlens arrays for sensors and microsystems," *Pure and Applied Optics* **6**, pp. 1–20, 1997.

[55] L.-W. Pan, L. Lin, and J. Ni, "Cylindrical plastic lens array fabricated by a micro intrusion process," in *MEMS'99*, pp. 217–221, (Orlando, USA), 1999.

[56] J. B. Pawley, ed., *Handbook of Biological Confocal Microscopy*, Plenum Press, New York, 2 ed., 1995.

[57] B. E. A. Saleh and C. T. Malvin, *Fundamentals of photonics*, John Wiley & Sons, Inc., New York, 1991.

[58] G. A. C. Spierings and J. van Dijk, "The dissolution of $Na_2O - MgO - SiO_2$ glass in aqueous HF solutions," *Journal of Material Science* **22**, pp. 1869–1874, 1987.

[59] M. Nese and A. Hanneborg, "Anodic bonding of silicon to silicon wafers coated with aluminium, silicon oxide, polysilicon or silicon nitride," *Sensors and Actuators A* **37**, pp. 61–67, 1993.

[60] A. Berthold, L. Nicola, P. Sarro, and M. Vellekoop, "Glass-to-glass anodic bonding with standard ic technology thin films as intermediate layers," *Sensors and Actuators A* **82**, pp. 224–228, 2000.

[61] Z. Fan and D. J. Harrison, "Rapid injection and separation of amino acids with capillary electrophoresis systems micromachined on a glass chip," *Analytical Chemistry* **66**, pp. 177–184, 1994.

[62] M. Stjernström and J. Roeraade, "Method for fabrication of microfluidic systems in glass," *J. Micromech. Microeng.* **8**, pp. 33–38, 1998.

[63] J.-C. Roulet, K. Fluri, E. Verpoorte, R. Völkel, H. P. Herzig, N. F. de Rooij, and R. Dändliker, "Micro-optic integration for fluorescence detection in μTAS systems," in *Transducers'99*, vol. 1, pp. 120–123, (Sendai, Japan), 1999.

[64] M. Born and E. Wolf, *Principles of Optics*, Cambridge University Press, Cambridge, 1999. sixth edition.

[65] J. Schwider and O. Falkenstörfer, "Twymann-Green interferometer for testing microspheres," *Optical Engineering* **34**(10), pp. 2972–2975, 1995.

[66] D. Malacara and Z. Malacara, *Handbook of lens design*, Optical Engineering, Marcel Dekker Inc., New York, 1994.

[67] N. M. Virendra, *Optical Imaging and Aberrations*, vol. 1 of *Ray Geometrical Optics*, SPIE, Bellingham, 1998.

[68] B. He, L. Tan, and F. Regnier, "Microfabricated filters for microfluidic analytical systems," *Analytical Chemistry* **71**, pp. 1464–1468, 1999.

[69] H. Andersson, W. van der Wijngaart, P. Enoksson, and G. Stemme, “Micromachined flow-through filter-chamber for chemical reactions on beads,” *Sensors and Actuators B* **67**, pp. 203–208, 2000.

[70] R. A. Mathies and K. Peck, “Optimization of high-sensitivity fluorescence detection,” *Analytical Chemistry* **62**(17), pp. 1–6, 1990.

[71] S. Traut, M. Rossi, and H. P. Herzig, “Replicated arrays of hybrid elements for application in a low-cost micro-spectrometer array,” *Journal of Modern Optics* **47**(13), pp. 2391–2397, 2000.

[72] N. Thomas *et al.*, “Integrated cell based assays in microfabricated disposable CD devices,” in *Micro Total Analysis Systems 2000*, A. van den Berg, W. Olthuis, and P. Bergveld, eds., pp. 249–252, Kluwer Academic Publishers, (Enschede, The Netherlands), 2000. ISBN 0-7923-6387-6.

[73] H. Becker, W. Dietz, and P. Dannberg, “Microfluidic manifolds by polymer hot embossing for μ-TAS applications,” in *Micro Total Analysis Systems'98*, D. J. Harrison and A. van den Berg, eds., pp. 253–256, Kluwer Academic Publishers, (Banff, Canada), 1998. ISBN 0-7923-5322-6.

Appendix B

List of publications

Refereed Articles.

- D.1 J.-C. Roulet, E. Verpoorte, R. Völkel, H. P. Herzig, N. F. de Rooij, and R. Dändliker, Microchemical chip with integrated fluorescence detection system for *μTAS* applications, *Analytical Chemistry*, submitted for publication, June 2001.
- D.2 J.-C. Roulet, E. Verpoorte, R. Völkel, H. P. Herzig, N. F. de Rooij, and R. Dändliker, Fabrication of Multilayer Systems Combining Microfluidic and Micro-Optical Elements for Fluorescence Detection, *IEEE Journal of Microelectromechanical Systems*, accepted for publication, March 2001 (will appear in Vol. 10 either September or December 2001).
- D.3 J.-C. Roulet, E. Verpoorte, R. Völkel, H. P. Herzig, N. F. de Rooij, and R. Dändliker, Microlens Systems for Fluorescence Detection in Chemical Microsystems, *Optical Engineering*, **40**(5), pp. 814–821, (May 2001).

Proceedings.

Main author:

1. J.-C. Roulet, E. Verpoorte, R. Völkel, H. P. Herzig, N. F. de Rooij, and R. Dändliker, Integration of micro-optical systems for fluorescence detection in *μTAS* applications, *Proc. of the μTAS'2000 Symposium*, 14-18 May, Enschede, The Netherlands, pp. 163–166, (2000).
2. J.-C. Roulet, K. Fluri, E. Verpoorte, R. Völkel, H. P. Herzig, N. F. de Rooij, and R. Dändliker, Micro-optic integration for fluorescence detection in *μTAS* systems, *Proc. Transducers'99*, 7-10 June, Sendai, Japan, pp. 120–123, (1999).
3. J.-C. Roulet, K. Fluri, E. Verpoorte, R. Völkel, H. P. Herzig, N. F. de Rooij, and R. Dändliker, Micro-optical systems for fluorescence detection in *μTAS* applications, *Proc. of the μTAS'98 workshop*, 13–16 October, Banff, Canada, pp. 287–290, (1998).

Co-author:

4. E. Verpoorte, L. Ceriotti, A. Daridon, A. Dodge, K. Fluri, G.-L. Lettieri, J. Lichtenberg, V. Linder, J.-C. Roulet, R. Völkel, H. P. Herzig, R. Dändliker, and N. F. de Rooij, Microfabricated tools for fast chemical analysis, *2^{nd} Cherry Blossom Symposium (Japanese Laboratory Automation 2000)*, 5–7 April, Karatsu City, Saga Prefecture, Japan, (2000).

5. O. T. Guenat, T. Hirata, T. Akashi, M.-A. Grétillat, M. Boillat, B. van der Schoot, K. Fluri, E. Verpoorte, J.-C. Roulet, R. Völkel, H. P. Herzig, R. Dändliker, and N. F. de Rooij, Microfactory on a chip, *International Workshop on Microfactories*, 7–9 December, Tsukuba AIST Research Center, Tsukuba, Japan, (1988).
6. E. Verpoorte, G. Boer, A. Dodge, G.-L. Lettieri, K. Fluri, J.-C. Roulet, R. Völkel, H. P. Herzig, R. Dändliker, and N. F. de Rooij, Toward the Lab-on-Chip: Multi-Functional Miniaturized Analysis Systems for Bioanalytics, *Proc. of Nanotech'98*, 24–25 November, Montreux, Switzerland, (1998).
7. J.-C. Roulet, E. Verpoorte, K. Fluri, R. Völkel, G. L. Duveneck, H. P. Herzig, B. van der Schoot, R. Dändliker, and N. F. de Rooij, A Generally Applicable Microsystem for Rapid Heterogeneous Immunoassay Combining Microfluidic and Micro-optical Elements, *Proc. of Nanotech'97*, 18–21 November, Montreux, Switzerland, (1997).
8. P. Nussbaum, R. Völkel, J.-C. Roulet, E. Verpoorte K. J. Weible, A. E. Bruno, H. P. Herzig, Design, fabrication and testing of microlenses arrays for sensors and microsystems, *EOS Topical meeting Digest Series: 13*, May 1997, pp.110–114, London, England, (1997).
9. R. Völkel, P. Nussbaum, J.-C. Roulet, E. Verpoorte, K. Fluri, H. P. Herzig, Design, fabrication and testing of microlenses arrays for sensors and microsystems, *European Symposium on Lasers and Optics in Manufacturing [EOS/ SPIE 3099]*, 16–20 June, Munich, Germany, (1997).